

**SEISMIC ANISOTROPY  
BENEATH THE SOUTHERN PUNA PLATEAU**

---

A Thesis Presented to the Faculty of the Graduate School at the  
University of Missouri

---

In Partial Fulfillment of the Requirements for the Degree  
Master of Science

---

by  
DANIELLE D. ROBINSON

Dr. Eric Sandvol, Thesis Supervisor

DECEMBER 2009

The undersigned, appointed by the dean of the Graduate School, have examined the thesis entitled

**SEISMIC ANISOTROPY  
BENEATH THE SOUTHERN PUNA PLATEAU**

presented by Danielle D. Robinson,

a candidate for the degree of Master of Science,

and hereby certify that, in their opinion, it is worthy of acceptance.

---

Dr. Eric Sandvol

---

Dr. Francisco Gomez

---

Dr. Brent Rosenblad

To  
Mom and Dad,  
*forever my foundation.*

## ACKNOWLEDGEMENTS

I would like to first thank the National Science Foundation for funding this research. This work was supported under Grant Proposal EAR-05 382 45, which covered travel expenses, field work, and most importantly the research. Also, thank you to IRIS/PASSCAL for the use and technical support of its instruments.

Thanks to the University of Missouri and the Geological Sciences Department for the use of its facilities, educational background for this research, and financial support through research and teaching assistantships during my graduate studies.

I want to thank my thesis advisor, Dr. Eric Sandvol, for his patience, help, and support both in the field and the classroom. I also want to thank my committee members, Dr. Francisco Gomez and Dr. Brent Rosenblad, for their help and suggestions.

Last, thank you to Sue Kay, Betty and Peluso Coira, and everyone else who helped in the field by installing/servicing seismometers, driving through the plateau, digging holes, and also protecting the sites.

## TABLE OF CONTENTS

ACKNOWLEDGEMENTS .....	ii
LIST OF FIGURES .....	vi
LIST OF EQUATIONS .....	ix
LIST OF PHOTOS .....	x
ABSTRACT .....	xi
CHAPTER 1: ACTIVE TECTONICS OF THE ANDEAN MARGIN .....	1
Introduction .....	1
Regional Tectonics .....	3
<b>Subduction style</b> .....	5
<b>Effects of subduction angle</b> .....	6
Evolution of the Central Andean Plateau .....	8
<b>Plateau uplift</b> .....	9
<b>Tectonic histories of the central Andean plateau</b> .....	10
<b>Southern Puna plateau</b> .....	11
<b>Lithospheric thinning</b> .....	15
Delamination .....	16
<b>Original models</b> .....	17
<b>Modified model</b> .....	17
<b>Indicators</b> .....	18
<b>Delamination beneath the Puna</b> .....	19
Anisotropy and Mantle Deformation .....	20
CHAPTER 2: METHOD OF SHEAR-WAVE SPLITTING .....	24

Shear-Wave Splitting .....	24
Measuring Splitting Parameters .....	28
<b>Rotation-correlation</b> .....	29
<b>Grid search</b> .....	30
<b>Complications</b> .....	31
Puna Seismic Array .....	32
<b>Installation</b> .....	34
<b>Neighboring experiments</b> .....	36
Data Processing .....	38
<b>Raw data</b> .....	38
<b>Windowing</b> .....	39
<b>Quality-control</b> .....	40
<b>Stacking</b> .....	48
CHAPTER 3: RESULTS AND IMPLICATIONS FOR MANTLE DEFORMATION	
.....	53
Results .....	53
Splitting Parameters .....	57
<b>Constraining depth</b> .....	59
<b>Localized splitting</b> .....	68
Stacking Results .....	71
<b>Teleseismic events stacking</b> .....	77
<b>Local events stacking</b> .....	78
Asthenospheric Motion .....	81

<b>Global flow patterns</b> .....	83
<b>Flow patterns of South America</b> .....	83
<b>South America and delamination</b> .....	86
Tectonic Implications .....	87
<b>Trench-parallel motion</b> .....	88
<b>Trench-perpendicular motion</b> .....	89
<b>Complex flow patterns</b> .....	90
CHAPTER 4: SUMMARY AND CONCLUSIONS .....	96
APPENDIX	
A. Matlab stacking code .....	100
B. Splitting events .....	102
C. Splitting results .....	104
D. Quality-control inspection of shear-wave splitting .....	107
E. Splitting versus BAZ .....	120
F. Stacking data .....	122
G. Stacking results .....	130
H. Topographic plots of stacking results.....	135
REFERENCES .....	139

## LIST OF FIGURES

Figure	Page
1.1. Nazca-South American subduction margin .....	4
1.2. Effects of shortening along the South American margin .....	7
1.3. Central Andean Plateau .....	10
1.4. Shortening variation along the Andean margin .....	13
1.5. Delamination model .....	16
1.6. Mantle anisotropy .....	21
2.1. Seismic wave components .....	24
2.2. Shear-wave phases .....	25
2.3. Shear-wave splitting .....	26
2.4. Surface projected fast and slow polarization directions .....	28
2.5. Multiple layers of anisotropy .....	31
2.6. PUNA seismic array station map .....	33
2.7. Neighboring seismic experiments .....	37
2.8. Window picking .....	41
2.9. Visible splitting between the fast and slow components .....	42
2.10. Waveform energy on seismogram components .....	43
2.11. Particle motion plots .....	44
2.12. Eigenvalue singularity .....	45

2.13. Energy contour plot .....	46
2.14. Null event depicted by energy contour plot .....	47
2.15. Earthquake coverage for the PUNA array .....	49
2.16. Stacking surfaces .....	49
2.17. Energy stacking example .....	52
3.1. Seismogram of local event crustal splitting .....	55
3.2. Seismogram of teleseismic splitting .....	56
3.3. Topographic map of teleseismic events splitting results.....	57
3.4. Topographic map of local events splitting results.....	58
3.5. Shear-wave splitting depth constraint .....	59
3.6. Regional station map .....	60
3.7. Local events map .....	61
3.8. Splitting versus depth .....	65
3.9. Regional depth constraint of anisotropy .....	68
3.10. Splitting versus BAZ modulo 90° for local events .....	70
3.11. Magnified map of southeast stations .....	71
3.12. Splitting versus BAZ modulo 90° southeast stations .....	73
3.13. Teleseismic energy contour plots for station BB13 .....	76
3.14. Stacked teleseismic events splitting compared to original .....	78
3.15. Local events stacked splitting compared with original .....	81
3.16. Trench-parallel flow beneath South America .....	84

3.17. Results of the BANJO experiment .....	86
3.18. Model of general flow patterns .....	88
3.19. Comparison of stacked local shallow splitting to strain patterns .....	90
3.20. Comparison of stacked teleseismic splitting to slab contours .....	92
3.21. General tectonic model of subslab mantle flow .....	93
3.22. General tectonic model describing mantle wedge flow .....	94

## LIST OF EQUATIONS

Equation	Page
2.1. Delay time .....	26
2.2. Percent anisotropy .....	26
2.3. Fast polarization .....	27
2.4. Slow polarization .....	27
2.5. Radial component .....	28
2.6. Transverse component .....	28
2.7. Covariance matrix .....	29
2.8. Energy of the transverse component .....	30
2.9. Eigenvalue for absence of anisotropy .....	44
2.10. F-test .....	46
2.11. Critical surface conversion angle .....	47
2.12. Estimated model parameters .....	50
2.13. Weight matrix .....	50
2.14. Variance .....	50
2.15. Stacking energy .....	51

## LIST OF PHOTOS

Photo	Page
2.1. Installation of NS08 .....	34
2.2. Surprise river crossing .....	35
2.3. Example station locations across the Puna .....	36

# **SEISMIC ANISOTROPY BENEATH THE SOUTHERN PUNA PLATEAU**

Danielle D. Robinson

Dr. Eric Sandvol, Thesis Supervisor

## **ABSTRACT**

The southern Puna plateau (25°S to 28°S) contains a number of anomalous features that are not present in the Puna-Altiplano plateau region to the north, including: 1) a distinctive spatial and geochemical pattern of mafic lavas and giant ignimbrites, 2) a high topography with a large deficit in crustal shortening, 3) an underlying slab with a gap in teleseismic intermediate depth seismicity, and 4) a transitional dip between a steeper segment to the north and a flat-slab to the south. These characteristics have led to suggestions that a link exists between plateau uplift in this region and removal of the underlying lower crust and lithospheric mantle. This study is designed to test this hypothesis using seismic anisotropy to evaluate mantle flow beneath the southern Puna plateau that may be associated with these anomalous features. This study provides foundational research in a region where no previous seismic networks have existed.

As an initial interpretation of lithospheric structure, shear-wave splitting measurements caused by anisotropic layers of the mantle were analyzed in an effort to infer asthenospheric flow patterns. Interpretations were completed by: 1) determining fast polarization directions and delay time magnitudes of splitting events, 2) providing a vertical constraint on the location of mantle anisotropy

using a combination of teleseismic events and deep and intermediate events of known depths, and 3) searching for any localized splitting dependencies using back azimuths of events.

A total of 30 teleseismic and 88 local events demonstrated shear-wave splitting for 43 PUNA stations over a 16-month period. Results illustrate a very complex pattern throughout the southern Puna plateau. In general, trench-parallel subslab splitting occurs from retrograde slab motion and shifts to trench-perpendicular motion as the angle of slab subduction shallows. Slab flattening also seems to affect the mantle wedge as splitting above the slab shifts from trench-perpendicular in accordance with absolute and relative plate motion to trench-parallel more towards the trench. A toroidal rotation pattern of mantle wedge splitting is also observed around the Cerro Galan ignimbrite region, suggesting a flow obstruction.

As a primary source of ignimbrite flare-ups, delamination is a possible cause of the toroidal splitting pattern detected in the southern Puna plateau. The implication of a delamination event within the Puna could aid in understanding lithospheric evolution of similar orogenic systems including Tibet and the western US.

# **CHAPTER 1: Active Tectonics of the Andean Margin**

## **INTRODUCTION**

The central Andean plateau stands as the second highest plateau in the world, second only to the Tibetan plateau of the Himalayas. Unlike the formation of the Tibetan plateau during continental collision, the Andes mountain range and central Andean plateau developed as a product of subduction. Extending 2,000 kilometers in length and 300 kilometers in width, average elevations of the plateau are greater than 3.7 kilometers, and the high topography is supported by a thick crust of at least 70 kilometers (Kay et al., 1994; Whitman et al., 1996). A simplified history of geologic events occurring in the central Andes includes initial subduction magmatism, plateau uplift from contractional deformation and thermal plateau uplift, crustal extension of the back-arc, subduction erosion of the forearc, and finally a basal crust and mantle lithosphere removal by delamination. Crustal shortening of the plateau combined with the process, timing, and result of lithospheric delamination remains in question though (Kay et al., 1994, 1999; Allmendinger et al., 1997; Babeyko et al., 2005; Hindle et al., 2005).

Geodynamic features of the central Andean plateau such as rapid uplift, stress change, and magmatism indicate the occurrence of delamination.

However, details that describe the process in a general model are still developing and continually evolving (Kay and Kay, 1993; Kay et al., 1994; Lamb and Hoke, 1997; Beck and Zandt, 2002; Yuan et al., 2002; Sobolev and Babeyko, 2005). The first delamination models involved the western US and Tibet. In these areas, rapid uplift and extension were followed by regional stress changes, a possible thinning lithosphere, and an increase in magmatism (Bird, 1979; England and Houseman, 1989). The loss of lithosphere, or lithospheric delamination, explains these geodynamic features. Similar features were observed in the central Andes, leading to a hypothesis of delamination within this area as well. However, Kay and Kay (1993) modified the original delamination models to include the loss of eclogitic crust as well as lithospheric mantle and encompassed a larger density contrast than other models to assist in creation of negative buoyancy in the uppermost mantle. To validate and further develop this model, the area thought to be undergoing delamination should be researched to find the behavior of associated mantle flow, discovering how much and where lithospheric separation has occurred.

This research involves the use of shear-wave splitting techniques and methodology to infer mantle flow patterns beneath the southern Puna plateau. Shear-wave splitting can illustrate and confine the location and extent of seismic anisotropy in the crust and mantle and allows for the determination of mantle deformation or flow patterns. Mantle deformation should directly reflect the behavior of a hypothetical delaminated block of lithosphere.

Specific objectives of this study that ultimately lead to inferences of mantle flow patterns include:

- (1) finding the fast polarization direction and magnitude of both teleseismic and local splitting events,
- (2) providing a vertical constraint on the location of mantle polarization anisotropy with the combination of teleseismic events and deep and intermediate events that originate from known depths, and
- (3) searching for any splitting dependencies based on shear-wave splitting versus back-azimuthal patterns.

By accomplishing these objectives, this research will aid in providing a link between upper mantle flow patterns of the southern Puna plateau and deformation of the overriding lithosphere.

## **REGIONAL TECTONICS**

The Andes Mountain Range has formed in large part due to the subduction of the Nazca Plate beneath the South American plate. The South American continent moves westward relative to the eastward moving Nazca Plate that subducts at ~80 millimeters per year (Espurt et al., 2007). This type of subduction is termed an “Andean”-style margin or active continental margin (Figure 1.1). A trench and active magmatic arc are found along the west side of

the cordillera, and a fold and thrust system is located to the east (Whitman et al., 1996). The western slope position of the cordillera changes according to the location of the tip of the asthenospheric wedge, which lies directly underneath the South American plate and above the Nazca plate. Cahill and Isacks (1992)

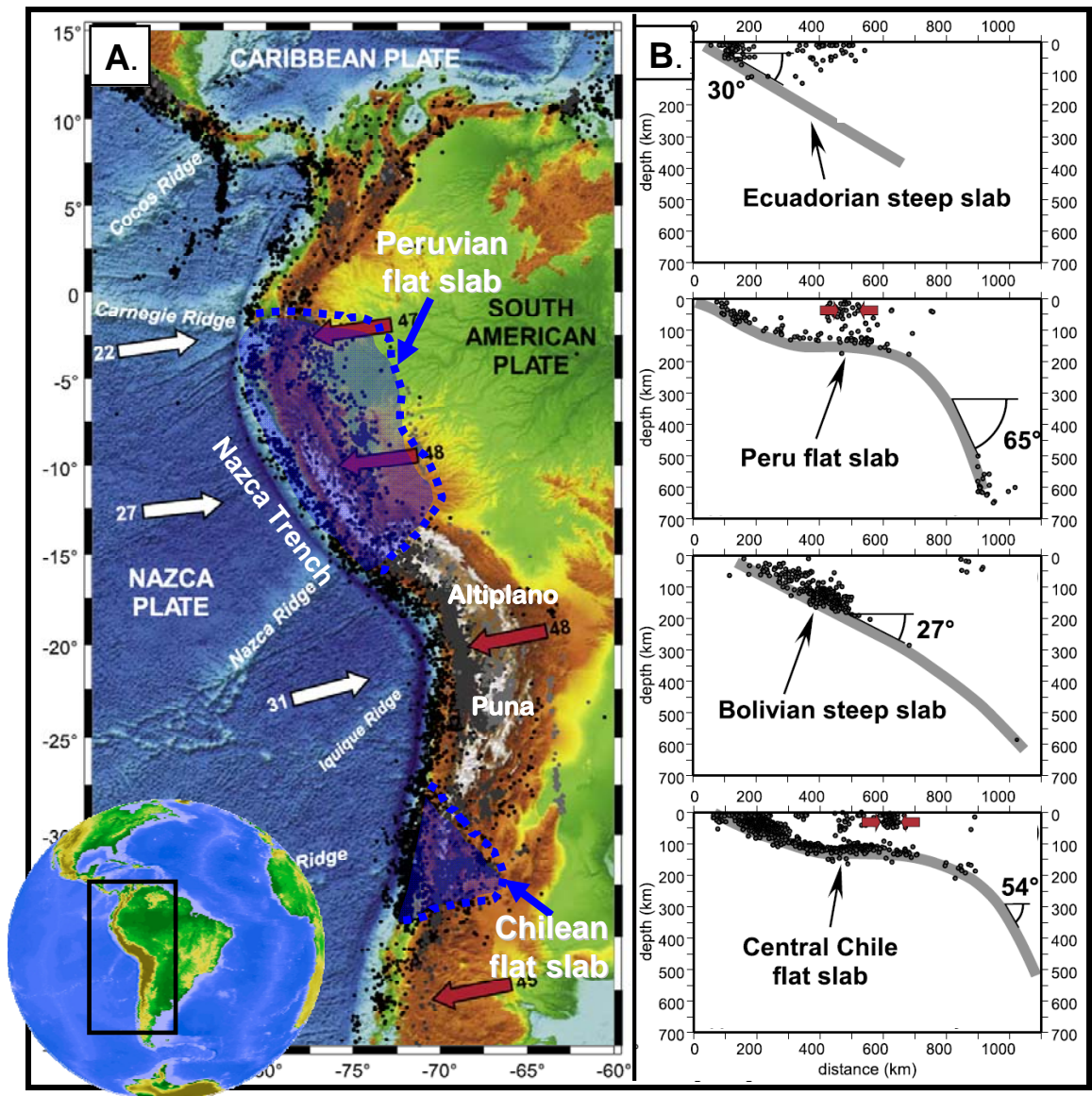


**Figure 1.1.** Nazca-South American subduction margin. A. Bathymetry and topography reveal the location of the subduction zone trench, oceanic ridges, and plateau area. The Peruvian and Chilean flat slabs are both noted with blue dashed lines. The Altiplano and Puna plateaus comprise the central Andean plateau. White and red arrows indicate relative plate motion velocities in  $\text{mm a}^{-1}$ . B. The profiles of each subduction segment along South America illustrate differences in subduction angle (Modified from Espurt et al., 2008).

presume that the location of the mantle wedge is a guide to where magma generation, thermal thinning, and mechanical weakening of the overriding plate will occur.

### **Subduction style**

Along different segments of the Andean margin, the subducting slab angle changes and can be categorized into two different types of subduction: shallow ( $<30^\circ$ ) and normal ( $>30^\circ$ ). Four distinct segments are noted between  $4^\circ\text{S}$  and  $45^\circ\text{S}$  (Figure 1.1). Beneath two of the segments, normal subduction occurs. These segments include southern Peru to northern Chile ( $15^\circ\text{S}$  to  $28^\circ\text{S}$ ) and southern Chile (south of  $33^\circ\text{S}$ ). Shallow subduction occurs beneath the other two segments which include northern to central Peru ( $4^\circ\text{S}$  to  $15^\circ\text{S}$ ) and western Argentina ( $28^\circ\text{S}$  to  $33^\circ\text{S}$ ) (Cahill and Isacks, 1992).

Shallow subduction is not considered a normal occurrence and can begin with the subduction of aseismic ridges, oceanic plateaus, and even seamounts. These features are considered topographic anomalies, or 'asperities,' where the oceanic crust is thicker than the surrounding plate. Usually, these oceanic anomalies will accrete or scrape off during a subduction collision. However, oftentimes they will continue to subduct at a very shallow angle because of an increase in buoyancy of the subducting slab due to thicker crust (Espurt et al., 2008).

The rate at which plates converge can also affect subduction angle. Faster convergence rates produce a thicker continental crust, which is observed along

shallow areas of subduction. Likewise, areas of steeper subduction form from slower convergence rates and have thinner associated continental crust (Allmendinger et al., 1997). Some areas of the Andes illustrating steeper subduction, such as the Puna plateau, have considerably thick crust though and stand quite high topographically.

### **Effects of subduction angle**

As the subducting slab angle changes along different segments of the Andean margin, tectonic behavior and magmatism change along-strike as well (Whitman et al., 1996). This includes the amount of crustal shortening that occurs above a subducting slab and the location and type of volcanic rocks present.

#### Crustal shortening:

Horizontal compression causes crustal shortening, so the amount of shortening and topographic elevation will therefore vary along-strike according to the angle of subduction versus the magnitude of maximum horizontal stress (Figure 1.2). The subduction angle at the center of the concave curvature of western South America, known as the 'Bolivian orocline,' steepened ~12 Ma when compressional failure occurred (Isacks, 1988). Continental material underwent more horizontal shortening than regions north and south, which had shallower subduction angles, and the margin bent into its present shape (Cahill and Isacks, 1992).

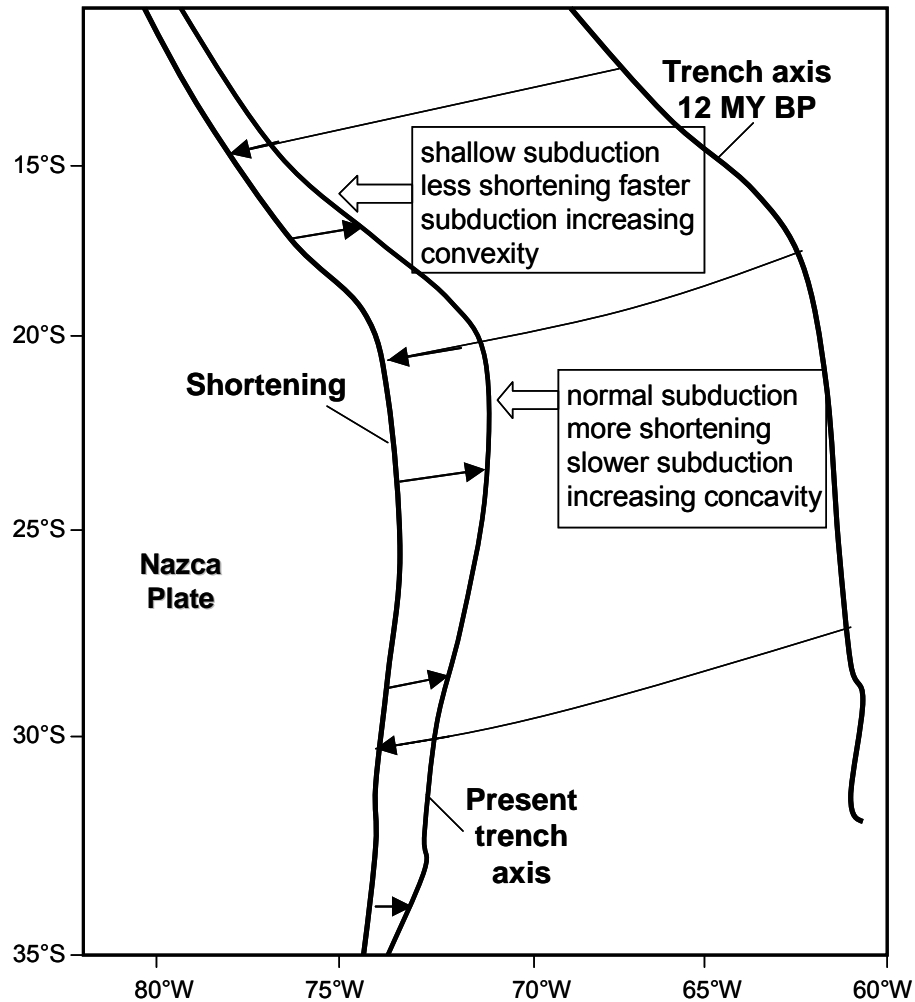


**Figure 1.2.** Effects of shortening along the South American margin. Because of a steeper subduction angle and associated weaker lithosphere, more shortening has occurred at the 20°S concavity and has caused a slower subduction rate. The trench axis is shown both 12 million years before ago and at the present. Because of varying along-strike shortening rates, the margin has bent into its present shape. (Modified after Cahill and Isacks, 1992).

Volcanic rocks:

Volcanism along the Andes can also be attributed to different subduction angles. A steeper subduction angle typically causes the occurrence of an active volcanic arc while areas of shallow subduction are void of volcanic arcs. The location of the magmatic “front” of a volcanic arc is led by the tip of the asthenospheric wedge and changes shape and location according to subduction

angle (Isacks, 1988; Cahill and Isacks, 1992). As subduction angle shallows, the asthenospheric wedge is forced further inland away from the trench. Where shallow subduction occurs along the South American margin, the asthenospheric wedge is found nearly 800 kilometers inland from the trench (Isacks, 1988). Steepening of the subduction angle within the central Andes can be spatially correlated to Cenozoic arc volcanism and the formation of the central Andean plateau (Cahill and Isacks, 1992).

## **EVOLUTION OF THE CENTRAL ANDEAN PLATEAU**

Between 15°S and 28°S, the main feature of the central Andes is a broad plateau (Figure 1.1). Crustal thicknesses for this region are calculated to be greater than 55 kilometers and up to 70 kilometers in some areas (Isacks, 1988). A vast majority of the plateau has low to moderate relief because erosion cannot occur quickly enough to transport material out of the internally draining system. The plateau originates from undeformed volcanic rocks of the Miocene to Recent that cover the deformed basement units of the pre-Miocene (Kay et al., 1994). Uplift of the central Andean plateau involved two major aspects: horizontal crustal shortening and a thermal component involving a magmatic influx (Riller et al., 2001).

## **Plateau uplift**

### Crustal shortening:

Horizontal shortening of the central Andes is proposed by Isacks (1988) to have failed during two deformational stages. The first phase, known as the Quechua phase, refers to the widespread horizontal shortening and crustal thickening that began 25 Ma in the north or between 15 and 20 Ma in the south (Allmendinger et al., 1997). This stage resulted in thick-skinned deformation with basement rocks thrust on top of sedimentary rocks, resulting in internally drained, intermontane basins. The shortening that occurred during this phase was the most important cause of crustal thickening.

During the second deformational stage, folding and thrusting shifted eastward beginning 12 to 6 Ma in the north, and collapse calderas formed. The upper crust was thrust over the eastern foreland, while lower crust to the west of this continued to thicken. To the south, shortening continued until 1 or 2 Ma. The result was an uplift that produced the central Andean plateau. This event is temporally marked by calderas as an important time geodynamically in the evolution of the plateau. Once the limit of crustal shortening or vertical thickening was reached though, another factor must have caused continued lithospheric uplift in the central Andes (Isacks, 1988).

### Thermal component:

Additionally, the high topography of the central Andes is supported by thermal isostasy that occurred as a consequence of lithospheric thinning (Isacks, 1988). The extensive volcanics covering the plateau confirm this postulation. A

thickening asthenospheric wedge caused a regional magmatic influx and general increase in temperature. Partially molten crustal material was thinned or replaced with mantle material, and the crust became isostatically supported, creating uplift. According to Whitman et al. (1996), if the lithosphere happens to thin from 140 to 70 kilometers, approximately one kilometer of plateau elevation can be explained (Whitman et al., 1996). In addition to a magmatic influx, lithospheric thinning can also be achieved by delamination, which will later be discussed in detail.

### **Tectonic histories of the central Andean plateau**

The Altiplano plateau of the north and the Puna plateau of the south split the central Andean plateau into two parts displayed in Figure 1.3. The difference in elevation distribution of the two plateaus demonstrates the contrasting tectonic histories of the late Cenozoic.

The Bolivian Altiplano is underlain by a stronger lithosphere due to the underthrust of the Brazilian shield. Only the Paleozoic sedimentary wedge has deformed. The termination of this thin-skinned deformation occurs near

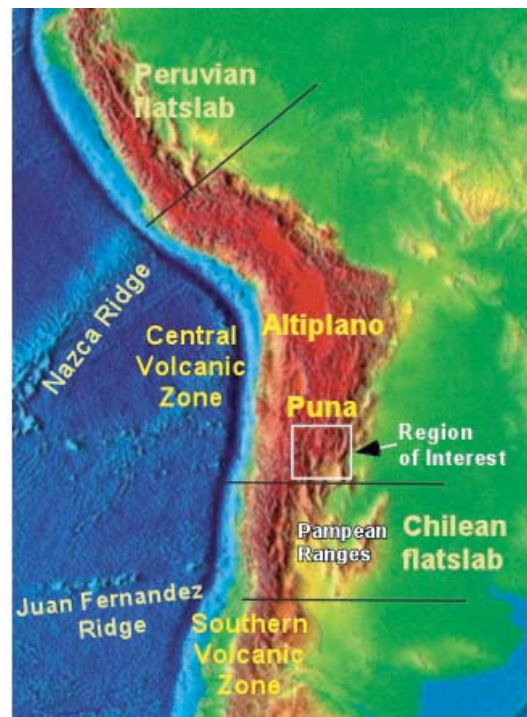


**Figure 1.3.** Central Andean Plateau. The plateau is divided into the Altiplano plateau of the north and the Puna of the south. The Puna plateau is located at a subduction transition zone between normal subduction to the north and shallow subduction to the south.

23°S-24°S and correlates with the superposition of Late Cretaceous rift basins to the south (Allmendinger et al., 1997). Within the crust of the Puna plateau, Late Miocene basement-involved deformation has occurred due to a thinner and weaker lithosphere. Thickening underneath the Altiplano plateau occurred from underthrusting of the Brazilian shield, while thinning farther south points to a delamination event (Whitman et al., 1992; 1996).

### **Southern Puna plateau**

In addition to topography differences, the southern Puna plateau is also characterized by mafic lavas and giant ignimbrites, a crustal shortening deficit, location at a subduction transition zone, and a proposed seismic gap. These attributes all suggest lithospheric thinning.

#### Mafic lavas and ignimbrites:

Cahill and Isacks (1992) suggest that late Cenozoic basaltic magmatism of the southern Puna plateau has a mantle source with very little crustal contamination. A change in young back-arc mafic flows from shoshonitic in the Altiplano and northern Puna to OIB (oceanic island basalt) type in the southern Puna indicates an increase in percentage of mantle melt and decrease in the lithospheric component (Kay and Kay, 1993). The current basaltic additions to the crust originate from the mantle, and any subtractions from the crust are the sum of upper and lower crust.

However, not all volcanics of the southern central Andes are basalt. Felsic melts are thought to have originated from crustal heating accompanying the

arrival of asthenospheric mantle beneath thickened crust. Significant ignimbrites of the southern Puna plateau are thought to occur as a consequence of a heat influx from the asthenosphere (Riller et al., 2001). These melts are an indicator of dramatic and possibly sudden lithospheric thinning.

Shortening deficit:

It is assumed that a thicker continental crust should be associated with the convergence of two plates where vertical thickening occurs from horizontal crustal shortening. Exceptions occur though, such as in the central Andean plateau. If high topography, supposedly caused by horizontal shortening, is accompanied by unusually thin lithosphere, the region is considered to have a shortening deficit. Moreover, measured shortening values from lithospheric thickness cannot solely account for such areas of high elevation.

Shortening values differ along the Andean margin as shown by Figure 1.4. Isacks (1988) used a shortening model to predict specific shortening values for different latitudes and compared these values to actual shortening. A calculated prediction curve was identical to the actual measured curve with some exceptions. North of 27°S, excess elevation is attributed to thermal isostasy where the subducting and overriding plates are decoupled. Elevation deficiencies in this same region occur from excess material removal of the Amazonian drainage system. However, south of 27°S at the southern end of the Puna, excess elevation is again noted. The shallowly subducting Nazca Plate is coupled to the overriding plate here, and isostatic rising cannot occur (Isacks, 1988). At this

point, the elevation (actual) is too high to account for the modeled (predicted) shortening. Thus, a shortening deficit is apparent.

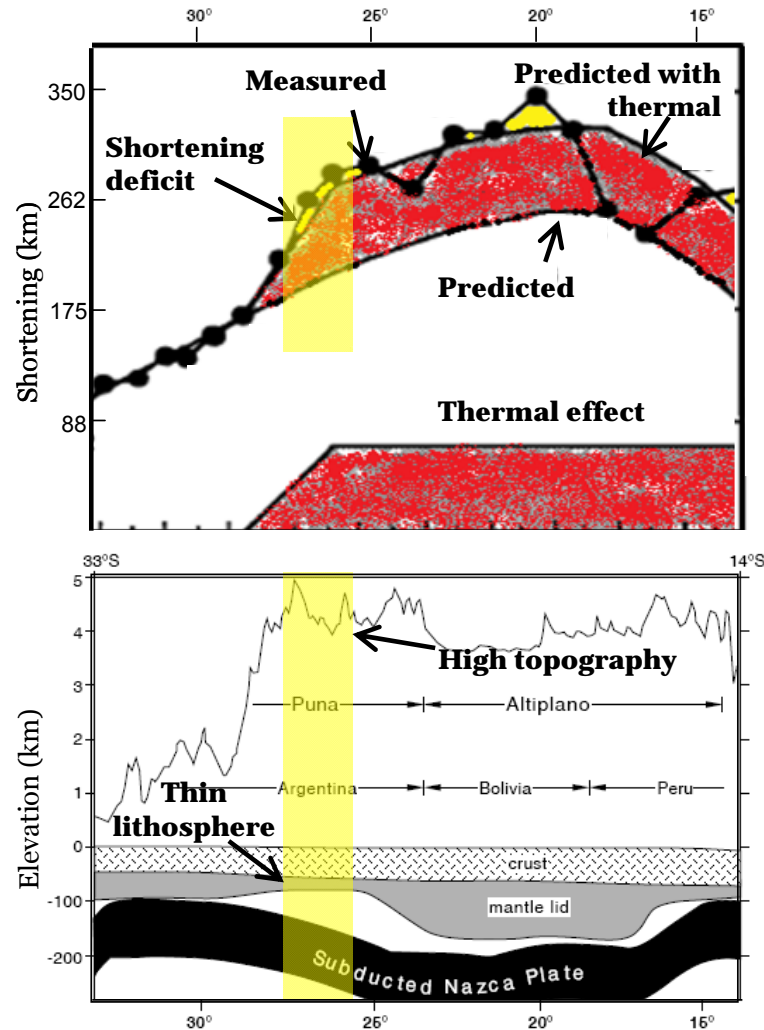


**Figure 1.4.** Shortening variation along the Andean margin. A thinner lithosphere beginning at  $\sim 27^\circ\text{S}$  combined with high topography makes for a shortening deficit along the region of the southern Puna plateau. At this region, predicted shortening values cannot account for measured shortening values, and a deficit is noted. Excess elevation north of  $27^\circ\text{S}$  is attributed to thermal isostasy, and elevation deficiencies are caused by excess material removal throughout the Amazonian basin (Modified after Isacks, 1988; Allmendinger et al., 1997).

### Subduction transition zone:

The southern Puna plateau is located at a subduction transition zone where subduction occurs normally to the north beneath the Altiplano and northern Puna, shallows through the transition zone in the southern Puna near 28°S, and becomes almost horizontal beneath the flat-slab region of Chile. The flattening transition region can be thought of as a 'bench' that occurs at a depth of 100 to 150 kilometers. The greatest number and largest young mafic back-arc flows occur above this 'bench' from a depth of 120 to 150 kilometers (Cahill and Isacks, 1992).

### Seismic gap:

The volcanic centers of the southern Puna plateau transition zone occur over the center of a supposed seismic gap occurring between 24.5°S and 27.5°S (Kay et al., 1994; Fielding, 1989). This gap may possibly reflect the lack of seismic stations in the southern Puna. However, if a seismic gap does exist, the gap signifies decoupling of the subducting slab from the overriding plate, creating a zone where earthquakes cannot occur because of such high temperatures. Greater heat in the southern Puna plateau was probably caused by an asthenospheric influx, led by the steepening of the subducting Nazca Plate. This directly relates to the extensive ignimbrite volcanism covering the area (Riller et al., 2001).

## **Lithospheric thinning**

The four attributes of the southern Puna plateau described in the previous section imply the occurrence of lithospheric thinning. Studies of mantle seismic attenuation (high-frequency wave propagation efficiency) structure also suggest that lithospheric thickness beneath the Puna is less than that of the Altiplano. Whitman et al. (1992) found that a higher attenuation (lower Q) exists for seismic waves traveling through the Puna plateau, and the Altiplano plateau has a lower attenuation (higher Q) with high attenuation only occurring under the main volcanic arc. This suggests that the continental mantle lithosphere is possibly thinner (<100 kilometers) and hotter underneath the southern Puna compared to the Altiplano (>150 kilometers) (Whitman et al., 1993, 1996; Kay et al., 1994). However, the data set of Whitman et al. (1993) is limited in its resolution due to a lack of seismic stations in the southern Puna.

During the Early Miocene to Recent, the subducting slab beneath the southern Puna plateau neither steepened nor flattened. Disregarding other processes, the lithosphere should be thicker than it currently is, since a thinner lithosphere is associated with shallow subduction zones. Kay and Kay (1993) state,

“One possible explanation is that the compression that caused Puna uplift produced a structurally thickened dense lower crust and upper mantle. Upon attaining a critical amount of shortening, this lithosphere became denser than the underlying asthenosphere, resulting in a catastrophic delamination event centered in the southern Puna.”

Moreover, crustal extension is limited in the Puna and cannot account for thinning, which further suggests an episode of delamination.

## DELAMINATION

Kay and Kay (1993) state that the process of delamination involves a quick break of the lower lithosphere into the asthenospheric mantle. The system is driven by density instability as hot asthenospheric mantle of low density material replaces higher density, colder lithosphere. Kay et al. (1994) speculate that a portion of the continental lithospheric base beneath the Puna plateau delaminated and returned to the mantle into the convection system during the Miocene (Figure 1.5). This removal of lithosphere would account for observed lateral thickness changes (Whitman et al., 1992).

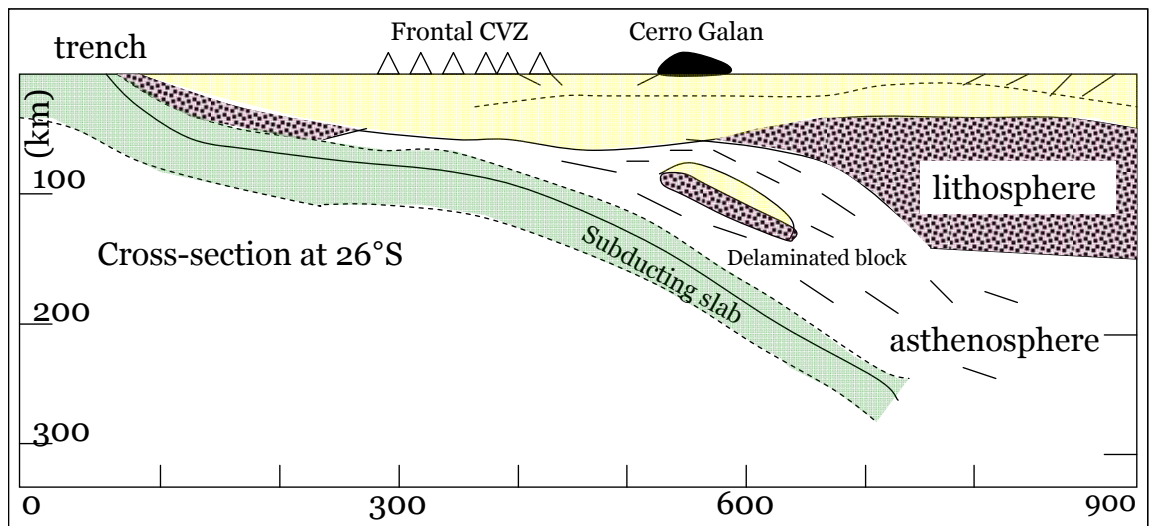


**Figure 1.5.** Delamination model. The delaminated block is shown to contain both mantle and crustal lithosphere as mantle lithosphere is missing beneath the main volcanic zone. Material of the delaminated block returns to the asthenospheric circulation system. The supposed region of lithospheric separation occurs at 26°S beneath the Cerro Galan ignimbrite and involves an eclogitic crustal transition (Modified after Kay et al., 1994).

## **Original models**

Models describing delamination were originally created for the western US and Tibet. In these models, delamination occurred as an effect of a fast increase in mantle temperature where the hot, deep, asthenospheric mantle advects to shallower depths. Rapid uplift and heightened production of magma have led to this conclusion (Kay and Kay, 1993). Meanwhile, the less dense underlying asthenosphere replaces the lowermost mantle lithosphere and releases potential energy to begin the process of delamination. Mantle lithosphere becomes gravitationally unstable after an increase in thickness and finally detaches. Elevation rapidly increases, basaltic volcanism commences, and the general stress regime in the crust changes from compressional to extensional (Whitman et al., 1996). The region of thinner lithosphere beneath the Puna plateau has undergone this sequence of events.

## **Modified model**

While original delamination models were applied to the central Andes because of similar features, those models have been modified to include a change in composition within the lithosphere. Regions with thicker crust (>50 kilometers) will increase in lower crustal density as basaltic compositions undergo an “eclogitic” phase transition. A mantle melt where 10 percent solidifies to eclogite causes a one percent increase in density (Kay and Kay, 1993). Hence, the detachment of a piece of lithosphere is more likely. Because a basaltic

lower crust will negatively contribute to buoyancy, it should also be involved in delamination of the lithospheric mantle.

In addition to density contrasts from mantle compositional changes, the upper lithosphere can become unstable above a stable lower lithosphere during compression. If a critical amount of shortening is reached, excess thickening of the lithosphere will result in a delamination event (Kay and Kay, 1993). Both of these factors have led to a hypothesis of delamination beneath the southern Puna.

### **Indicators**

Because of short duration, a delamination event is difficult to observe. However, general observations have been made regarding the effects. Besides lithospheric thinning, indicators of a delamination episode include volcanism and a change in stress orientation (Kay and Kay, 1993). These features are illustrated in the southern Puna plateau.

#### Volcanism:

One line of evidence for a delamination event includes the initiation of mafic volcanism. Throughout the Puna plateau, most of the volcanics are silicic andesites and dacites from ignimbrites. These intermediates formed from crustal melting during plateau uplift and crustal thickening; however, back-arc calc-alkaline and shoshonitic group lavas in the Puna mark the onset of mafic volcanism and imply a mantle addition (Kay et al., 1994).

### Stress orientation:

A second condition involves a change in the regional stress system. Fault kinematic studies show that Miocene to early Pliocene volcanic rocks of the Puna erupted during E-W crustal shortening as calderas lie along a NW-SE-striking fault system. However, the entire Puna plateau seems to have been affected as the deformation regime underwent a local change from vertical thickening to orogen-parallel extension of the upper crust. Later erupted mafic back-arc lavas illustrate this behavior as they are associated with a different, more complex system of extensional to strike-slip faults (Kay et al., 1994).

### **Delamination beneath the Puna**

The southern Puna plateau illustrates features of delamination as the regional stress system underwent a major change 2 to 3 m.y. ago, and mafic volcanism became prominent after this stress change (Kay and Kay, 1993). Kay and Kay (1993) suggest that the region of the southern Puna plateau exhibiting the most extensive mafic volcanism marks the location of thickened mantle, hence, crustal lithospheric delamination. Kay et al. (1994) suggest that lithospheric delamination of the southern Puna occurred during the Pliocene. The timescale for this event is short, and the origin is thought to be density driven rather than a longer lasting convective thinning. The delamination model proposed by Kay et al. (1994) suggests that one or more pieces of detached continental lithosphere beneath the southern Puna plateau at 26°S were replaced by asthenosphere.

## **ANISOTROPY AND MANTLE DEFORMATION**

Anisotropy is a property of a material being directionally dependent; seismic anisotropy is the directional dependence of seismic wave speeds. Elastic waves exhibit seismic anisotropy in an Earth medium when they travel in one direction faster than another. In anisotropic media, local propagation direction determines seismic velocities, and wave type and local symmetry of elastic properties determines polarization (Babuska and Cara, 1991). Seismic anisotropy can be detected both in the crust and the mantle, but the generating mechanism of anisotropy within each region is different.

Seismic anisotropy of the uppermost crust is induced by cracks, faults, and stress fields. Almost any rock can contain small cracks. If the cracks are distributed in a coherent spatial alignment, the rocks can behave with elastic anisotropy even if the rocks are seismically perfectly isotropic. Anisotropy in this case occurs from a decrease in velocity mainly normal to the plane in which cracks are oriented. The phenomenon of fluid-filled cracks, microcracks, and pores preferentially aligning in the crust is known as extensive-dilatancy anisotropy (EDA). The details of crack geometries can be determined from propagating shear-waves, which becomes indicative of current stress fields (Babuska and Cara, 1991).

Mantle anisotropy specifically refers to strain-induced preferred orientation of mantle minerals (Figure 1.6) (Savage, 1999). The plastic and

viscous flow of the mantle acts as the primary mechanism that orients the minerals and causes seismic anisotropy (Babuska and Cara, 1991). The upper mantle is mostly comprised of the mineral olivine which develops a definite fabric called lattice-preferred orientation (LPO) in response to finite strain (Sandvol and Ni, 1997). For a peridotite aggregate of about 70 percent olivine, LPO results in a 3-6 percent average anisotropy for shear waves (Russo and Silver, 1994). Seismic anisotropy within the mantle is generally accepted as occurring from this preferred orientation of crystals produced by deformation (Ribe, 1989).

Within the upper mantle, two types of deformation exist: diffusion creep and dislocation creep. Diffusion creep refers to a solid-state migration occurring across a crystal lattice or between grain boundaries (Savage, 1999). Deformed material of this type is considered isotropic because preferred mineral orientation has not developed. Diffusion creep occurs in low stress environments involving smaller-sized grains. The second deformation type, dislocation creep, is defined by Savage (1999) as crystalline motions where there is a discontinuity in lattice structure. This deformation type leads to seismic anisotropy in olivine aggregates because it does cause preferred mineral orientation. Dislocation creep plays an important role in high strain asthenospheric flow regions near ridges and subduction zones (Babuska and Cara, 1991).

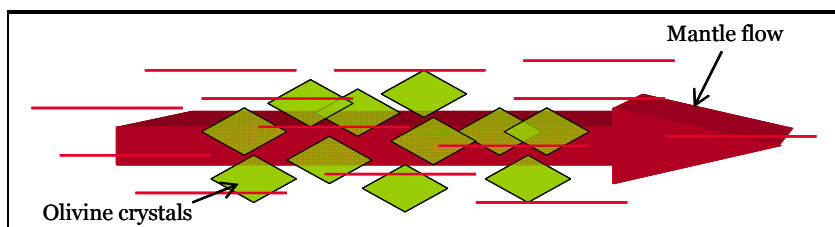


**Figure 1.6.** Mantle anisotropy. Olivine develops a fabric of LPO in response to finite strain or asthenospheric flow.

The coherence of finite strain fields as well as the type of deformation occurring determines the behavior of anisotropic fabric. General strain in olivine aligns the  $a$ ,  $b$ , and  $c$  axes with extension, compression, and intermediate strain ellipse axes, respectively (Savage, 1999). When olivine deforms at upper-mantle pressures and temperatures, the fast direction of anisotropic propagation tends to align along the  $a$  axis of single olivine crystals to exhibit total crystal alignment, or deformation along the flow line (Ribe, 1989).

Different factors can slightly alter anisotropy. Higher temperatures and pressures cause increased diffusion and mobility of grains so that only specifically oriented grains can flow, enhancing preferred orientation. Furthermore, partial melting encourages a transition between dislocation creep and diffusion creep, preventing the formation of preferred orientation. Preferred mineral orientation is a function of strain history as well because anisotropy intensifies with increasing time and strain extent. Finally, anisotropy can vary with slight changes in composition like rock alterations and orientation with respect to the foliation plane (Savage, 1999). Although the degree of anisotropy depends on surroundings, mantle strain must initiate mineral orientation.

Seismic anisotropy causes shear-wave splitting, and based on the orientation and depth extent, measurements of shear-wave splitting can be used to infer mantle strain fields. Thus, a relationship can be made between strain and anisotropy, and we can infer mantle strain patterns. From this, the amount of anisotropy caused by past and present lithospheric deformation can be determined as well as the amount caused by sources related to the crust, upper

mantle, and/or lower mantle (Savage, 1999). While shear-wave splitting measurements have become common-place, the interpretation of tectonic processes deduced from splitting parameters has not been fully resolved as the method of data calculation is continuously revised.

## CHAPTER 2: The Method of Shear-Wave Splitting

### SHEAR-WAVE SPLITTING

A process called shear wave birefringence, or shear wave splitting, occurs when seismic shear waves undergo multiple polarizations, and components move at different speeds. Shear-wave splitting takes place when a shear wave passes through an anisotropic medium. P-wave particle motion travels in the direction of wave propagation, and S-wave particle motion travels perpendicular to this. The splitting of S-wave motion involves a time separation occurring with increasing forward P-wave motion.

Shear-waves have two components, SV and SH. The vertical SV-component combined with the wave vector, or P-wave, make up the plane of incidence (Figure 2.1). This plane lies in both the direction of propagation and direction towards the source. The horizontal SH-component is oriented orthogonal to

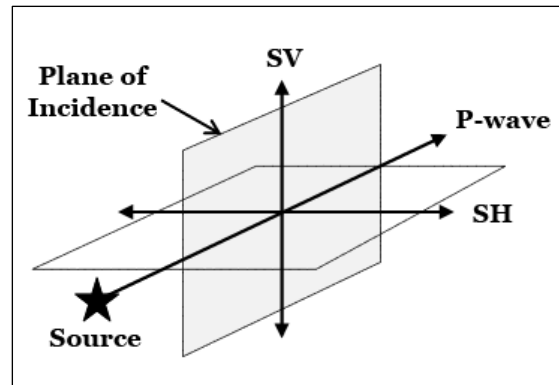


**Figure 2.1.** Seismic wave components. SV- and P-wave components lie in the plane of incidence and point in the direction of wave propagation. The SH-wave component is oriented orthogonal to SV and lies in the horizontal plane.

SV and the plane of incidence. Shear-wave phases used in this study include SKS,

SKKS, and PKS (Figure 2.2). These phases travel through the outer core as P-waves and convert to S-waves upon mantle re-entry. Because of this, shear-wave splitting must occur in the mantle between S-wave conversion and surface arrival.

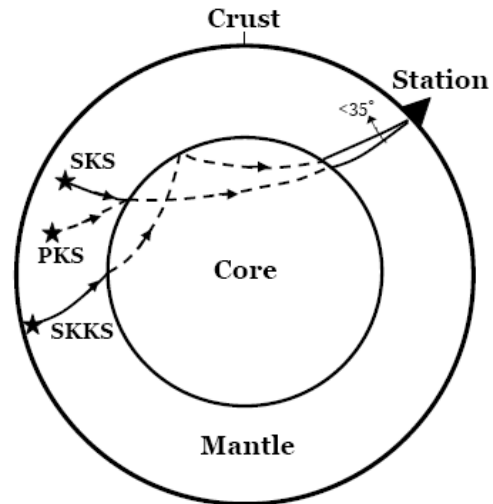


**Figure 2.2.** Shear-wave phases. Teleseismic phases used in this study include SKS, SKKS, and PKS. These phases all pass through the outer core before re-entering the lower mantle to initially polarize isotropically. P-waves are shown by a solid line, and S-waves are shown by a dashed line (Modified after Savage, 1999).

It is assumed that most shear-wave splitting does not occur in the lower mantle as the lower mantle is considered to be largely isotropic (Savage, 1999).

Minerals of the lower mantle do not

usually develop a strong preferred orientation, and anisotropy cannot be detected. Therefore, we assume that most shear-wave splitting occurs in the upper mantle, and polarization after S-wave conversion will be in the direction of wave propagation. If anisotropic material is encountered in the upper mantle, a shear wave will re-orient itself into two polarization directions as shown in Figure 2.3: a fast direction parallel to the direction of fast-axis polarization of the mineral and a slow direction that is perpendicular to the fast polarization direction. This process of shear-wave splitting is equivalent to birefringence of light rays. By finding the fast polarization direction ( $\phi$ ) and the delay time ( $\delta t$ ) between two arriving shear-wave components, the principle axes of strain orientation can be constrained (Russo and Silver, 1994).

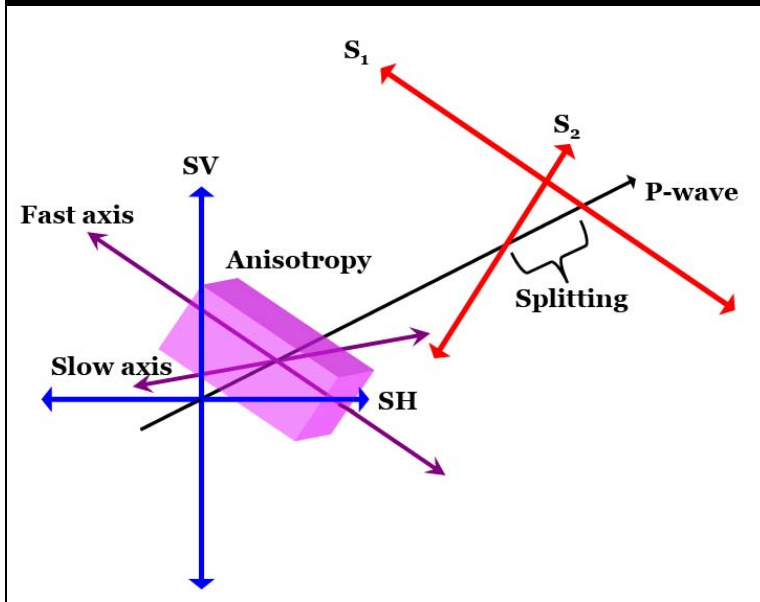


**Figure 2.3.** Shear-wave splitting. If a seismic wave encounters an anisotropic medium, the SV-component will align parallel to the fast polarization axis ( $S_1$ ), and the SH-component will align orthogonal to the fast axis ( $S_2$ ). Although  $S_1$  parallels the fast axis,  $S_2$  does not necessarily parallel the slow axis. Splitting between the fast and slow components occurs with increasing P-wave motion. The magnitude of splitting between  $S_1$  and  $S_2$  depends on the strength and extent of anisotropic material.

The two re-oriented polarizations of a shear-wave will travel at different speeds that depend on the properties of the anisotropic medium and the direction of wave propagation through the medium (Savage, 1999). Specifically, the delay time ( $\delta t$ ) between a fast component ( $S_1$ ) and slow component ( $S_2$ ) is dependent on the magnitude of travel through the anisotropic medium of the wave path as well as the difference in speeds. Delay time is shown by

$$\delta t = L(1/V_{S1} - 1/V_{S2}), \quad (\text{Eq. 2.1})$$

where  $V_{S1}$  and  $V_{S2}$  represent the speeds of  $S_1$  and  $S_2$ , respectively, for a certain propagation direction within anisotropic material.  $L$  defines the path length of the wave passing through anisotropic material. These different speeds for  $S_1$  and  $S_2$  can also be used to find percent anisotropy ( $k_s$ ) as described in Savage (1999) as

$$k_s = 200(V_{S1} - V_{S2})/(V_{S2} + V_{S1}). \quad (\text{Eq. 2.2})$$

Percent anisotropy is similar but different from intrinsic anisotropy, which is a measure of the percent difference between fast and slow velocities. Because of the dependence on propagation direction, intrinsic anisotropy values of a material are generally higher than percent anisotropy values. Nevertheless, these values as well as delay times are dependent on how fast different polarizations travel.

At teleseismic distances, an incoming raypath beneath a seismic station possesses a nearly vertical propagation direction, where the plane containing  $S_1$  and  $S_2$  is nearly horizontal. Assuming the Earth is spherically isotropic, the incident S-wave will polarize in the vertical plane, or the radial direction on the surface. The transverse direction is perpendicular to this in the absence of anisotropy. The radially directed S-wave can be represented by  $S(t)$ . Assuming anisotropy occurs, the fast and slow polarization directions projected onto the surface are represented respectively as

$$S_1(t) = S(t) * \cos \phi, \quad (\text{Eq. 2.3})$$

$$S_2(t) = S(t - \delta t) * \sin \phi \quad (\text{Eq. 2.4})$$

where  $\phi$  is the angle of fast polarization direction measured from the radial direction as shown in Figure 2.4 (Babuska and Cara, 1991). The direction towards the source is also called the back azimuth (BAZ), where the BAZ is the angle measured from North to the source. Essentially, the radial direction is the same as the BAZ direction, and radial represents the polarization direction in a completely isotropic Earth. Silver and Chan (1988) show equations illustrating

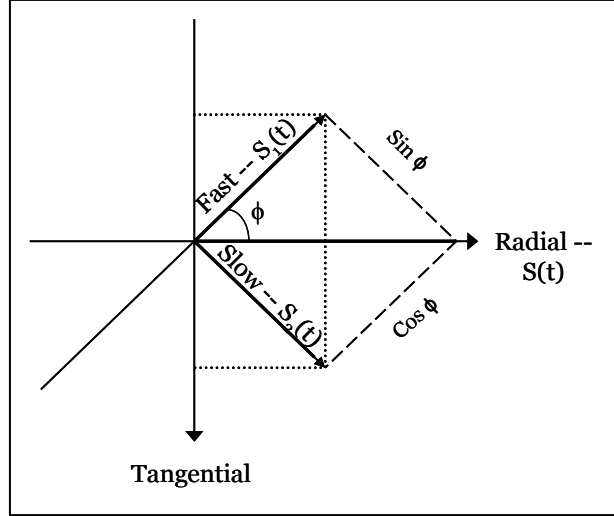


**Figure 2.4.** Surface projected fast and slow polarization directions. The radial propagation direction is represented by  $S(t)$ , fast polarization direction by  $S_1(t)$ , and slow polarization direction by  $S_2(t)$ .  $\phi$  represents the angle between fast polarization direction and radial direction (Modified after Babuska and Cara, 1991).

radial  $u_R(t)$  and transverse  $u_T(t)$  components of the two projected polarized components as

$$u_R(\phi, t) = S(t) \cos^2 \phi + S(t - \delta t) \sin^2 \phi \quad (\text{Eq. 2.5})$$

$$u_T(\phi, t) = -\frac{1}{2} [S(t) - S(t - \delta t)] \sin(2\phi). \quad (\text{Eq. 2.6})$$

These equations describe the motions of split shear waveforms, but the splitting parameters  $\phi$  and  $\delta t$  must be known to determine these motions. Shear-wave splitting parameters can then be used to find the direction of asthenospheric flow, as well as depth extent and magnitude of anisotropy in a given flow region (Russo and Silver, 1994; Silver and Chan, 1988).

## MEASURING SPLITTING PARAMETERS

Since we observe the effects of shear-wave splitting on recorded seismograms, an ideal method for measuring splitting parameters involves correcting split waveforms on these seismograms. In effect, we globally search

for a pair of splitting parameters,  $\phi$  and  $\delta t$ , that most successfully removes the effects of anisotropy and returns the seismogram to its initial isotropic polarization of  $S(t)$ . These splitting parameters can be found using the method of Silver and Chan (1991) from the covariance matrix of particle motion in the horizontal plane. After solving for the eigenvalues of the matrix, the linearity of particle motion can be measured. This linearity can be viewed on particle motion diagrams and will be discussed later in detail. The covariance matrix  $c_{ij}$  for two orthogonal components on the surface is shown by

$$c_{ij}(\phi, \delta t) = \int_{-\infty}^{\infty} u_i(\phi, t) u_j(\phi, t - \delta t) dt \quad (\text{Eq. 2.7})$$

$i, j = \text{radial, transverse.}$

This method for finding splitting parameters is best completed using a grid search for single events containing parameters of  $\phi$  from  $0^\circ$ - $180^\circ$  and  $\delta t$  from 0.0-6.0 seconds. Savage (1999) and Wüstefeld and Bokelmann (2007) summarize two techniques used for this search.

### **Rotation-correlation**

One approach initiated by Bowman and Ando (1987) uses a rotation-correlation method. With this method, the seismogram is rotated into fast and slow polarization directions using polarization diagrams for pairs of splitting parameters. A cross-correlation is performed between the two polarized components to find the time shift that produces the maximum cross correlation. The splitting parameters exhibiting the maximum cross-correlation are deduced

as the optimal splitting parameters. In short, this method essentially searches for splitting parameters that illustrate waveforms behavior most similar to corrected waveform shapes. Both short- and long-period wavelengths can be used in the rotation-correlation method.

### **Grid search**

Silver and Chan (1991) use another approach which uses the observed radial component to model the expected corrected component. With this method, a grid search is first performed for splitting parameters finding the most singular covariance matrix from eigenvalues without assigning errors. The corrected radial and transverse seismograms are created from these parameters, and the energy contained within the corrected transverse component is plotted on a contour diagram with a mark designating minimum energy. This energy on the transverse component is shown as

$$E_T(\phi, t) = \int_{-\infty}^{\infty} \tilde{u}_T(t)^2 dt \quad (\text{Eq. 2.8})$$

where  $\tilde{u}_T(t)$  is the corrected transverse component. The minimum energy corresponds to the splitting parameters used in the creation of the corrected seismograms, and contours around the minimum form an error margin. This method can only be used for longer period teleseismic phases where short-period energy has been attenuated in the mantle. Long-period S-phases have been radially polarized, so any magnitude of anisotropy will produce a time-dependent transverse component based on the radial component.

## Complications

These single-event methods are used while assuming that only one homogeneous layer of anisotropy exists. Multiple layers of anisotropy are sometimes detected using the effects of splitting parameters. Graphs comparing splitting parameters to BAZ directions show whether different source directions are causing variable results (Savage, 1999). If one radially polarized shear phase is split once, it will produce both fast and slow polarized components. If each of these split components encounters another layer of anisotropy, another split into fast and slow polarized components will occur (Figure 2.5). Two fast polarized and two slow polarized components result. When plotted in this manner, multiple anisotropy layers display symmetrical patterns.

The vertical resolution of shear-wave splitting is considered poor even with dense arrays because of difficulty determining the depth extent of detected anisotropic layers using only teleseismic core phases. However, splitting parameters provide excellent lateral resolution, and techniques such as those just described can work around the difficulties of vertical resolution. This study attempts to vertically constrain the depth of mantle anisotropy for better

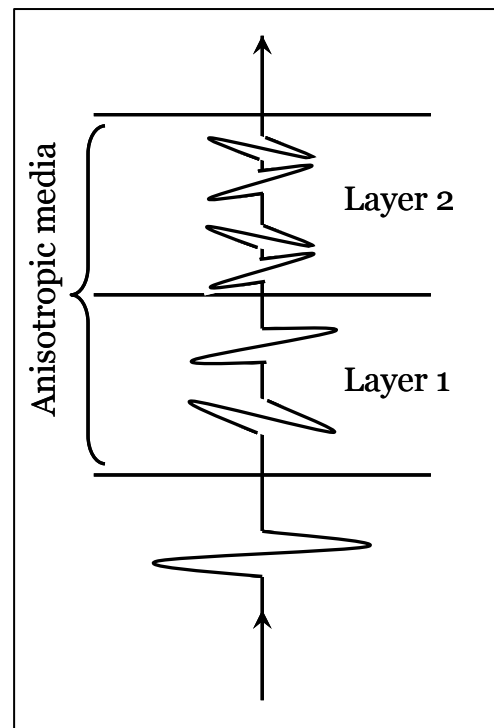


**Figure 2.5.** Multiple layers of anisotropy. If a shear wave encounters multiple layers of anisotropy, each component will split accordingly. (Modified after Savage, 1999).

interpretation by using teleseismic events in conjunction with local deep and intermediate events having hypocenters of known depth. Final splitting parameters are also compared to BAZ measurements to determine if an azimuthal dependence exists. Multiple studies have used these methods to acquire dependable results (e.g. Sandvol et al., 1994; Sandvol and Ni, 1997; Polet et al., 1999; Smith et al., 2001; Long and van der Hilst, 2006).

### **PUNA SEISMIC ARRAY**

The PUNA seismic array entirely consists of 43 US and 30 German stations, but this study only focuses on data from the US stations (Figure 2.6). Of these stations, 31 broadband and 12 short-period stations constitute an area greater than 96,000 square kilometers, centered at  $\sim 27^{\circ}\text{S}$ ,  $68^{\circ}\text{W}$ . Two separate components of the array are used for imaging lithospheric structure. The first component is a north-south transect combined with an east-west transect to form a plus (+) shape. Stations within these transects are closely spaced ( $\sim 10$  kilometers) and primarily contain intermediate-period sensors. The second component of the array consists of a 2-D grid of broadband sensors with larger spacing ( $\sim 50$  kilometers) that surrounds and includes the two previously mentioned transects. Broadband seismometers can detect motion over a wide range of frequencies and are useful for recording signals from regional and teleseismic earthquakes including longer period surface waves. Intermediate-period seismometers detect motion over higher frequencies and are best used for

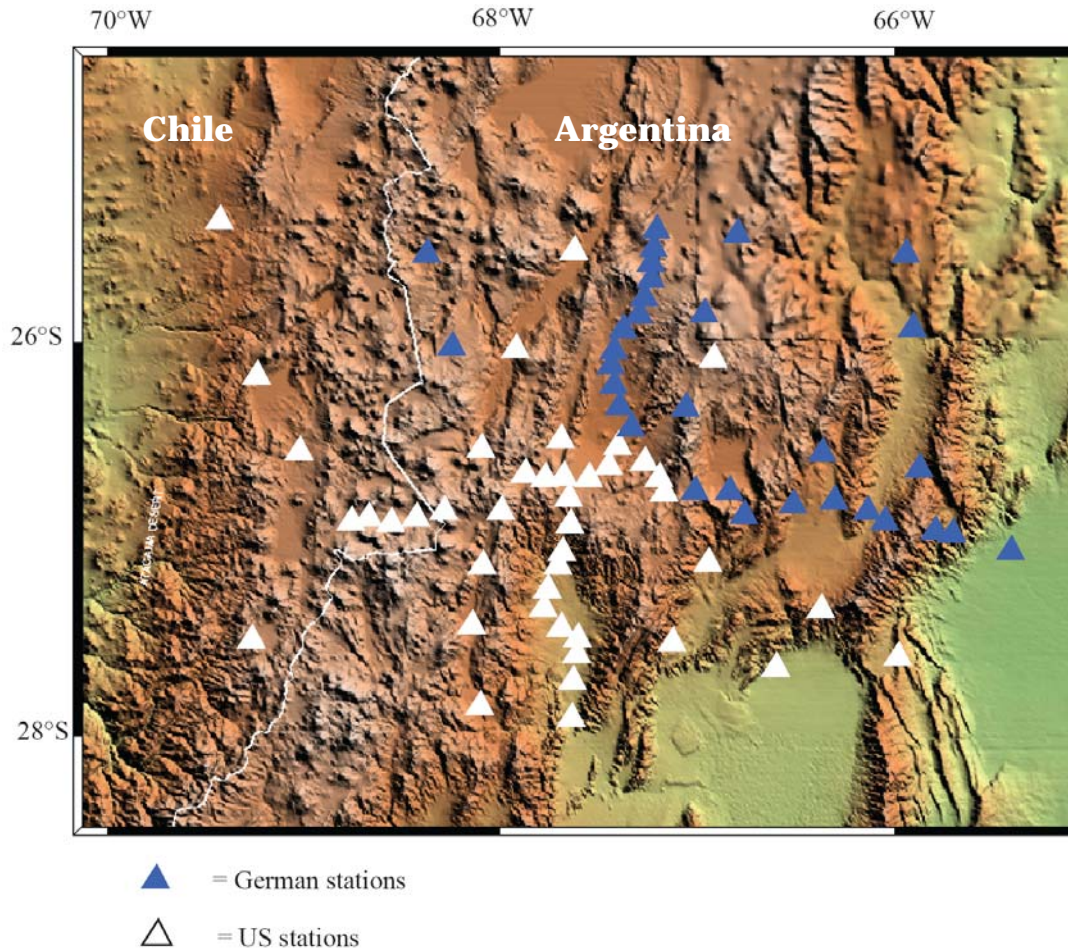


**Figure 2.6.** PUNA seismic array station map. A total of 73 stations comprise the array with white triangles representing US-run stations and blue triangles representing German-run stations. A N-S, E-W transect comprises one component, and a 2-D grid comprises a second.

recording body waves such as SKS and PKS. These two combined array components allow 3-D imaging of large-scale (~75 kilometers) structure and the denser station spacing of the two transects allows for higher resolution imaging.

## Installation

For this research, stations were deployed for ~16 months beginning in December 2007. Field service runs and data collection occurred every five to six months after the installation of the seismometers. Sensors were placed into holes of one cubic meter dug from ground surface (Photo 2.1). These sensors included Streckeisen STS-2, Guralp CMG-3T, CMG-40T, Nanometrics Trillium 40, and Trillium 120 second three-component sensors. They were placed on concrete pads and protected by a styrofoam casing covered with plastic. Dirt and small rocks on top provided extra protection. Sensors were connected by cables to digital seismograph recorders including either REF TEK 130 or Nanometrics Taurus dataloggers. Data was recorded continuously onto two 2-Gbyte disks for REF TEK 130 recorders and one 4-Gbyte disk for Taurus recorders at 50 samples per second (sps) or 40 sps as a default. Data recorded at this period has a high enough resolution to accurately locate local events as well as

**Photo 2.1.** Installation of NS08. Sensors were placed in holes that were dug one meter deep into the ground and connected to seismometers in separate holes by cables. Solar panels supplied the main power to the instruments, and a battery provided backup power. Recordings were kept in UTM time with GPS units.



teleseismic events. The recorders and backup batteries were encased by a box that was covered with plastic and dirt on top. Solar panels supplied the main power for the seismometers and charged internal batteries to 14.2V. The seismometers also connected to GPS units that kept signals correct to UTM time within a few microseconds.

Stations of the PUNA seismic array were mostly installed in extremely remote areas. Conditions of the Puna plateau sometimes caused difficulties in servicing particular stations (Photo 2.2). However, quiet locations provide excellent signal quality, and stations usually have fewer problems. Much care was taken in avoiding pitfall locations, but some regions were unavoidable as the importance of the research depended on certain station positions within the array (Photo 2.3).



**Photo 2.2.** Surprise river crossing. Climate conditions of the Puna Plateau are harsh and sometimes caused difficulties in reaching specific stations during service runs. Rainfall caused this river to form where a road used to exist for crossing.

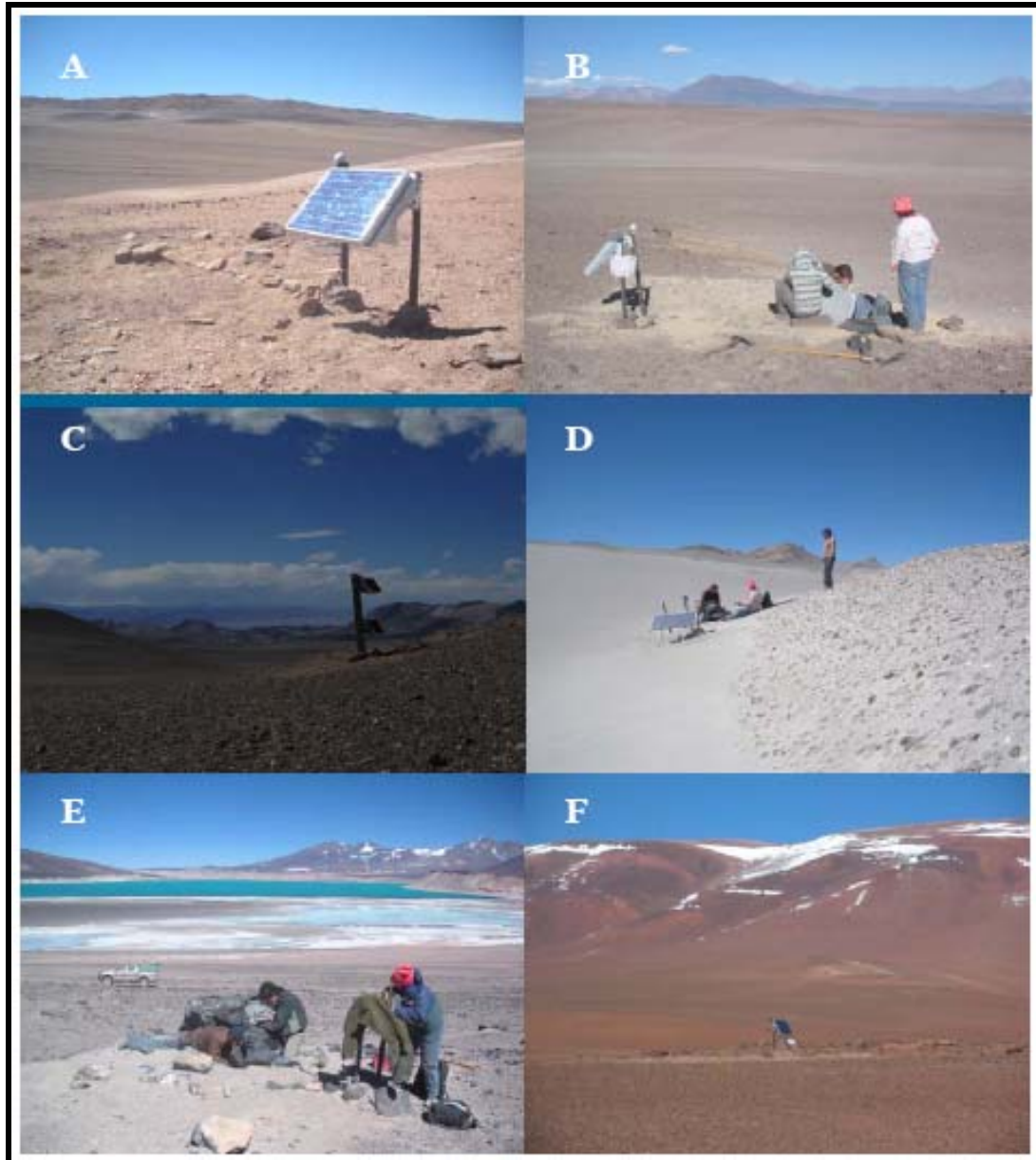


**Photo 2.3.** Example station locations across the Puna. A. Station BB23 located in the Atacama Desert. B. Servicing station BB22 in the sandy wind. C. Trusty station EW10 produced good results. D. Peaceful NSO6 within a giant sand dune. E. Bright blue lagoon near EW17. F. BBO3 resting in a Chilean National Park.

### **Neighboring experiments**

Several geophysical studies have been carried out in the central Andes, and the southern Puna serves as an important one within a transition region. The PUNA seismic experiment pioneers research for the southern Puna plateau

though as no seismic stations have previously existed for this particular area. Furthermore, the PUNA seismic array is one of the few to study along-strike lithospheric variations. Some previous studies include the BANJO, SEDA, PISCO, and CHARGE seismic experiments shown in Figure 2.7 (Polet et al., 2000; Gilbert et al., 2006). North of PUNA, the BANJO experiment consisted of an east-west line of broadband seismometers at 20°S latitude. This network

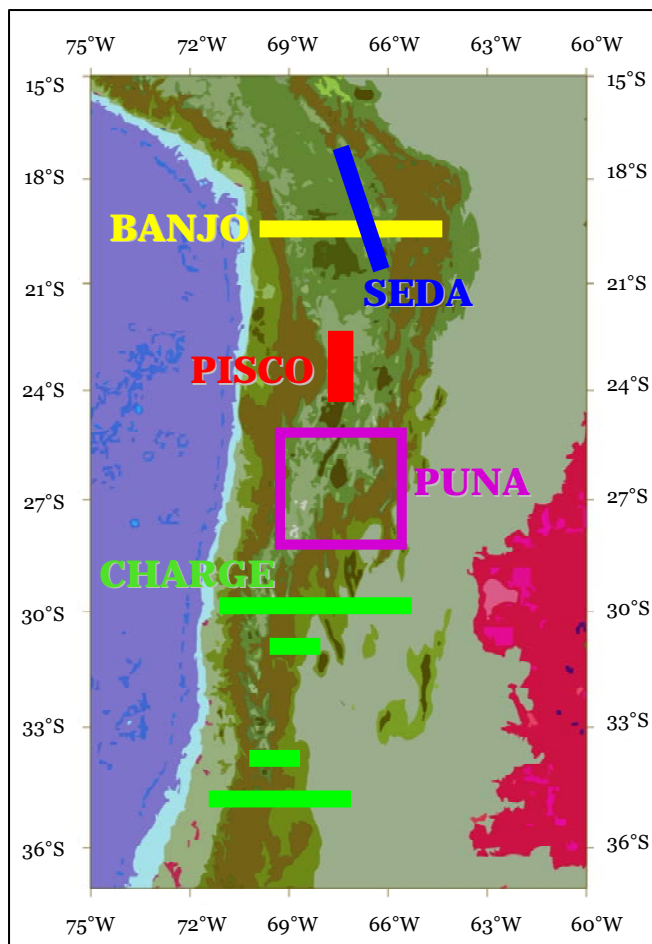


**Figure 2.7.** Neighboring seismic experiments. Locations of nearby completed seismic experiments include but are not limited to: BANJO (yellow), SEDA (blue), PISCO (red), and CHARGE (green). PUNA (pink) is shown for reference.

spanned ~1,000 kilometers from the western Cordillera through the Chaco plain and was deployed from March 1994 to September 1995. The SEDA experiment ran roughly perpendicular to BANJO for 350 kilometers at 67°W and consisted of short-period seismometers. SEDA was located along the eastern boundary of the Altiplano and operated from April 1994 to May 1995. The PISCO network was located at 68°W and ran through the Atacama Desert in northern Chile. PISCO consisted of both broadband and short-period

instruments and operated from February 1994 to May 1994. The CHARGE array was located south of PUNA in four main east-west transects across the Andes and Sierras Pampeanas. CHARGE broadband seismometers operated from November 2000 through May 2002. Results of some of these studies will be discussed and compared with the results of the PUNA seismic experiment in Chapter 3.

## **DATA PROCESSING**

### **Raw data**

Once data has been recorded and collected from the field, data processing for the PUNA experiment begins with converting raw data files to MiniSEED format using Antelope software. MiniSEED is a subset of SEED (Standard for the Exchange of Earthquake Data), which is a standard seismic data format for all seismologists to use and share. Events needed for the experiment can be extracted from MiniSEED format, and specific events are found within an earthquake catalog using search parameters. Since this study utilized both teleseismic and local events, two separate searches were performed. For teleseismic events, we searched for all earthquakes having a body wave magnitude of 5.6 or greater and a source distance of  $85^{\circ}$ - $180^{\circ}$  from the center of the array. For local events, we performed a grid search for all earthquakes having any body wave magnitude, a depth of 100-700 kilometers, and a source distance

of less than  $5^\circ$  within a grid from  $23^\circ\text{S}$ - $31^\circ\text{S}$  latitude and  $63^\circ$ - $73^\circ\text{W}$  longitude. From these parameters, two lists of events were produced.

These events were extracted from MiniSEED files using a 4,500 second time window for teleseismic events and a 500 second time window for local events. This extraction generates data in SAC (Seismic Analysis Code) format. To reduce the number of samples within the signal, we decimated the files from 50 sps to 25 sps. A final step before viewing the actual seismograms included assigning headers using event data to automatically note where important phases were located according to arrival time. Following this initial processing phase, a manual inspection of the seismograms was performed.

### **Windowing**

To perform the shear-wave splitting correction method of Silver and Chan (1991), a shear-wave window was manually selected. A grid search was later performed to find the best correction parameters,  $\phi$  and  $\delta t$ . This method was used for teleseismic events. For local events, we used the method of Bowman and Ando (1987). A window was again manually chosen, and rotation-correlation of the seismogram followed. For either method, picking the shear-wave window was an important process. To start, a typical bandpass frequency filter of 0.1 to 4.0 Hz was applied to event recordings. Using a SAC macro, the shear-wave window was chosen by picking a start time and end time corresponding with the S-wave. For teleseismic events, we investigated SKS, SKKS, and PKS phases, and general S-waves were windowed for local events.

As mentioned in Teanby et al. (2004), the final calculated  $\phi$  and  $\delta t$  results are heavily influenced by the exact placement of the shear-wave window as well as the error. Cycle skipping can also occur with a poor window choice. Cycle skipping occurs when the amplitude of the first arriving wave is large enough for detection, but the amplitude of the second arriving wave is not. One or more cycles will be skipped until the amplitude reaches detection level. This phenomenon is caused by noisy data or by applying too narrow of a filter and results in multiple solutions for  $\phi$  and  $\delta t$  when only one pair should exist. To avoid the effects of cycle skipping and provide the best results, we chose a window start time 10-15 seconds before the start of the earthquake phase as shown in Figure 2.8. By including this main frequency for several periods, cycle skipping can be prevented. The end of the window should include one full period to maintain realistic errors, but it should not include secondary phases. With a careful windowing process, the best correction parameters can be estimated with minimal error.

### **Quality-control**

After windowing the S-waves, the data must pass quality-control inspection to verify the validity of the results. We used separate programs for the Silver and Chan (1991) method for teleseismic waves and the Bowman and Ando (1987) method for local earthquake waves. The output of the data for both programs is identical. Individual result files were produced for every station examined that gave the most ideal splitting parameters,  $\phi$  and  $\delta t$ , as well as

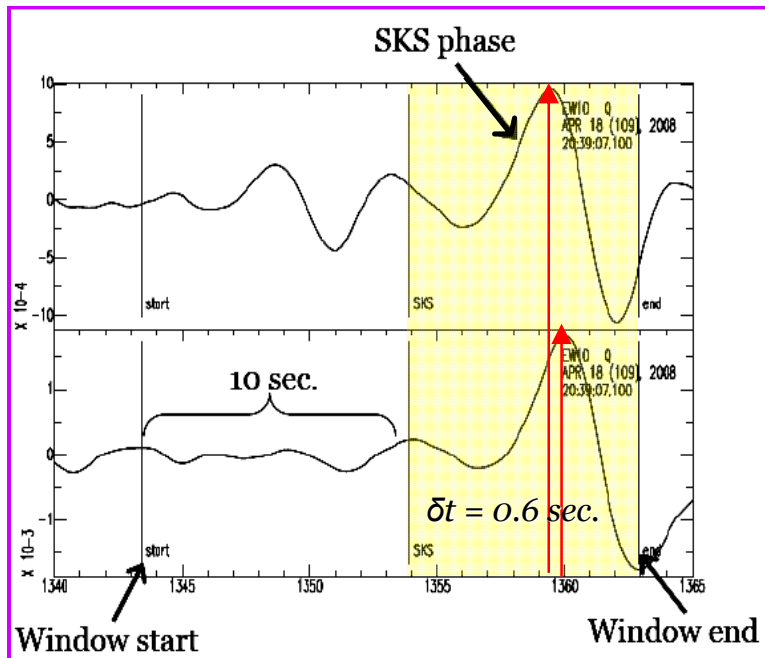


**Figure 2.8.** Window picking. The best SKS window starts 10-15 seconds before the phase arrival to avoid cycle skipping. The window should end by including one full period. Window picking is an important aspect of shear-wave splitting and directly reflects results.

associated errors, event identification, back azimuth, and source distance (delta).

Separate output files were also generated which contained the rotated fast and slow seismograms for each examined event, as well as a corrected seismogram. Finally,

energy files containing error estimations were generated. To quality-control the data, we checked four main effects of seismogram correction which include:

1. visibility of rotated fast and slow waveform splitting,
2. minimization of energy on the tangential component,
3. elliptical and linear particle motion,
4. one minimum energy value contained in the energy contour plot.

The output files mentioned above allowed us to check each of these four points in the quality-control process.

We used the fast and slow seismogram files to check for visible splitting of the waveform. These seismograms are the original horizontal seismic components that have been rotated by  $\phi$  degrees to the fast and slow directions. Visible splitting should be apparent between the two components as the fast component shows a phase arrival time slightly before that of the slow component (Figure 2. 9). The file containing the corrected seismogram component should also be used for comparison. The corrected file is simply the slow component (or tangential) that has been time-shifted by  $\delta t$  and finishes the shear-wave splitting correction. When comparing the corrected component to the fast component, the waveforms should be nearly identical if the splitting parameters are correct.

Quality-control of the teleseismic core phase splitting is very similar. For this check, we used the fast and corrected seismogram components and rotated them back to the BAZ, or

to the radial and tangential components. By setting the amplitude axis equal for both components, waveform amplitude should exist on the radial component while the tangential waveform is relatively flat in comparison. Since we

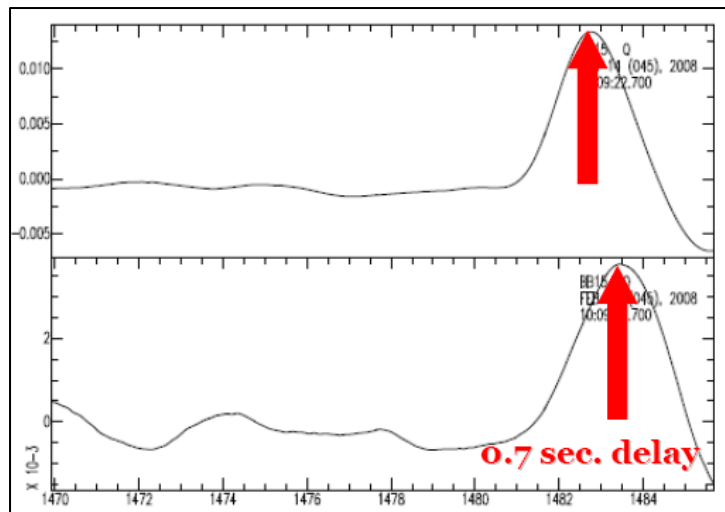


**Figure 2.9.** Visible splitting between fast and slow components. This teleseismic event recorded at station BB15 shows a 0.7 second delay between the two components of the seismogram. This completes the first quality-control check.

were looking at corrected seismograms containing potentially no splitting, all of the waveform energy should have been within the radial component (Figure 2.10).

The next quality-control check involves the inspection of particle motion plots. These plots involve fast, slow, and corrected seismogram components. A first plot involves the amplitude of the fast component versus the amplitude of the slow component. Since the amplitude of the fast component will increase before the amplitude of the slow component for an S-wave that is split, the particle motion is plotted as an ellipse. A second plot uses the fast component versus the time corrected slow component. There should be no time shift between these two components, so the amplitudes of both waveforms will increase and decrease at identical times. Particle motion between these components should plot rectilinear. When comparing these two separate plots, a

good split waveform is identified by an elliptical plot corresponding to the fast and slow components and a rectilinear plot corresponding to the fast and corrected components as exemplified in Figure 2.11. Two rectilinear plots indicate a waveform

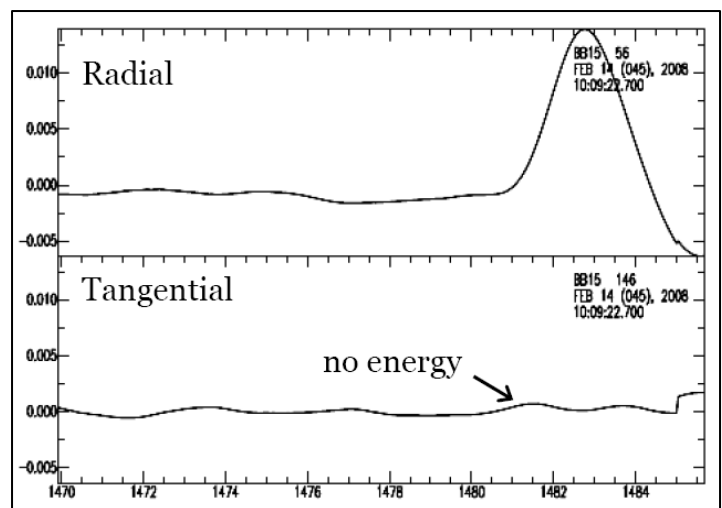
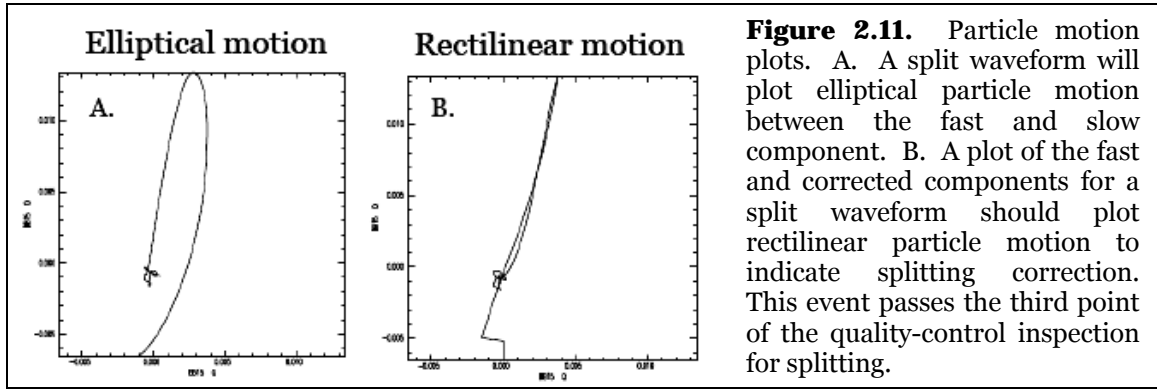


**Figure 2.10.** Waveform energy on seismogram components. Waveform amplitude exists on the radial component, but very little energy is visible on the tangential component for the corrected waveform. This event passes the second quality-control check for a split event.



contains no splitting.

A final step for a quality-control check of the data involves error analysis through energy contour plots. The generated energy files discussed earlier essentially contain a matrix of energy values, which measure the non-singularity between fast and corrected waveform components. These values originate from Eq. 2.7, the covariance matrix for a specific set of splitting parameters. As mentioned previously, Silver and Chan (1991) used a grid search to find these parameters. The covariance matrix of Eq. 2.7 has two eigenvalues associated with each set of splitting parameters. If splitting is present, these two eigenvalues,  $\lambda_1$  and  $\lambda_2$ , will both depict nonzero values. However, with an absence of anisotropy, only one nonzero eigenvalue will exist, or only one principle component of horizontal ground motion. This eigenvalue,  $\lambda_1$ , is shown by Equation 2.9 and originates from Equation 2.8

$$\lambda_1 = E_T(\phi, t) = \int_{-\infty}^{\infty} \tilde{u}_T(t)^2 dt \quad (\text{Eq. 2.9})$$

which computes the energy value for a certain set of splitting parameters. Because of this, a corrected seismogram should only have one nonzero eigenvalue. Nevertheless, noise within the seismogram will cause the components to never perfectly match. It becomes nearly impossible to find one nonzero eigenvalue, so a search for the most singular matrix is performed instead to find the most ideal splitting parameters (Figure 2.12). The method used for teleseismic events in this study finds a minimum value for  $\lambda_2$  (Silver and Chan, 1991). The Bowman and Ando (1987) approach is very similar to this, but a rotation test finds the fast polarization direction parameter, and a maximum cross-correlation finds the lag time parameter.

Energy values are generated using Eq. 2.8 for every set of splitting parameters tested. These values are then contoured in an energy plot, where the ideal splitting parameters are marked (Figure 2.13). Since these splitting

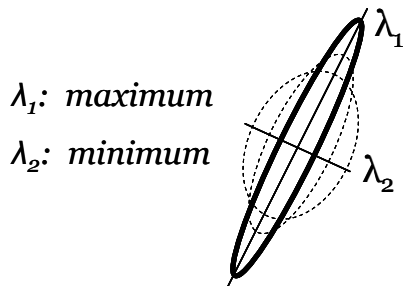


**Figure 2.12.** Eigenvalue singularity. To measure the linearity of particle motion, we solve the eigenvalues of the covariance matrix. A waveform containing no splitting will have only one nonzero eigenvalue. To correct splitting, we search for splitting parameters that produce a minimum eigenvalue.

parameters should have an associated minimum value, the optimal solution should lie within a convex structure, or “bowl”-shape within error space. A more constrained “bowl”-shape shows less error associated with the parameters. The quality-control process is finalized by checking these errors to find if the splitting parameters fall within a 95% confidence interval described in Silver and Chan (1991). For an  $n$ -point discrete time series,  $\lambda_2^{\min}$  is essentially the sum-of-

squares of noise on the corrected tangential component under a  $X^2$ -distribution. The confidence region is found with an F-test for  $\nu$  degrees of freedom and  $k$  parameters at an  $\alpha$  confidence level for values of  $\lambda_2$  that satisfy the equation

$$\frac{\lambda_2}{\lambda_2^{\min}} \leq 1 + \frac{k}{\nu - k} f_{k, \nu - k}(1 - \alpha) \quad (\text{Eq. 2.10})$$

where the inverse of the F-distribution is represented by  $f$ ,  $k = 2$  for the splitting parameters, and  $\alpha$  corresponds with the 95% confidence interval as 0.05. The quantity of  $\nu$  is usually much smaller than  $n$  samples for a discrete series. However, this quantity depends on instrument response and the noise spectrum, so  $\nu$  is relatively unknown. Silver and Chan (1991) estimate  $\nu$  from each minimum by finding  $\nu_i = v_i / n_i$  for every  $i$ th record and then averaging to find  $\nu$ .

Parameters that fall within the 95% confidence interval are assumed to be a possible set of shear wave splitting parameters. If the splitting parameters are not constrained by a minimum “bowl”-shape, the measurement may be

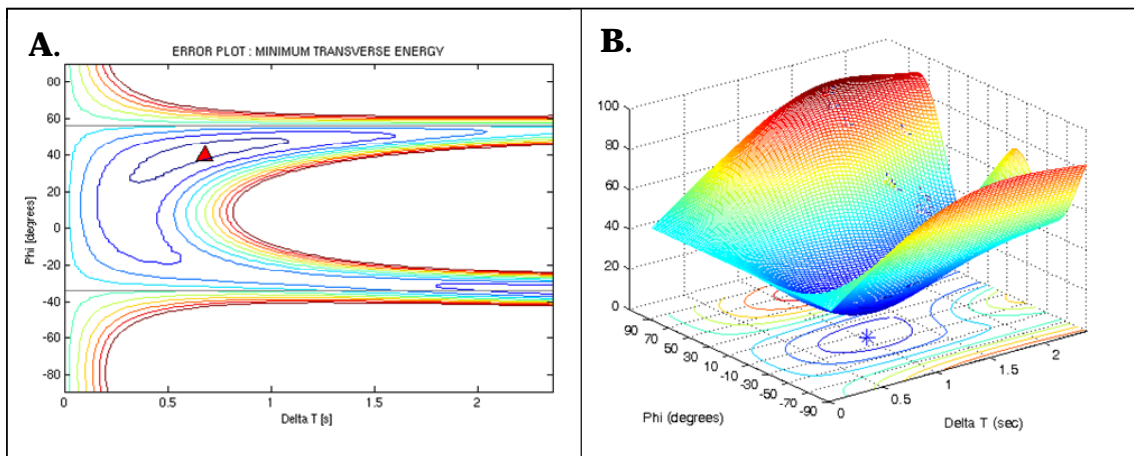
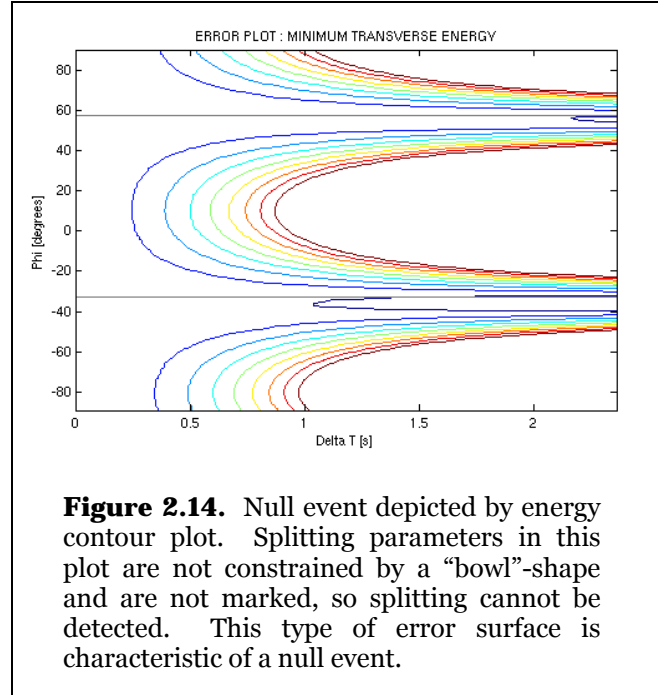


**Figure 2.13.** Energy contour plot. A. Plotted contours show the margin of error associated with the optimal splitting parameters designated by a triangle. B. The optimal splitting parameters have a minimum energy value that lies in a convex “bowl”-shape. This value also represents the minimum eigenvalue when solving the covariance matrix.

considered a null. Supposed null events occur when splitting cannot be detected. Null events also have a characteristic shape to the error surface (Figure 2.14). They occur when seismic waves propagate through an isotropic medium, or the fast polarization direction is equal to initial polarization



(Wüstefeld and Bokermann, 2007). Null events should not be disregarded. If a null event is associated with only specific back azimuths, information is presented on the strength and geometry of the anisotropy. However, if nulls are visible from all back azimuths, the media can be considered isotropic.

Theoretically, we can measure shear-wave splitting from any type of S-wave. To avoid problems though, only S-phases where the angle of incidence falls within the shear-wave window should be used. The shear-wave window is defined by the critical surface conversion angle  $i_c$

$$i_c = \arcsin \frac{v_s}{v_p} \quad (\text{Eq. 2.11})$$

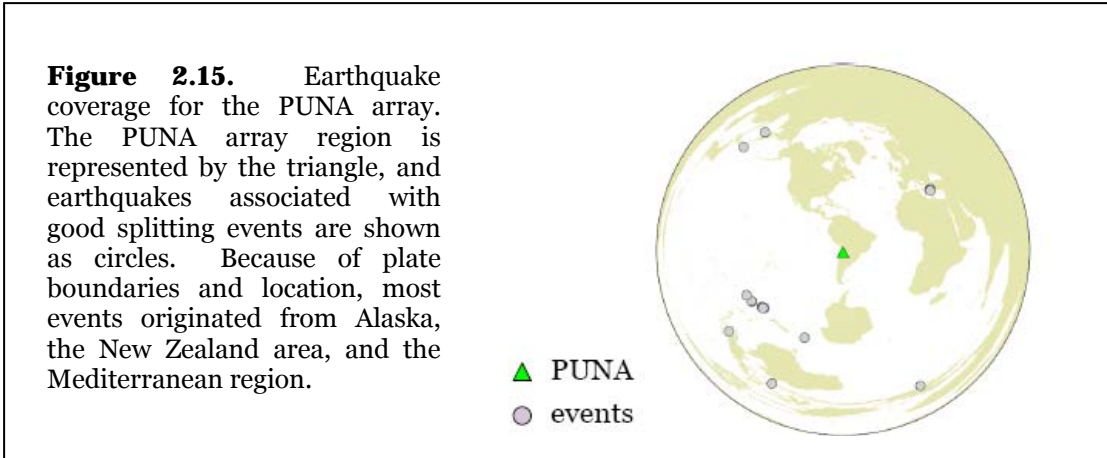
where  $v_s$  and  $v_p$  are S-wave and P-wave velocities near the surface, respectively. The critical angle is approximately  $35^\circ$  from the vertical for shear-waves (Savage, 1999). If the angle of incidence of an incoming S-wave is greater than this, the

recorded wave amplitude and phase become distorted. Because of this, most phases used for measuring shear-wave splitting have near-vertical incidence.

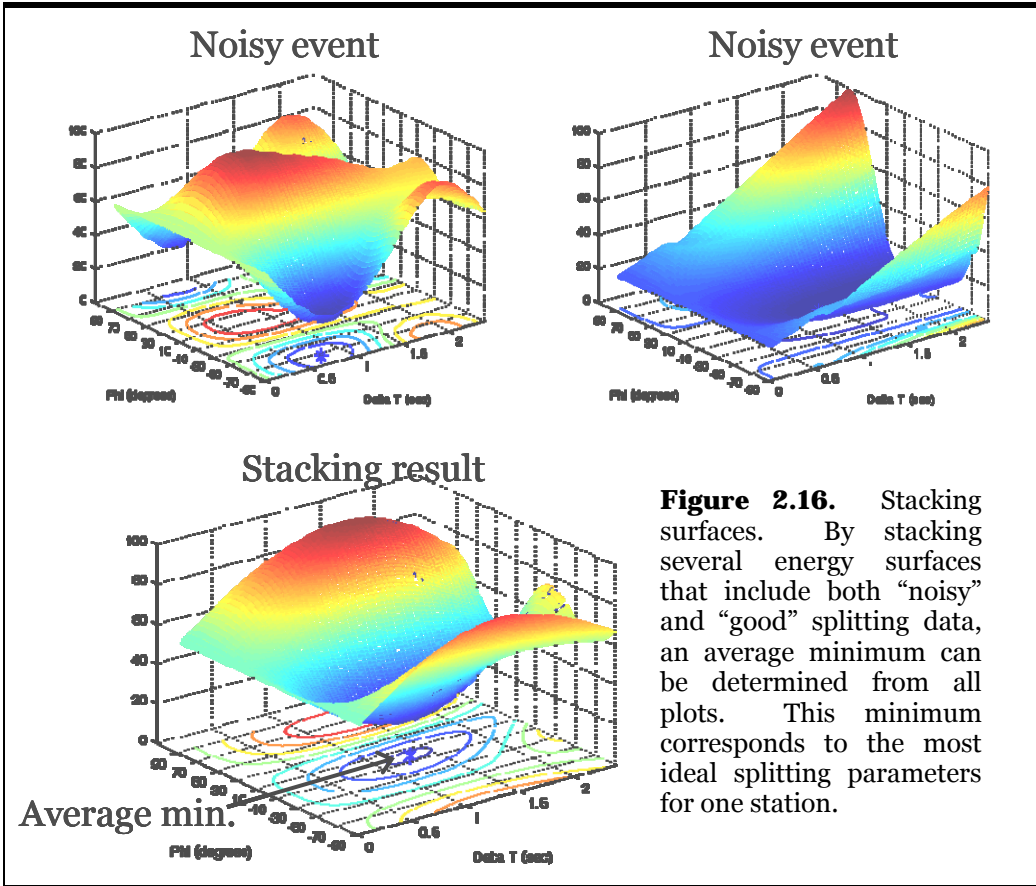
### **Stacking**

Local and teleseismic earthquake coverage for the PUNA seismic array was unevenly distributed. As mentioned earlier, optimal SKS phase recordings required a search of distances from  $85^{\circ}$  to  $180^{\circ}$  from the center of the array. Because of South America's location in relation to plate boundaries where most large earthquakes occur, large azimuthal gaps exist in PUNA array coverage that can bias anisotropy measurements. Most good splitting events originated from the regions of New Zealand, Alaska, and the Mediterranean (Figure 2.15). This limited azimuthal coverage could lead to missed complexities in shear-wave splitting behavior beneath the array. Also, because of the specific distances and depths of events used in this study, phase quality of S-waves is illustrated as mostly poor to nonexistent. For these reasons, events that demonstrate good shear-wave splitting measurements are fewer than desired. Other shear-wave splitting studies have had similar problems, but the main cause for degraded waveform quality has been oceanic wave-related seismic noise, causing large individual splitting errors (Bjarnason et al., 2002; Wolfe and Silver, 1998).

Since the reliability of this research is dependent on good data, we wished to increase our data set. This was achieved by using not only "good" split data but also the "noisy" data. A combination could provide more ideal splitting parameters (Figure 2.16). Originally, Wolfe and Silver (1998) modified the



method of Silver and Chan (1991) to estimate a single set of splitting parameters by stacking error space of multiple events. Several studies have used this type of stacking method (Restivo and Helffrich, 1999; Vinnik et al., 1989; Wolfe and Vernon III, 1998; and Wolfe et al., 1999). For instance, Bjarnason et al. (2002)



used this procedure to stack misfit error surfaces where the 95% confidence region was not well constrained to obtain a better constrained solution. We have also used a stacking method to average individual error surfaces and find an average minimum to correspond with optimal splitting parameters.

In theory, the best splitting parameters are found from a combination of ‘good’ split data and ‘noisy’ data, or an overall average for each station. Before averaging though, the data must be normalized with a base level. Then, a weighted average of the data will be based on the normalization to provide the best results. The setup for this method is a simple inverse problem with a weighted least squares solution for the estimated model parameters.

$$\mathbf{m}^{\text{est}} = (\mathbf{G}^T \mathbf{W}_e \mathbf{G})^{-1} \mathbf{G}^T \mathbf{W}_e \mathbf{d} \quad (\text{Eq. 2.12})$$

where the weight matrix ( $\mathbf{W}_e$ ) is defined as

$$\mathbf{W}_e = \begin{pmatrix} \frac{1}{\sigma_1^2} & 0 & \dots & \dots & 0 \\ 0 & \frac{1}{\sigma_2^2} & \ddots & & \vdots \\ \vdots & \ddots & \frac{1}{\sigma_3^2} & \ddots & \vdots \\ \vdots & & \ddots & \ddots & 0 \\ 0 & \dots & \dots & 0 & \frac{1}{\sigma_N^2} \end{pmatrix}, \quad (\text{Eq. 2.13})$$

and  $1/\sigma_i^2$  is the variance for each energy contour plot for one station based on an assigned weight. The variance can be found using the equation

$$\sigma_i^2 = \sum_i^N 1 - \left( \frac{(x_i - x^*)^2}{\sum (x_i - x^*)^2} \right) \quad (\text{Eq. 2.14})$$

where  $x_i$  defines the sample event and  $x^*$  defines the assigned weighted event for  $N$  total events at one station. Considering data from each event as one matrix, the program Matlab was used to compute and plot the weighted average for each station. The code is shown in Appendix A. Four separate assigned weighted events were based on the following factors:

- 1) lag time with least error,
- 2) fast polarization direction with least error,
- 3) the average minimum energy value, and
- 4) the absolute minimum energy value.

Applying weights to these separate events eliminates the extreme effects of outliers. The weighted average, or stacking, of  $N$  events for one station can then be found by

$$E(j) = \sum_j^n \frac{\sigma_{tot}^2 x_i(j)}{\sigma_{tot}^2} \quad (\text{Eq. 2.15})$$

for  $n$  total matrix elements, each given value  $j$ .

As an example, assume we have four events producing energy contour plots for a specific station illustrated in Figure 2.17. For one specific  $j$  value,  $i_1=8$ ,  $i_2=2$ ,  $i_3=9$ , and  $i_4=2$ . If the assigned weight is the event corresponding with  $i_1$ , using Equation 2.14,  $\sigma_1^2 = 1$ ,  $\sigma_2^2 = 0.51$ ,  $\sigma_3^2 = 0.99$ , and  $\sigma_4^2 = 0.51$  making  $\sigma_{tot}^2 = 3.01$ . Using Equation 2.15,  $E(j) = 6.3$ . This would represent the stacked energy value for this one matrix element for all four events at this station. This value will plot

onto a new energy contour and may or may not be the minimum value which shows the most ideal model parameters for shear-wave splitting.

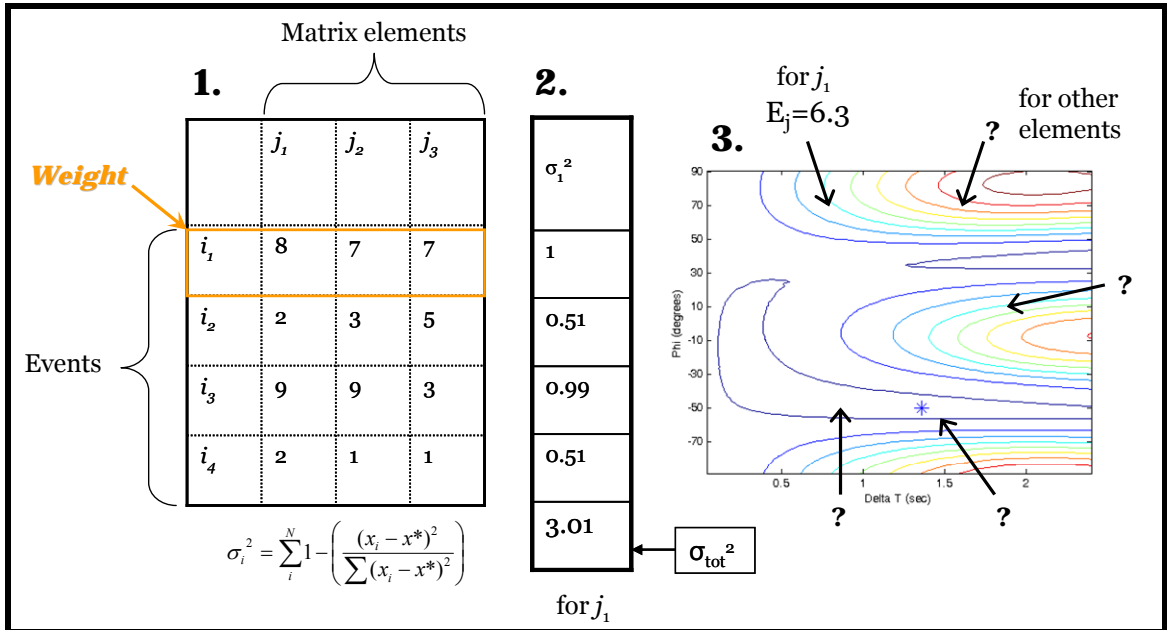


**Figure 2.15.** Energy stacking example. This table represents one example station and its results where each  $i$  represents a specific event recorded at this station and each  $j$  represents one element of the matrix that is used in the original energy plot (1). Using a designated weighting event based on the energy plot from that event, each component can be normalized based on variance from the weight (2). A weighted average, or “stack,” is then made for each element which is then plotted on a contour map to display the averaged minimum energy (3).

# **CHAPTER 3: Results and Implications for Mantle Deformation**

## **RESULTS**

To determine mantle deformation beneath the southern Puna plateau, we have investigated shear-wave splitting using a 43 station seismic array deployed in the southern Puna plateau for ~16 months. More than 330 teleseismic and 220 local events were extracted from the data of the stations for shear-wave splitting consideration. Of these, 17 teleseismic and 51 local events (Appendix B) produced 30 total teleseismic and 88 total local splitting results (Appendix C).

Each split event passed quality-control inspection described in Chapter 2 (Appendix D). When initially analyzing the events, maximum error values were chosen based on those used for past shear-wave splitting research (e.g. Sandvol et al., 2003). For teleseismic events, a maximum of 35° error was allowed for the fast polarization direction and a maximum of 0.6 seconds for lag time error before the event was interpreted as a null. One degree of freedom per second and a signal-to-noise ratio of 5.0 were allowed. For local events, 20° maximum fast polarization direction error and 0.7 seconds maximum lag time error were allowed. 0.5 to 3.0 degrees of freedom per second were allowed as well as a signal-to-noise ratio of 2.0.

Teleseismic and local S-wave lag times are noticeably different for split waveforms. Local events typically have an average lag time of less than 0.4 seconds while a split teleseismic event has an average lag time of 1.0 second. Figures 3.1 and 3.2 illustrate examples of a split local event and split teleseismic event, respectively. The difference in splitting can be attributed to portions of the teleseismic event path below the hypocentral depth of the local earthquake. This suggests that a large portion of teleseismic splitting is either within the subducting Nazca lithosphere or in the asthenosphere below the slab.

From the teleseismic events splitting results, we found an average of about 1.0 second time delay between the fast and slow components. The maximum lag time observed is  $1.8 \pm 0.6$  seconds for station BB11. Two separate events showed a minimum lag time of  $0.6 \pm 0.3$  seconds at station EW10 and  $0.6 \pm 0.4$  seconds at station BB12. The weighted average splitting parameters for each station were plotted on a topographic map of the study area (Figure 3.3). From this plot, we observed a very complex splitting pattern throughout the PUNA array, where measures of polarization are variable within smaller regions.

Splitting results for local events show an average lag time between 0.4 and 0.5 seconds. Station NS11 showed a maximum splitting delay time of  $1.5 \pm 0.1$  seconds, and several stations illustrated a minimum time delay of 0.1 seconds. The splitting parameters for individual events were again plotted on a topographic map (Figure 3.4).

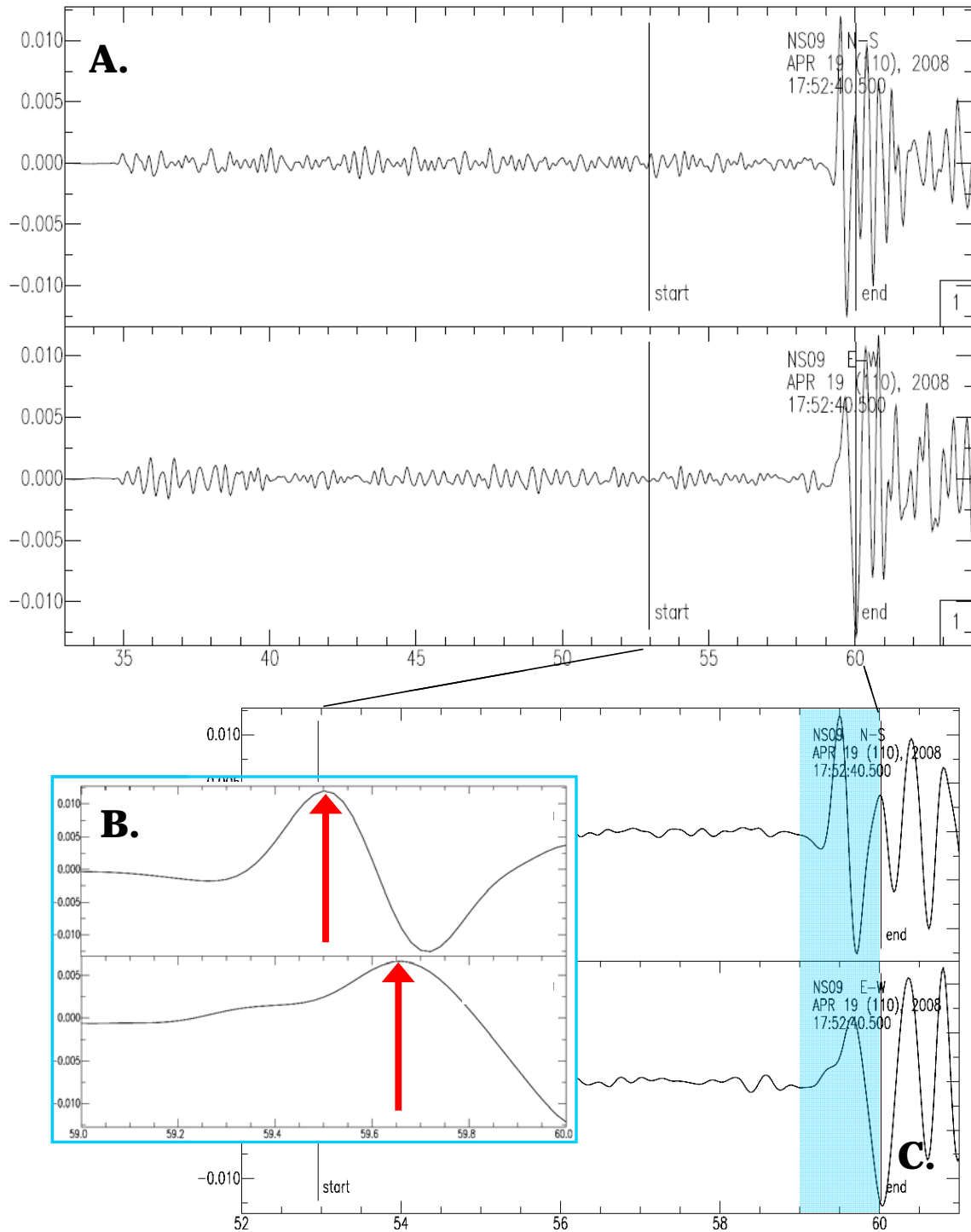


**Figure 3.1.** Seismogram of local event crustal splitting. A. Full seismogram recorded at NS09 for local event 2008, Julian day 110. Notice the P-wave arrival time of ~35 sec. and the S-wave arrival time of ~59 sec. B. Magnified portion of the S-phase splitting shown by the shaded region of C. The arrows represent peaks that show 0.2 sec. lag time which indicates crustal splitting. C. Seismogram showing the windowed portion of the event.

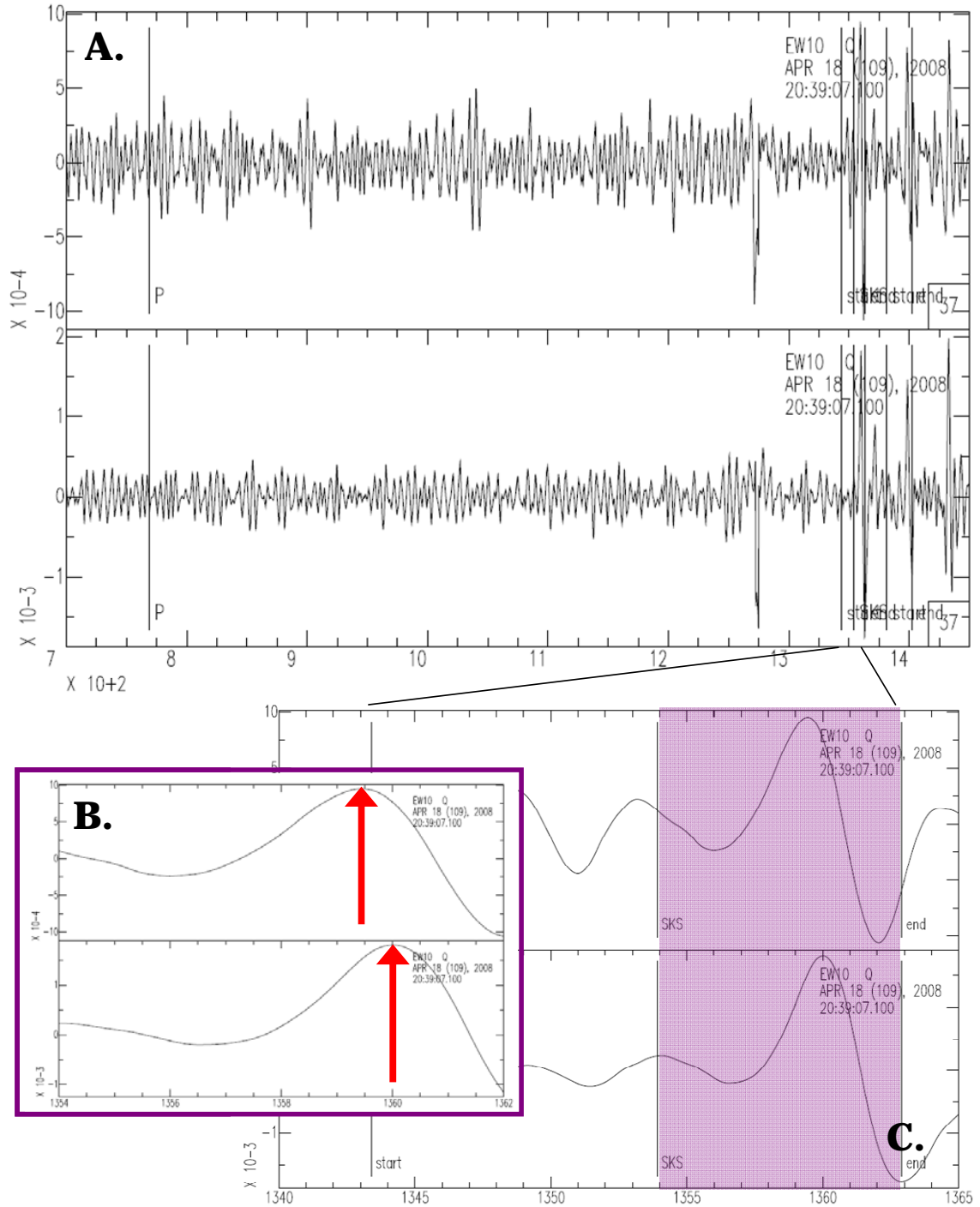


**Figure 3.2.** Seismogram of teleseismic splitting. A. Full seismogram recorded at EW10 for teleseismic event 2008, Julian day 109. Notice the P-wave arrival time of ~770 sec. and the SKS arrival time of ~1350 sec. B. Magnified portion of SKS splitting shown by the shaded area of C. The arrows represent peaks that show 0.6 sec. lag time which indicates splitting within the upper mantle. C. Seismogram showing the windowed portion of the SKS phase.

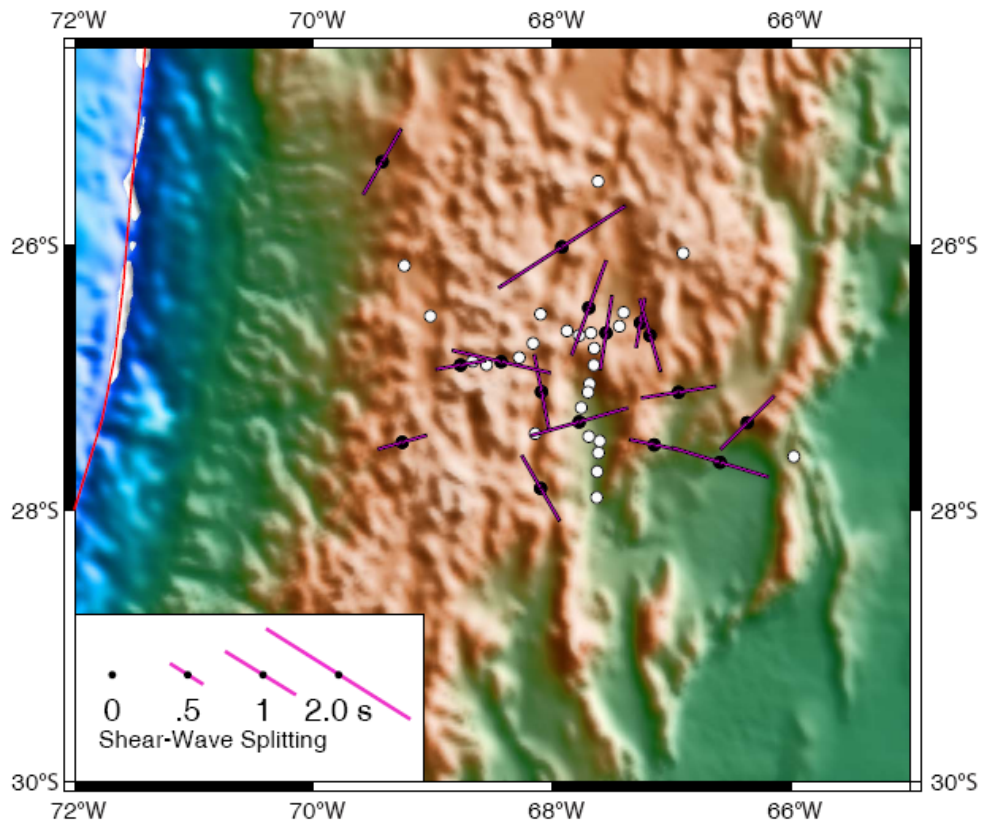


**Figure 3.3.** Topographic map of teleseismic events splitting results. Segment length indicates splitting magnitude as noted by the scale, and segment azimuth indicates fast polarization direction. White circles show stations where no teleseismic splitting was recorded, or null events. Plotted results consist of weighted averages for each station.

## SPLITTING PARAMETERS

Once the splitting parameters have been given a general surface representation, anisotropy can be localized. Because vertical resolution is sacrificed for excellent lateral resolution in shear-wave splitting, the most important constriction of anisotropy is depth. Using both local S-waves and teleseismic S-phases, the depth of the anisotropic zones can be constrained

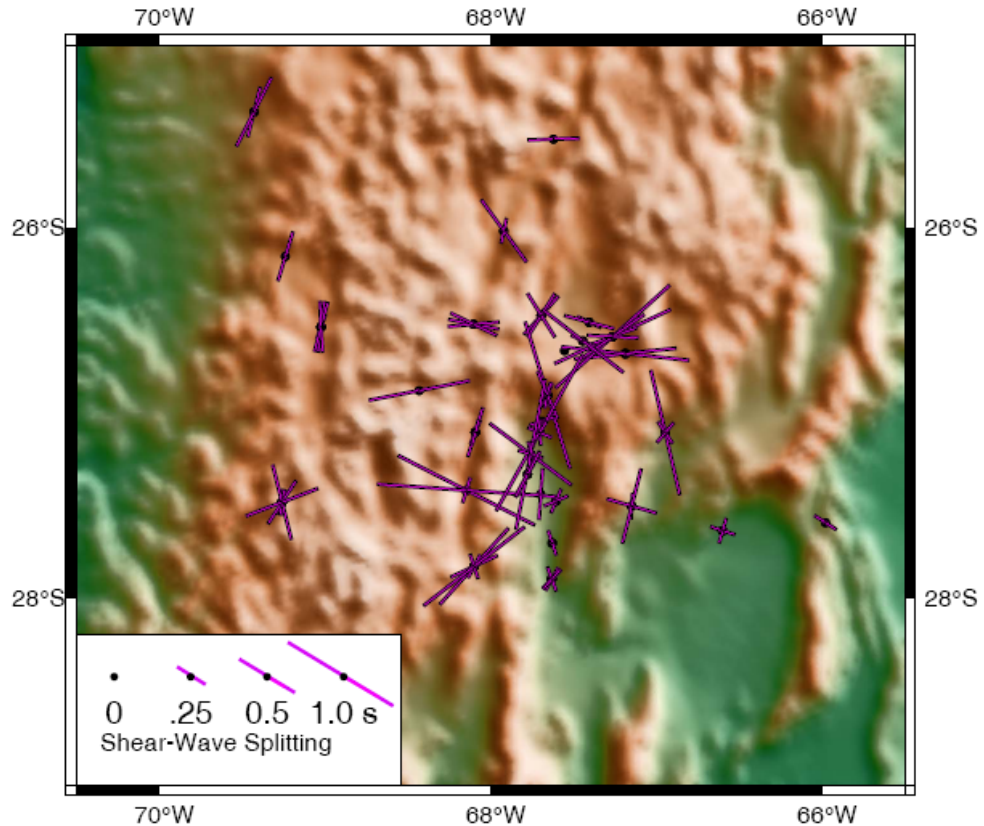


**Figure 3.4.** Topographic map of local events splitting results. Segment length indicates splitting magnitude as noted by the scale, and segment azimuth indicates fast polarization direction. Results for each individual splitting event are plotted for each station.

(Figure 3.5). For instance, if a local slab event exhibits splitting with a delay time of 0.2 seconds, and a teleseismic S-phase shows a splitting delay time of 0.9 seconds, most splitting has occurred within or beneath the subducting slab as local S-waves travel upward and isolate the above-slab component (Russo and Silver, 1994). To better constrain depth and localize anisotropy, the stations of the PUNA array have been divided into four separate regions shown in Figure 3.6: Volcanic arc, Puna plateau, Southern transition, and Eastern. Shear-wave splitting data has been plotted on graphs separately for each region.

## Constraining depth

Crustal anisotropy is caused by the alignment of cracks and microcracks within the upper 10-15 km of the crust and is perceptible within our shear-wave splitting results. Normal crustal splitting reveals delay times of 0.04-0.2 seconds, and delay times can reach 0.5 seconds if the station is located above a fault (Savage, 1999). Crustal splitting delay times of areas such as the Tibetan plateau are 0.1-0.3 seconds (Silver and Chan, 1988; Vinnik et al., 1992). According to McNamara et al. (1994), these times are equivalent to crustal delay times of the

Andes. Mantle splitting yields greater delay times, and crustal anisotropy is considered insignificant for teleseismic waves. Vertically propagating waves are hardly affected by horizontal foliation planes of the crust. Even though crustal splitting is likely present, shear-wave splitting measured with teleseismic waves is mostly a consequence of the upper mantle.

Local earthquakes originate in the subduction zone along the slab and travel above. Therefore, these events allow us to constrain anisotropy to the mantle wedge (Figure 3.5). The epicenters of split local events have been plotted on a map of South America shown in Figure 3.7. Splitting parameters have been

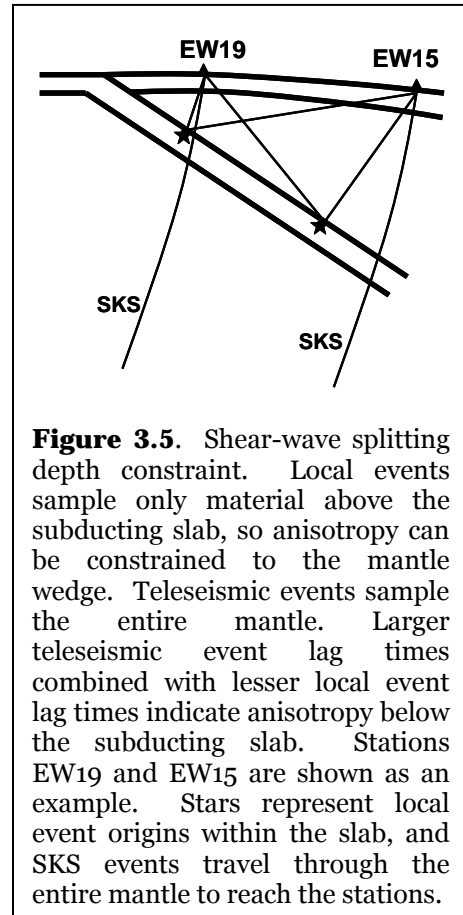


**Figure 3.5.** Shear-wave splitting depth constraint. Local events sample only material above the subducting slab, so anisotropy can be constrained to the mantle wedge. Teleseismic events sample the entire mantle. Larger teleseismic event lag times combined with lesser local event lag times indicate anisotropy below the subducting slab. Stations EW19 and EW15 are shown as an example. Stars represent local event origins within the slab, and SKS events travel through the entire mantle to reach the stations.

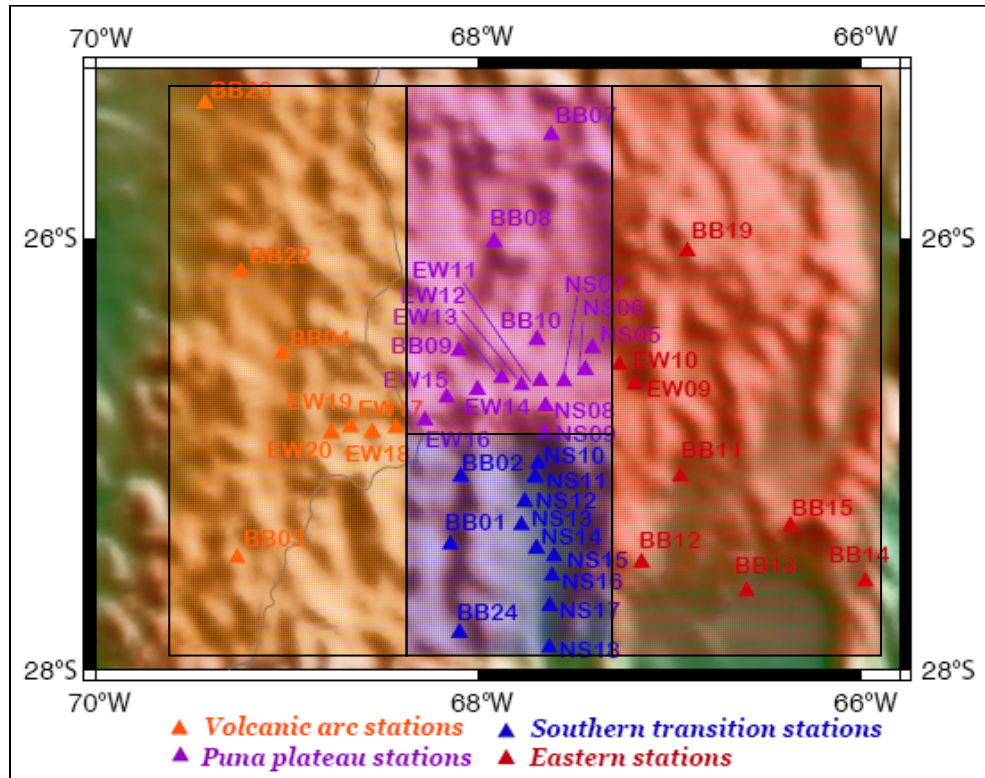


**Figure 3.6.** Regional station map. The PUNA seismic array is divided into four sections shown by the noted colors. The western section has been designated Volcanic arc, the central-north section as the Puna plateau, the central-south as the Southern transition, and the eastern portion as the Eastern stations. Each section is interpreted separately for more accurate results.

plotted against the source depth for local events (Figure 3.8). Teleseismic splitting events are plotted in red as well for comparison at a fixed depth of ~620 kilometers to correspond with the deepest local events.

#### Volcanic arc:

Within the Volcanic arc region, many local events have a lag time of less than 0.3 seconds and are thus mostly considered products of crustal splitting. With the exception of one splitting event, teleseismic splitting lag times are only slightly greater than local events splitting within the Volcanic arc. Hence, we assume that most anisotropy occurs in the mantle wedge with some subslab anisotropy. One local event shows consistency with teleseismic events in that it

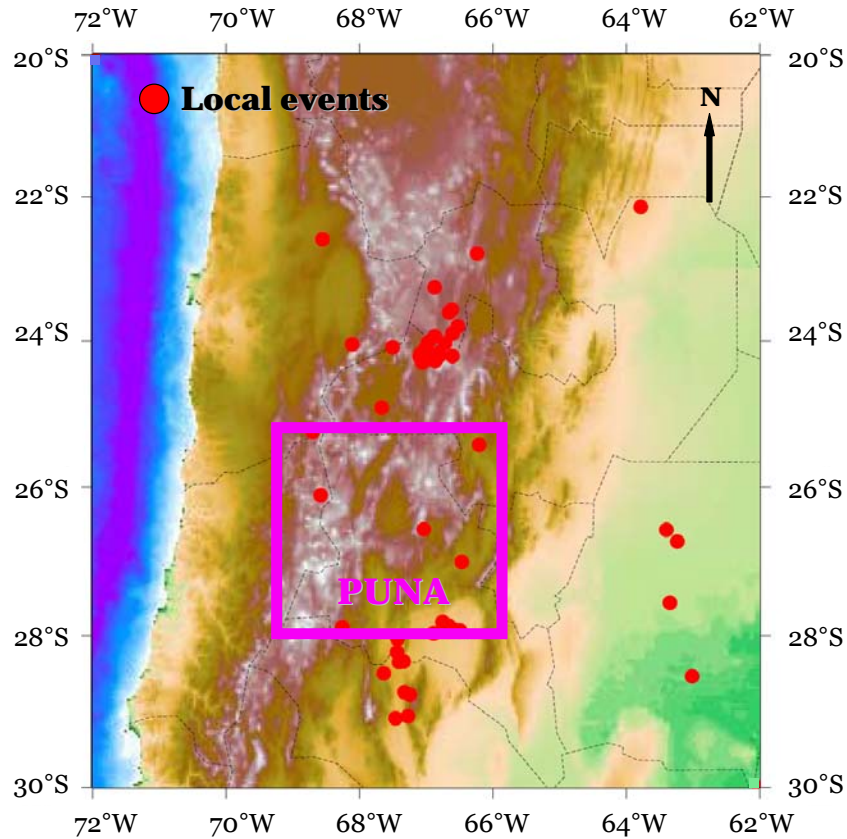


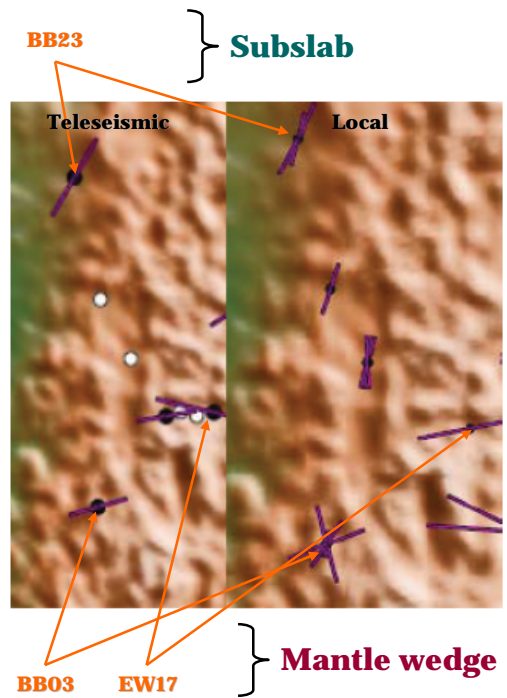
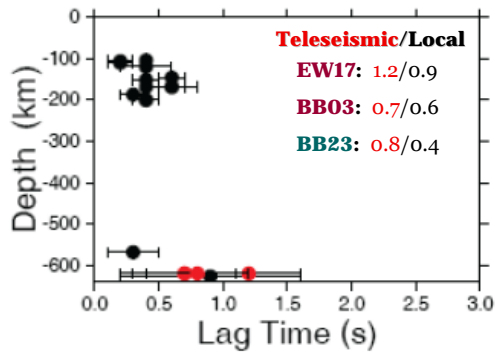
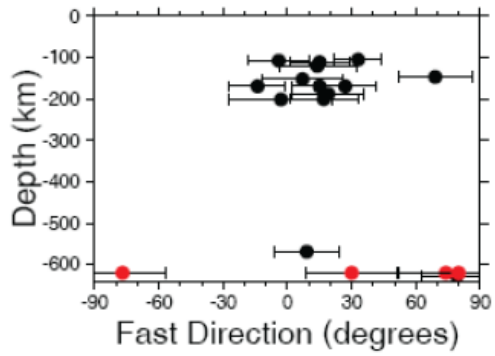
**Figure 3.7.** Local events map. Epicentral locations of local events found to produce good splitting results have been plotted in red. The PUNA array region is outlined in purple.

has nearly 1.0 second of delay time, and the source depth lies below 600 kilometers. This event further suggests a majority of the detected anisotropy is in the mantle wedge.

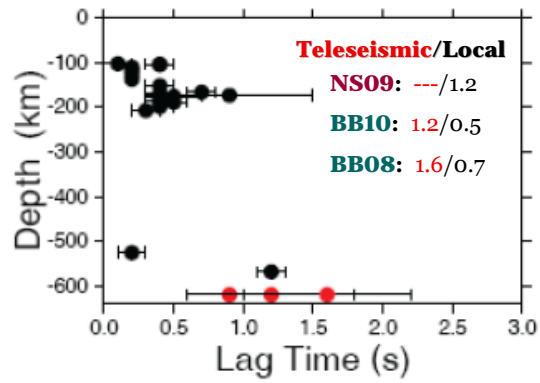
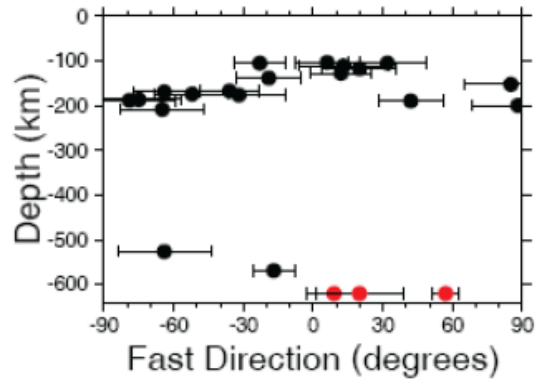
Teleseismic fast polarization directions are oriented E-W with the exception of one station orientation of SW-NE, a trench-parallel direction. Local events splitting with hypocentral depths less than 250 kilometers cluster around 0-30° fast direction, also a trench-parallel direction. A local event for station BBo3 shows a depth of almost 600 kilometers, and the fast direction is trench parallel. The lag time for this event is also only 0.3 seconds, indicating that

**A.**

# Volcanic arc

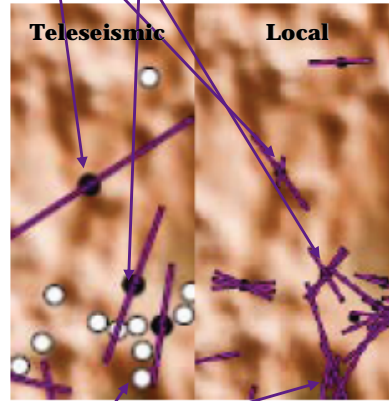


## B. Puna plateau



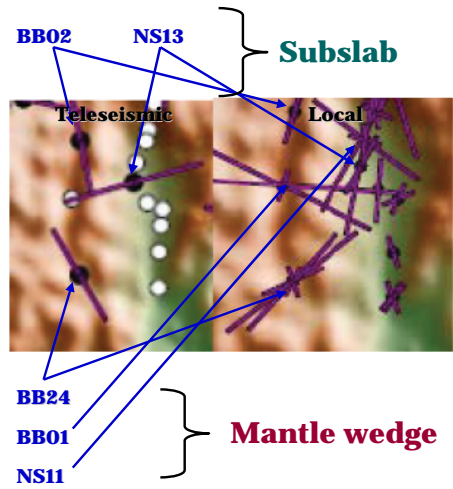
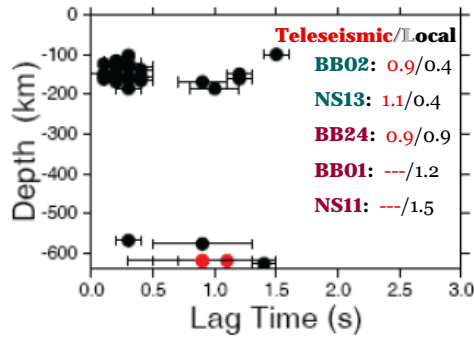
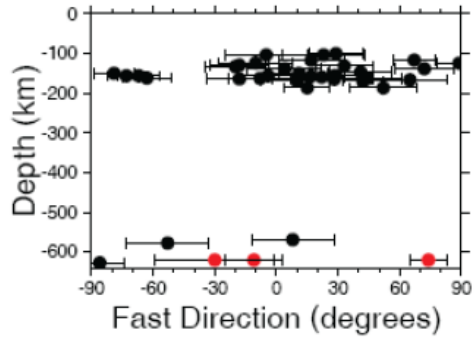
BB08 } **Subslab**

BB10 }



NS09 } **Mantle wedge**

# C. Southern transition



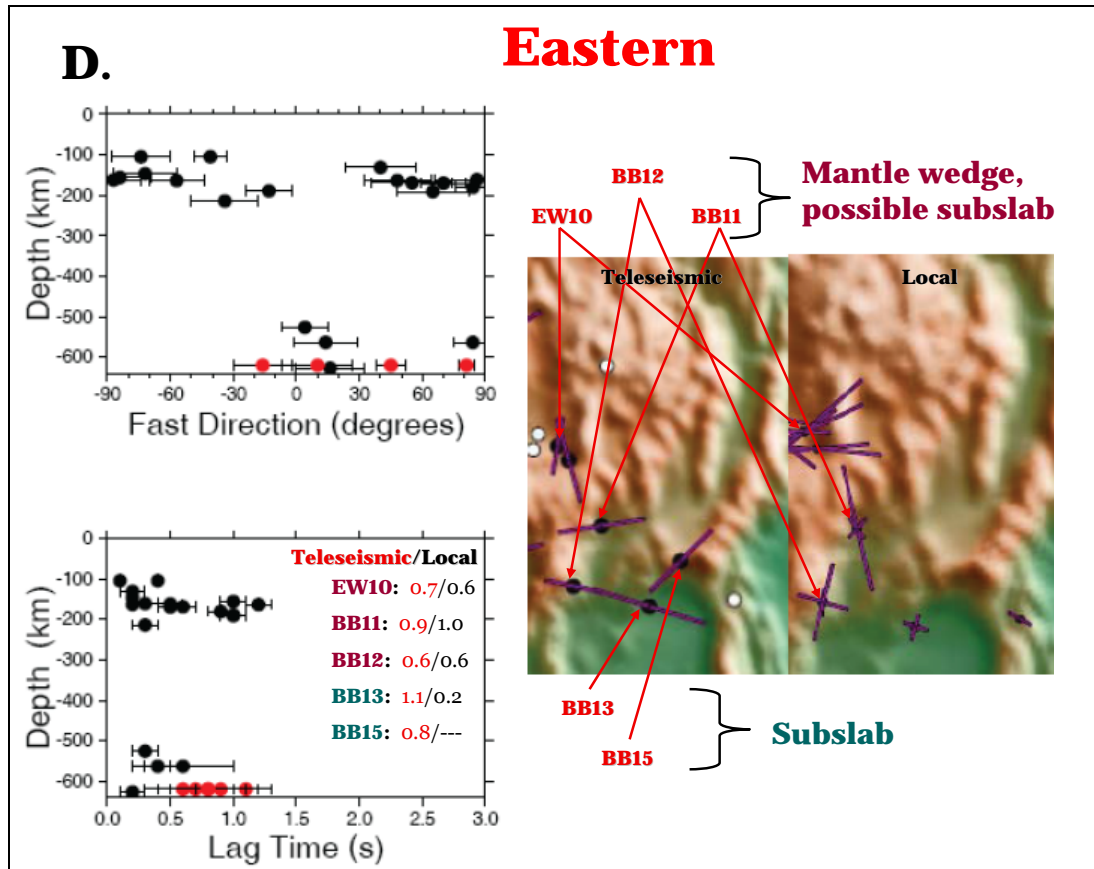


**Figure 3.8.** Splitting versus depth. Comparing teleseismic splitting events to local splitting events of known hypocenters aids in constraining the depth of anisotropy. Local events (black) with lag times equivalent to teleseismic events (red) demonstrate anisotropy occurrence within the mantle wedge. Local events with lag times much smaller than teleseismic events demonstrate anisotropy within the subslab. Stations are color-coded according to anisotropy occurrence within the subslab/mantle wedge, and example station delay times are shown in red for teleseismic events and black for local events. Sectional maps show both teleseismic and local events splitting results, and stations are analyzed in regions. A. Volcanic arc. B. Puna plateau. C. Southern transition. D. Eastern. Both subslab and mantle wedge splitting patterns were found for each region.

splitting below this station only occurs in the upper 250 kilometers of the upper mantle.

#### Puna plateau:

Within the Puna plateau region, teleseismic event delay times average 1.0-1.5 seconds. Local splitting events are again mostly confined to the upper 250 kilometers. Splitting with lag times of 0.2 seconds are considered an effect of crustal anisotropy. One event originating from almost 550 kilometers depth also shows a delay time of 0.2 seconds. This event for station NS06 illustrates that anisotropy beneath might exist only at crustal levels, or this wave was polarized parallel or orthogonal to the mantle wedge fast direction. Another deep event has a delay time comparable to teleseismic, suggesting anisotropy in regions other than the uppermost crust.

Fast polarization directions for teleseismic splitting events are oriented SW-NE. Local splitting events with shallower depth origins are oriented from E-W to NW-SE. The deepest local events also have fast directions in the NW-SE orientation and similar delay times, indicating that anisotropy occurs within the upper 250 kilometers. Because teleseismic events appear to have separate splitting parameters from the local events, we assume that anisotropy occurs within or beneath the slab as well as in the mantle wedge.

#### Southern transition:

Teleseismic events of the Southern transition region show average lag times around 1.0 second. A cluster of local events shows delay times of less than 0.5 seconds for the upper 200 kilometers, displaying crustal anisotropy. A deep

event recorded at NS12 has a delay time of 0.3 seconds, implying that only crustal anisotropy occurs beneath this station. Other deep local events have delay times equivalent to teleseismic lag times suggesting that the primary source of anisotropy is in the mantle wedge.

The fast directions for two teleseismic events in the southern transition region have a NW-SE orientation, and one event is oriented almost directly E-W. Fast directions for local split events do not dominate one particular.

Eastern:

Teleseismic splitting lag times of the Eastern region range from 0.6-1.1 seconds, while local events splitting ranges from 0.2-1.1 seconds. Crustal splitting is associated with local events showing smaller lag times and originating from shallower depths. Local events showing splitting at greater depths with lag times equivalent to shallow events marks where crustal anisotropy only occurs in the upper 250 kilometers. Local events originating at shallower depths of 150-200 kilometers and showing average lag times of 1.0 second suggest that the uppermost mantle in the Sub-Andean fold and thrust belt is highly anisotropic. We observe evidence for anisotropy in both the mantle wedge as well as below the slab beneath the easternmost plateau as observed from teleseismic events.

Fast directions of teleseismic events recorded at four stations show an E-W orientation, while two other stations show a N-S orientation. Local splitting events show orientations both E-W and N-S. A toroidal fast polarization direction is detected within the local events splitting results for stations EW09 and EW10.

## Localized splitting

Using results of local splitting events in combination with teleseismic splitting events, the depth of anisotropy for each region of the southern Puna plateau has been constrained to either subslab or mantle wedge (Figure 3.9). To check for complications, we searched for splitting dependencies, or localized splitting. Back azimuths were plotted against splitting parameters for each of the four PUNA regions to discover any changes that could be related to multiple anisotropy layers as discussed in Chapter 2. Splitting parameters for both teleseismic and local events were used making eight total plots shown in Appendix E. No patterns of multiple anisotropy layers were visible for teleseismic events. However, splitting parameters of local events plotted against back azimuth show a possible pattern of multiple anisotropy layers for the

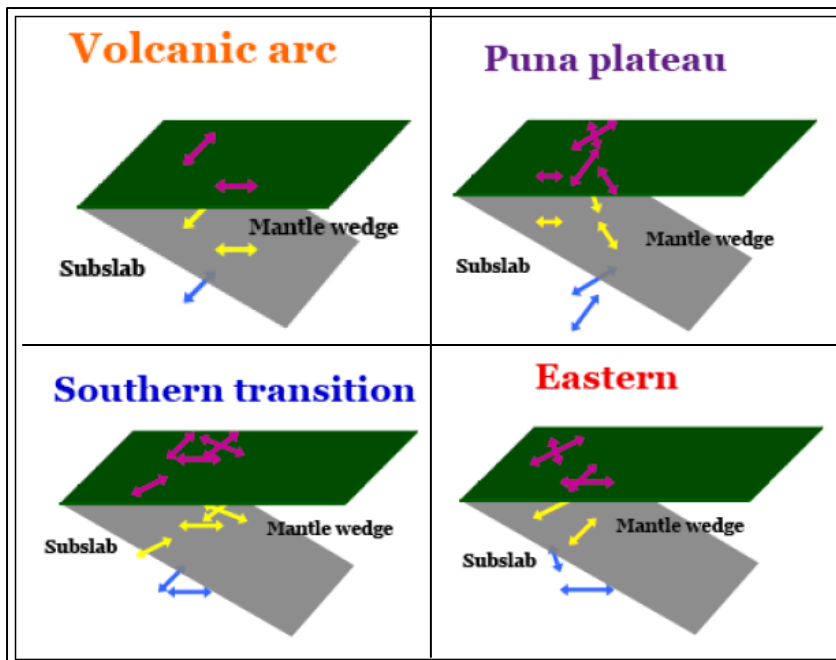


**Figure 3.9.** Regional depth constraint of anisotropy. Using the comparisons of teleseismic and local events of Figure 3.8 and the determined depth constraint of each region, models were created to show splitting results within the correct depth region. Pink arrows represent original splitting results, yellow arrows represent mantle wedge splitting, and blue arrows represent subslab splitting.

Eastern region. We plotted the splitting parameters versus the back-azimuth modulo 90 degrees (Figure 3.10). Splitting parameters exhibit  $\pi/2$  periodicity, and the plot eliminates the natural recurrence of event patterns from symmetry (Silver and Savage, 1994). The modulo plots do not appear to have characteristics of multiple anisotropy layers. However, the Southern transition and Eastern regions represent areas of numerous local splitting events.

If a variation in splitting parameters between closely spaced stations exists, the cause is likely multiple anisotropy layers. This suggests complicated localized anisotropy due to multiple flow layers within the mantle. Studies with temporary arrays, such as this one, usually do not have enough azimuthal earthquake coverage to exclude multiple anisotropy layers. However, one homogeneous layer above 250 kilometers depth can have a complex anisotropic symmetry system. To find true BAZ-dependent splitting, the Eastern and Southern transition regions must be broken down into smaller areas. Stations of these regions within close proximity to one another have been grouped together as seen in Figure 3.11. Under this division, splitting of local events found at these stations was again plotted against a modulo 90° BAZ shown in Figure 3.12. The plots show no clear patterns related to multiple anisotropy layers. Some station groups show possible azimuthal dependent splitting parameters, but the data is insufficient to constrain multiple layers. Two anisotropy layers might exist, but it is more likely that the splitting results shown by these station groups are caused by lateral changes in anisotropy, a complex homogeneous layer.

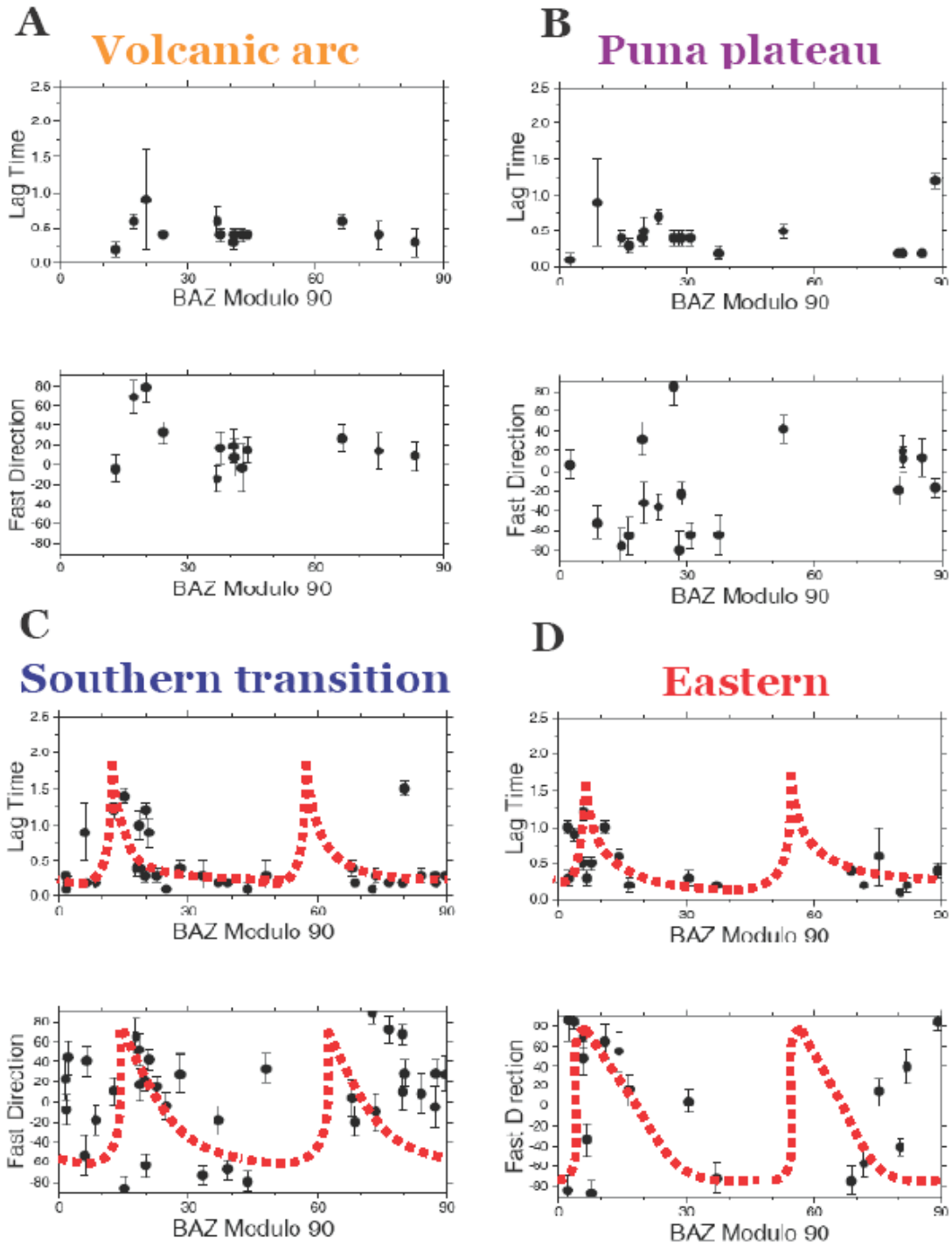


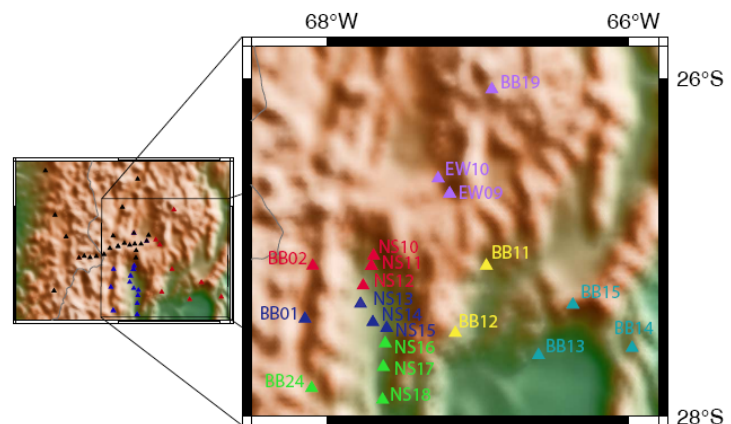
**Figure 3.10.** Splitting versus BAZ modulo  $90^\circ$  for local events. Using a scale of  $0\text{-}90^\circ$  for BAZ of local events, the natural recurrence of event patterns caused from symmetry are eliminated. If multiple anisotropy layers are present within the region of study, plots of splitting versus BAZ will illustrate repeating patterns. A. The Volcanic arc region shows no repeating patterns. B. The Puna plateau region shows no repeating patterns. C. The Southern transition region shows possible repeating patterns shown in red dashed lines. D. The Eastern region shows possible repeating patterns shown in red dashed lines.

## STACKING RESULTS

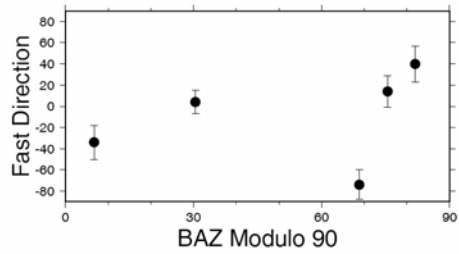
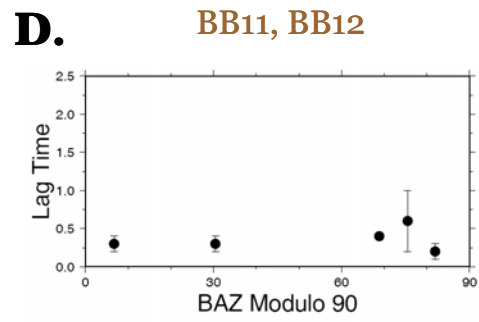
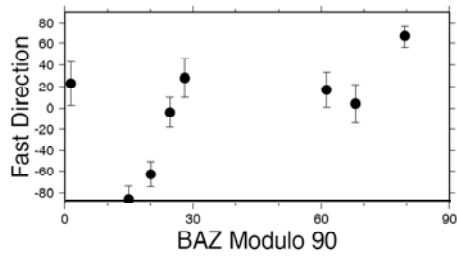
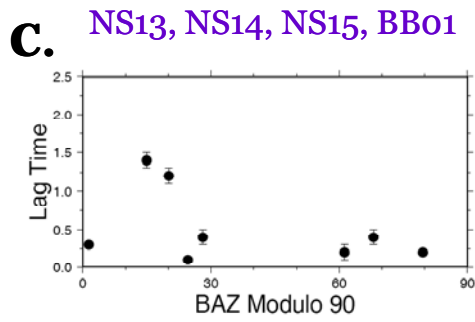
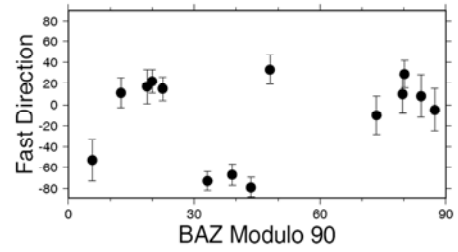
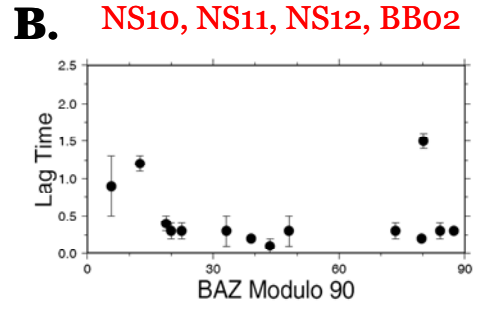
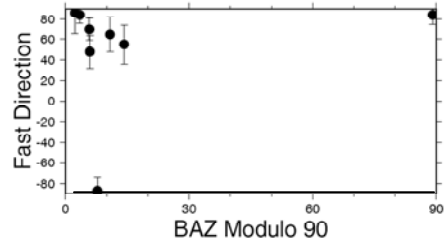
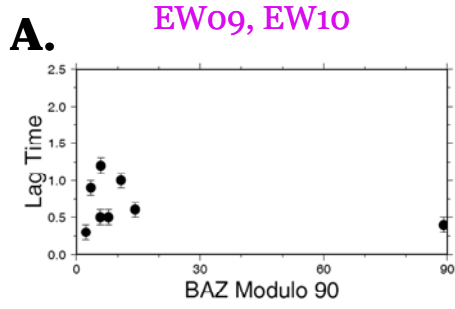
As mentioned in Chapter 2, a method of stacking energy surfaces has been applied to use ‘noisy’ splitting data in addition to ‘good’ splitting data. New energy contour plots were generated by finding a normalized weighted average of minimum energy at each station.

Several different kinds of plots were created during the stacking procedure. We used two sets of data for each station (Appendix F). One set included all events that contained ‘good’ splitting data and ‘noisy’ data. Another set included only ‘good’ splitting data. For each of these data sets at each station, four plots were created to illustrate the four different weighting factors. Results seem consistent, but an alteration of the weighting factor causes significant changes to the final topographic map. Hence, a “best” method for this particular stacking procedure is

unknown. All stacking results differ but are consistent with the original splitting results. Because of a large number of associated events, station BB13 is shown in Figure 3.13 to illustrate the differences in each



**Figure 3.11.** Magnified map of southeast stations. Stations of the Southern transition and Eastern regions were divided geographically for better modulo  $90^\circ$  plotting. Each division is represented by a different color.



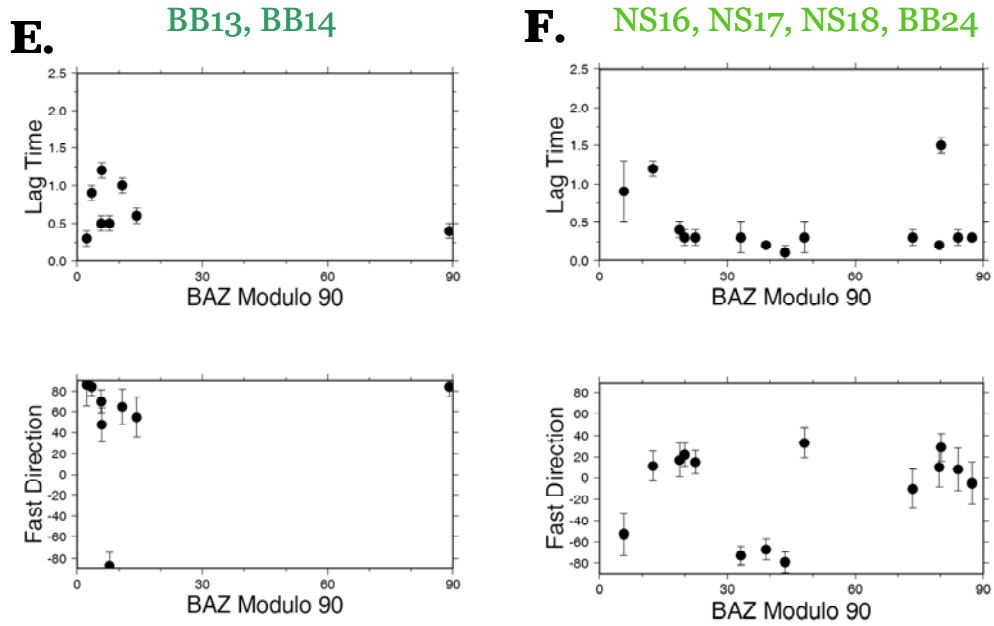


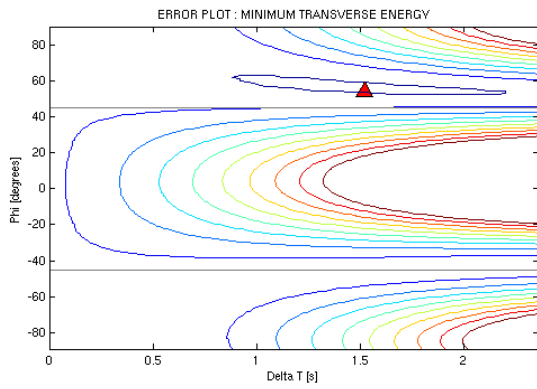
**Figure 3.12.** Splitting versus BAZ modulo  $90^\circ$  southeast stations. Plots of local event back azimuths modulo  $90^\circ$  versus both the fast direction and the lag time of shear-wave splitting for local events in the Southern transition and Eastern regions are displayed. No clear repeating patterns are observed for station divisions, implying that multiple anisotropy layers do not exist. However, more data is necessary for better examination. Plots are divided according to station locations. A. EW09 and Ew10. B. NS10, NS11, NS12, and BBo2. C. NS13, NS14, NS15, and BBo1. D. BB11 and BB12. E. Same BB13 and BB14. F. NS16, NS17, NS18, and BB24.

of these plots. The primary weighting factor was considered lag time with least error since lag time is critical for this study. Appendix G shows stacking plots for all stations using this primary weight factor for both sets of data.

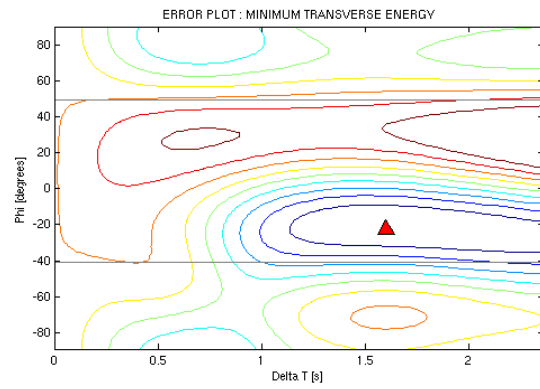
Topographic maps were created that display the magnitude of shear-wave splitting and fast polarization direction for stacking results (Appendix H). Stacking was performed for both teleseismic and local events separately. Local events, however, were categorized based on depth origin and stacked within each depth range accordingly. Three separate stacks resulted: a shallow stack with depth origin less than 200 kilometers, an intermediate stack with depth of

## A. Original energy contour plots

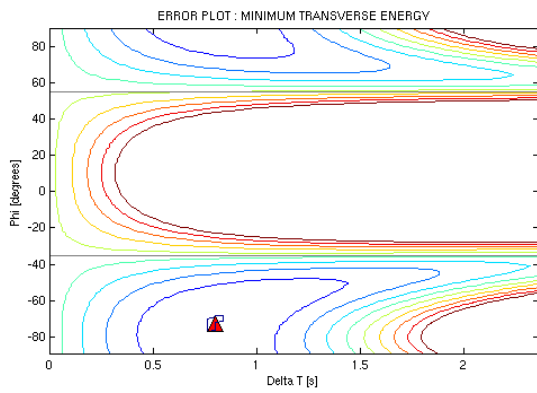
BB13-2007354



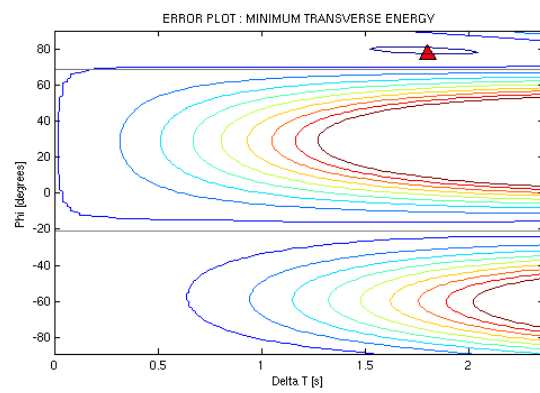
BB13-2008001



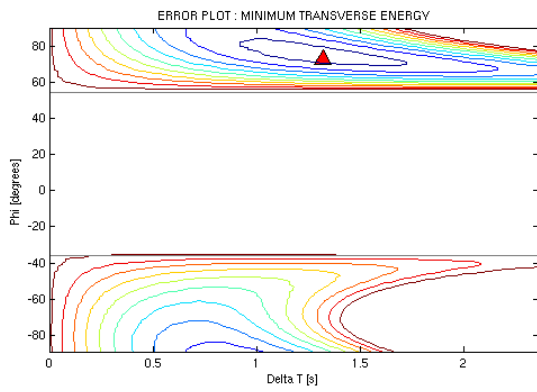
BB13-2008078



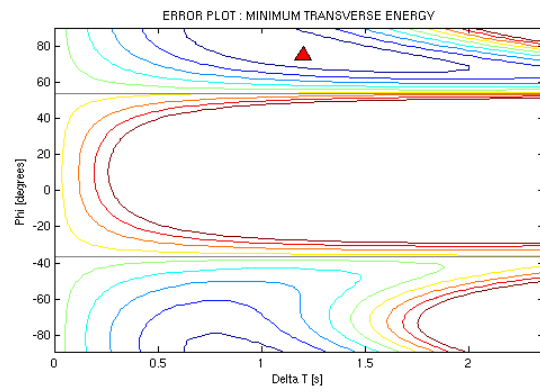
BB13-2008232



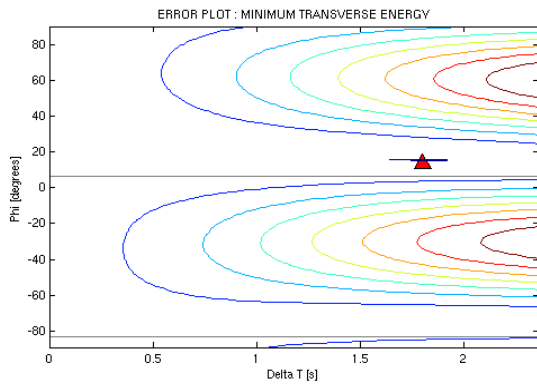
BB13-2008273



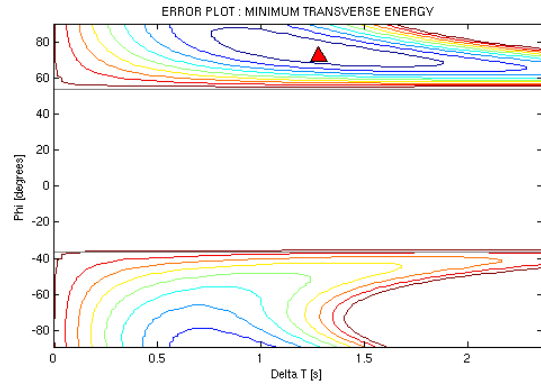
BB13-2008344



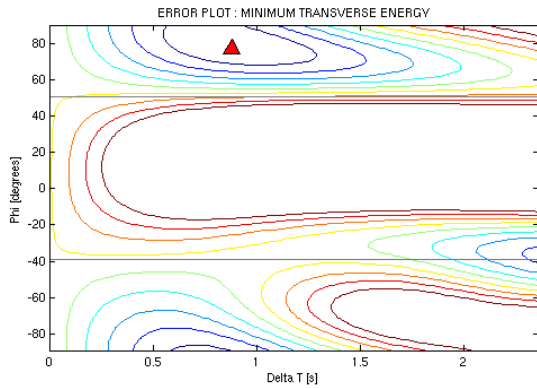
BB13-2008348



BB13-2009018



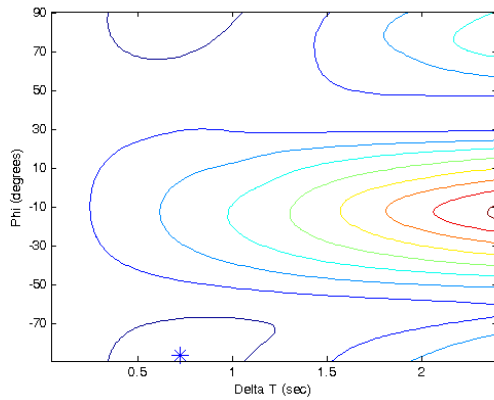
BB13-2009022



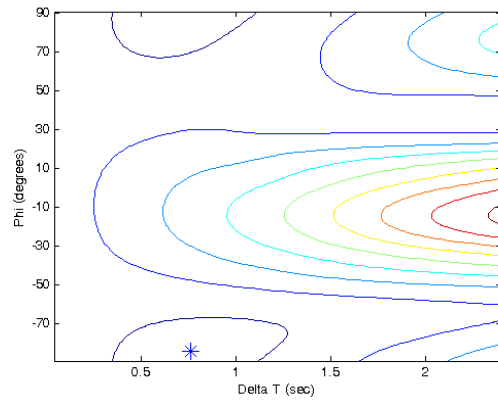
---

B. All stacking data ('good' + 'noisy')

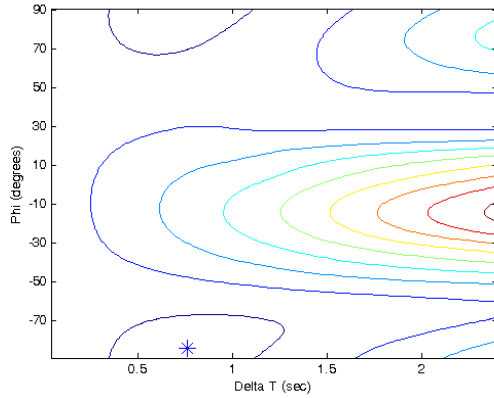
Average error (BB13)



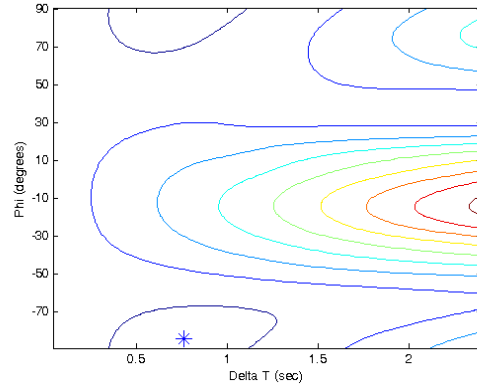
Least error in fast direction (BB13)



Least error in lag time (BB13)

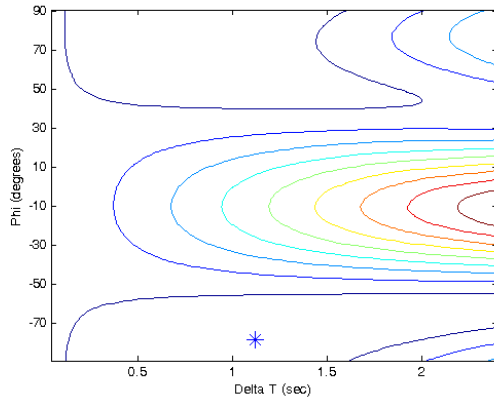


Absolute minimum (BB13)

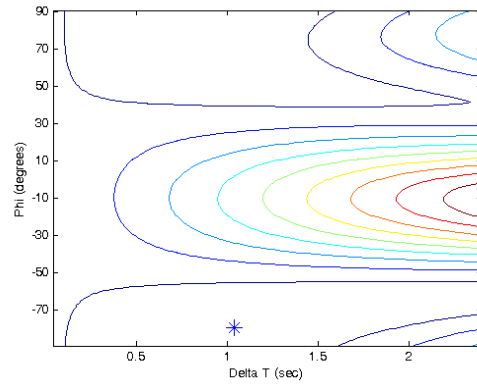


### C. Only 'good' split data

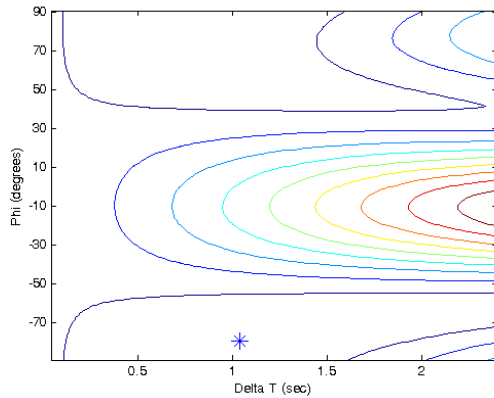
Average error (BB13)



Least error in fast direction (BB13)



Least error in lag time (BB13)



Absolute minimum (BB13)

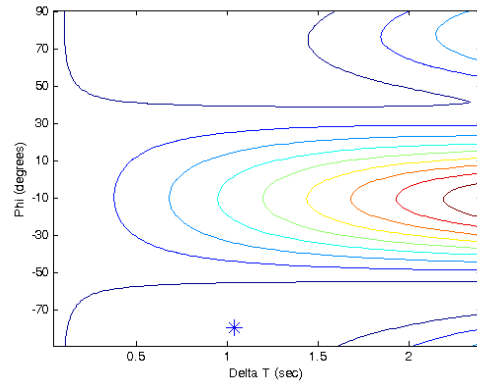


**Figure 3.13.** Teleseismic energy contour plots for station BB13. A: Original contour plots for each analyzed event at BB13. Triangles represent minimum energy. B: Contour plots from stacked events with all four weighting factors using 'noisy' and 'good' quality data. Stars represent average minimum energy. C: Contour plots from stacked events with all four weighting factors using only 'good' quality data.

200-300 kilometers, and a deep stack of depth greater than 300 kilometers. These stacks were then compared to find if flow patterns differ with depth. Energy plots created by this stacking procedure agree with original energy plots for station events with minor exceptions. Hence, this method seems to be within accuracy. Final topographic maps showing splitting magnitudes and polarization directions using the different data sets were considered reliable.

### **Teleseismic events stacking**

Comparing the topographic map of least lag time error teleseismic stacking with the original teleseismic splitting events topographic map, we noticed similar patterns that are displayed in Figure 3.14. The E-W fast direction exhibited by stations of the Volcanic arc and Eastern regions is identical to original splitting results. Stations in the center of the array as well as several Southern transition stations indicate the same trench-parallel flow. As a check, we have also stacked only 'good' splitting teleseismic events and applied the least lag time error weighted average to create another topographic map shown in Appendix H. This map is almost identical to the original, so the stacking method seems reliable.

One difference with the stacked teleseismic map includes splitting of station BB23. The original map shows a trench-parallel fast orientation (SW-NE), but the stacked version indicates NW-SE. Station BBO8 also exhibits a NW-SE stacked orientation rather than SW-NE. BBO7 mimics this splitting orientation in stacked results where no splitting results are observed in the original.

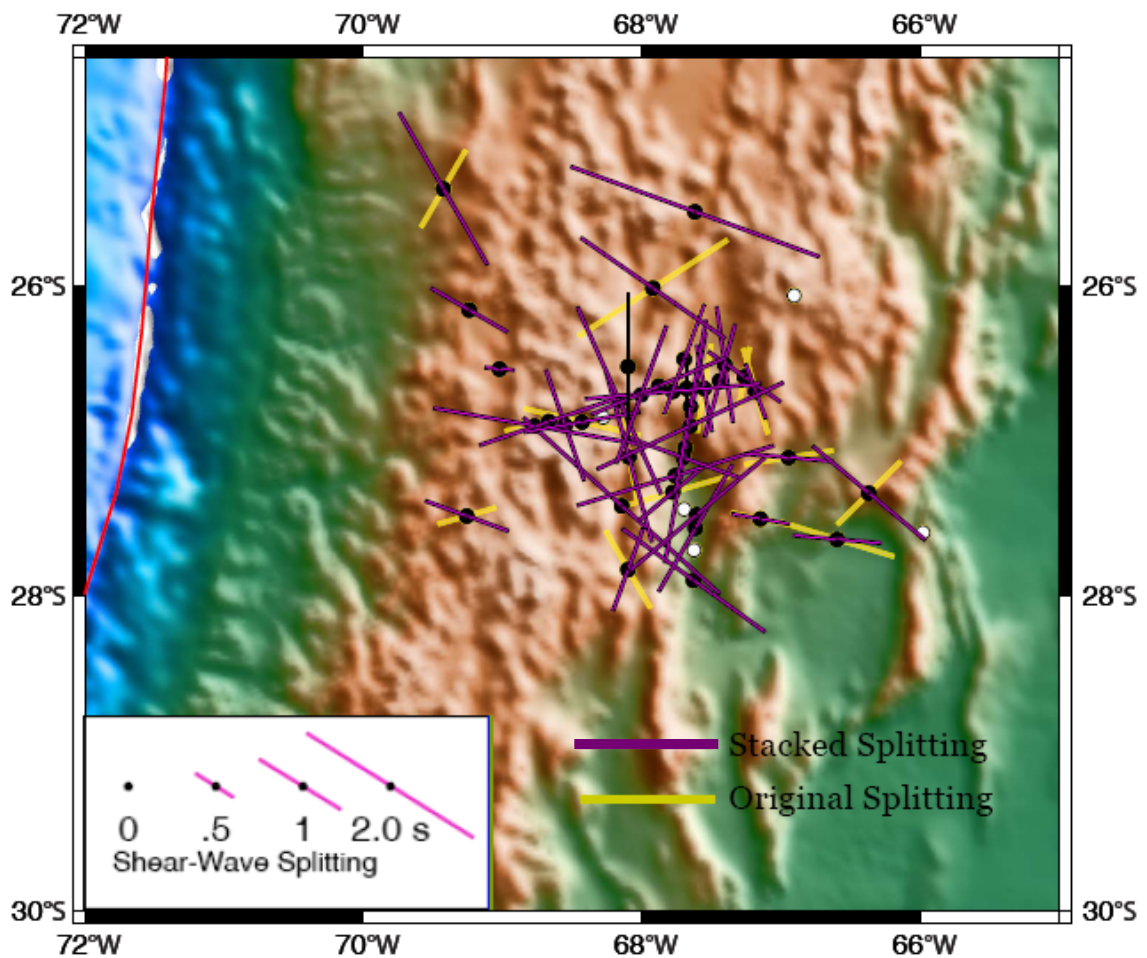


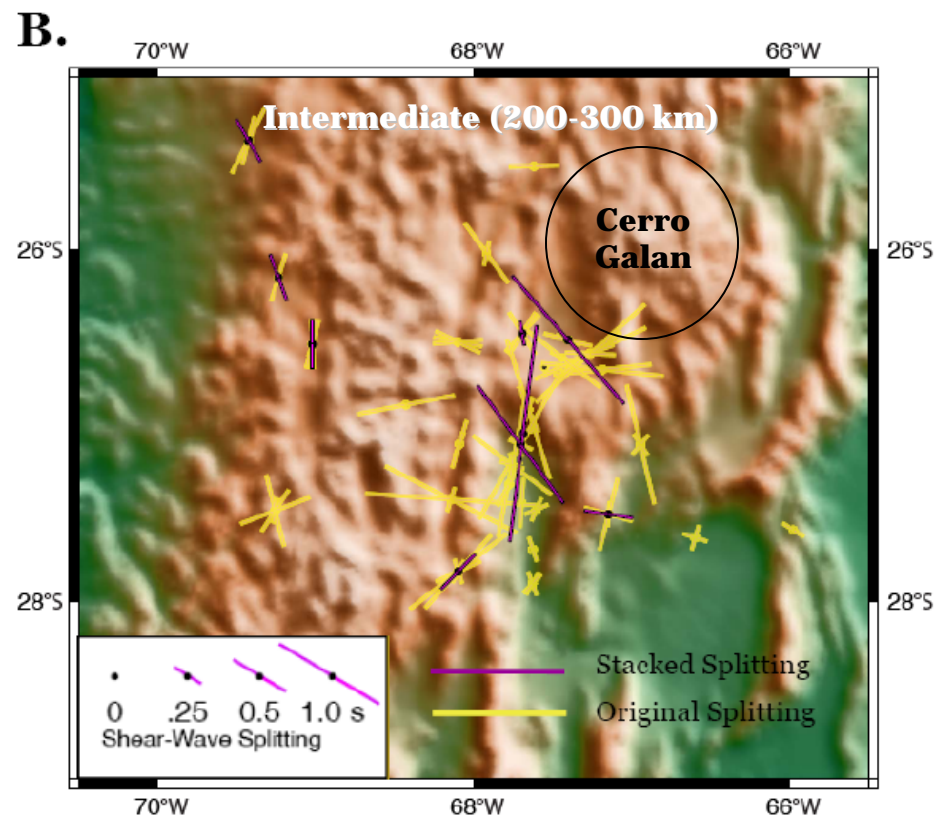
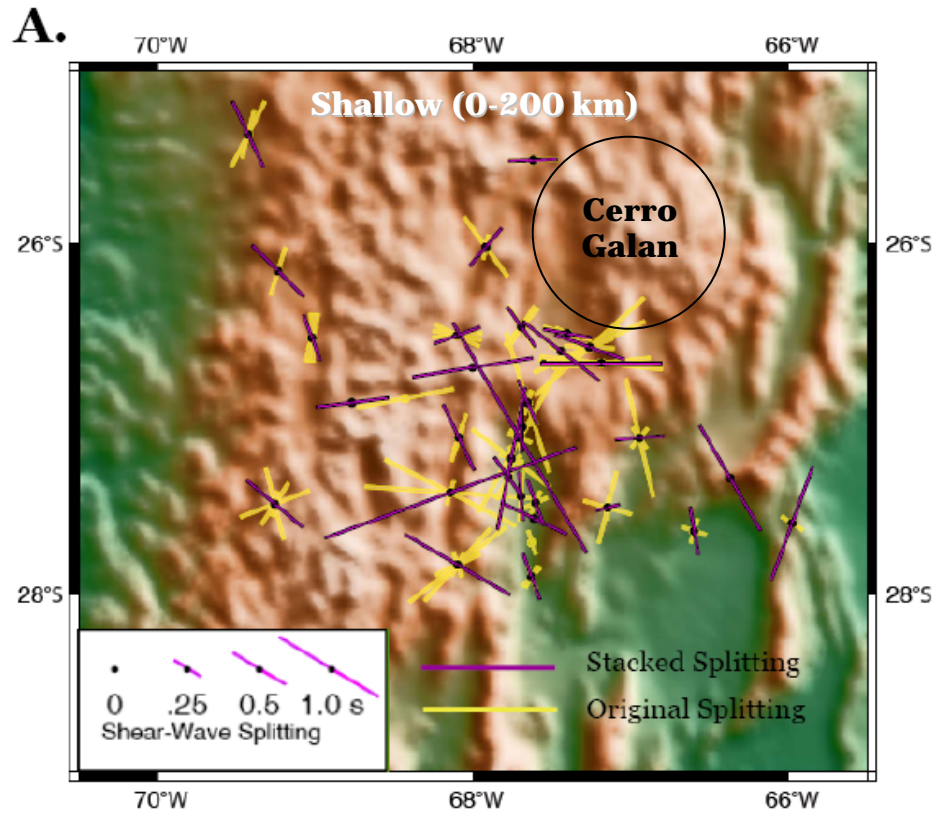
**Figure 3.14.** Stacked teleseismic events splitting compared to original. Splitting results from least lag time error weighted teleseismic stacking (purple) are plotted with original teleseismic splitting events results (yellow) for a comparison. Most stacking results agree with original splitting results. However, the most northern stations indicate splitting orientations of NW-SE where original results show SW-NE. This is possibly an important azimuthal anisotropic characteristic that is discovered by including ‘noisy’ split events from a particular source direction.

### Local events stacking

Two separate stacks were completed for local splitting events as shown in Appendix H. The first set includes splitting at all depths with delay times of 0.3 seconds or greater. To reduce the effects of crustal splitting on the stacks, a

second set was created for all depths that contained only delay times of 0.4 seconds or greater. This discussion focuses on the splitting set with delay times of 0.4 seconds or greater.

By dividing local events splitting into depth regions, some aspects of the anisotropy become clearer. A comparison of these stacked depths with all original local splitting is shown in Figure 3.15. Shallow stacked splitting shows consistency with original local events stacking. A slight orientation change to NW-SE occurs in the Volcanic arc region much like teleseismic stacking showed. A strong E-W flow orientation exists in the center of the array as well as NW-SE orientation. A strong toroidal mantle flow pattern is also observed at the southwest corner of Cerro Galan. This pattern is not observed quite as well with the original splitting. Moving deeper to the intermediate stacking map, we notice that the Volcanic arc trench-parallel fast direction is still present as well as the trench-parallel splitting within the center of the array. The E-W splitting in the center is not visible, and the toroidal flow pattern near Cerro Galan is barely present. The deepest stack of local splitting events shows the main trench-parallel fast directions for the Volcanic arc region. The E-W flow orientation is visible again for center stations along with the N-S orientation.



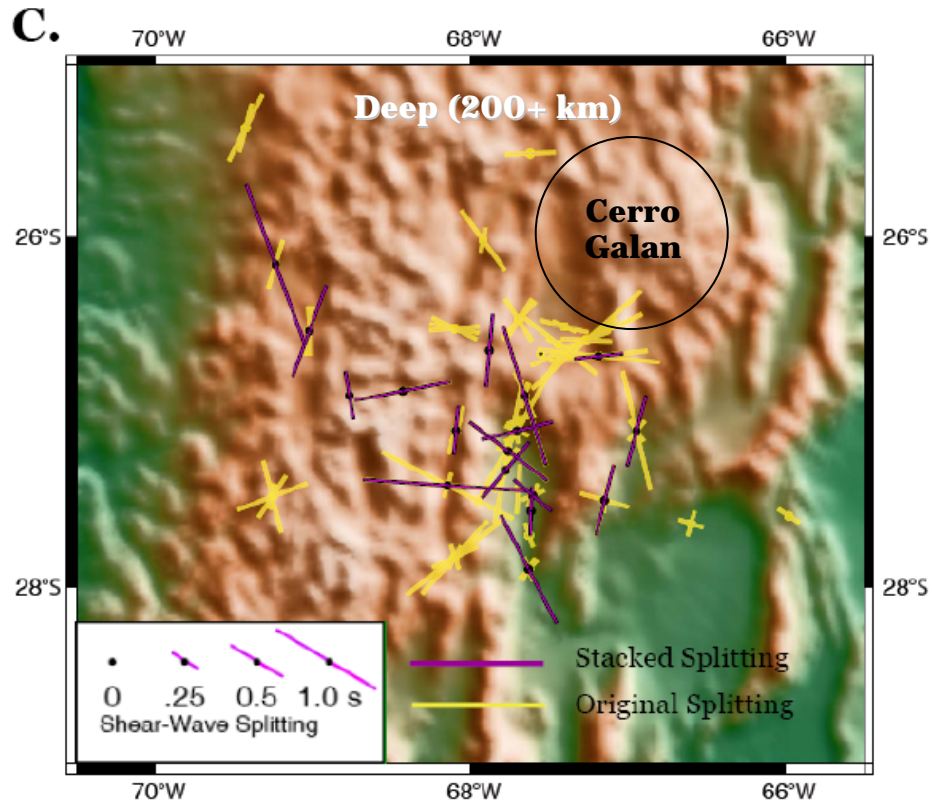


**Figure 3.15.** Local events stacked splitting compared with original. Using a least lag time error weight, results of local stacked events (purple) with delay times of 0.4 seconds or greater are compared to original local events splitting results (yellow) according to depth range. The most notable feature found using the stacking procedure is shown in the shallow depth region where a clear toroidal flow pattern is observed around Cerro Galan. Plots are divided according to depth. A. Shallow. B. Intermediate. C. Deep.

## ASTHENOSPHERIC MOTION

Anisotropy and tectonic processes are mainly related by stress and fluid-filled cracks, lithospheric deformation from stress and strain, consistent mantle and crustal deformation, mineral orientations from past episodes that have been frozen-in, and the large-scale flow of the asthenosphere associated with tectonic plates (Savage, 1999). The latter is most importantly involved with this research.

The motion of tectonic plates at the surface and subducting slabs below are the simplest indicators of mantle flow. The upper mantle should be coupled to the bottom of a tectonic plate, so the motion of the plate should define the motion of the mantle. Hence, coupled mantle material beneath a subducting slab will trail the subducting slab, and flow direction will be that of absolute plate motion (APM). Similarly, material above the subducting slab in the mantle wedge should parallel relative plate motion (RPM). The South America and Nazca Plates are converging with practically no obliquity, so APM directions are parallel to RPM directions. Because of this, mantle flow is expected to be quite simple (Russo and Silver, 1994). However, some regions can have rapid variations in splitting parameters that do not match the movement of plates. These types of variations suggest local small-scale asthenospheric flows. This could be explained by localized disruptions in the mantle flow field caused by a delamination event.

Mantle flow patterns can become complicated closer to the trench. Water content can affect anisotropy orientation by deformation, thin melt sheets that produce trench-parallel fast directions, and also transpressional deformation of the overlying plate (Smith et al., 2001). The effect of water should be restricted to mantle wedge anisotropy. However, there is not an obvious reason to expect extremely abrupt changes in water content of the uppermost mantle minerals below the Puna plateau.

## **Global flow patterns**

Numerous studies of shear-wave splitting have been completed at different tectonic boundaries, each kind illustrating different patterns of mantle flow. Some results have shown complicated flow patterns that imply extremely complex tectonic areas, and other results show unusual flow patterns.

Smith et al. (2001) found a complex mantle flow in the Lau Backarc of the Tonga trench. Although water content was considered as a factor affecting deformation and LPO along the trench, a clear rotational flow pattern was observed and attributed to a tear in the subducting slab. A similar pattern of rotation was found by Civello and Margheriti (2004) around the Calabrian slab of Italy. They considered the toroidal flow pattern a product of the retreating slab as mantle material flows around it rather than underneath the slab.

Zhao and Zheng (2007) found complex shear-wave splitting results beneath the North China craton that suggest lithospheric thinning. Results show large delay times at the northern end of their profile oriented NE-SW, null events in the center of the profile, and average delay times of the southern end oriented NE-SW, rotating clockwise to the south. They attributed these results to lithospheric delamination as the asthenosphere would flow vertically over the delaminated portion from South to North.

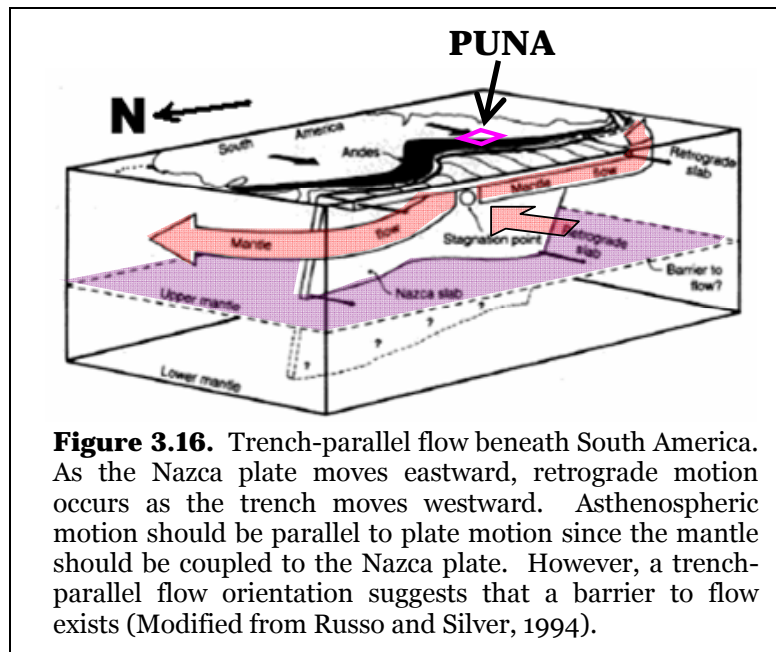
## **Flow patterns of South America**

Generally beneath South America, we expect to find a two-dimensional simple flow model parallel to APM direction. Russo and Silver (1994) discovered,

however, that most of the mantle beneath the Nazca slab flows in a trench-parallel direction. Because larger delay times were observed within their results, the flow layer is assumed to be thick, possibly 100-200 kilometers based on anisotropy values. A trench-parallel flow direction signifies mantle decoupling from the subducting slab. The subducting slab then acts only as a boundary and can only affect the mantle in the subslab by transmitting normal stress, moving the slab toward or away from the overriding plate.

The subducting slab, or Nazca trench, moves westward as the actual plate moves eastward, rendering a retrograde motion. This backward-type motion is thought to be the cause of the trench-parallel mantle flow as a barrier could exist at the end of the subducting slab, forcing lateral mantle flow instead of escaping underneath the slab (Figure 3.16). If the entire 7,000 kilometer trench length of the South American continent is undergoing retrograde motion, the northern

portion should have a northern trench-parallel flow, the southern portion should exhibit a southern trench-parallel flow, and a stagnation point between the two should signify very little trench-parallel flow. Maximum pressure



occurs at this stagnation point located at the 'Bolivian orocline' (Russo and Silver, 1994).

In addition to slab retrograde motion, slab morphology can have a local effect on mantle flow. A tear in the slab would directly influence mantle flow as it would provide a channel for mantle material to reach the opposite side of the slab. At locations where slab dip is transitioning, it is possible to have a slab tear. However, slab transitions beneath South America do not seem to have associated tears (Cahill and Isacks, 1992). Therefore, a trench-parallel flow is necessary for mantle material to flow from the Pacific basin into the Atlantic and Indian basins, guided by absolute plate motion (Russo and Silver, 1994; 1996).

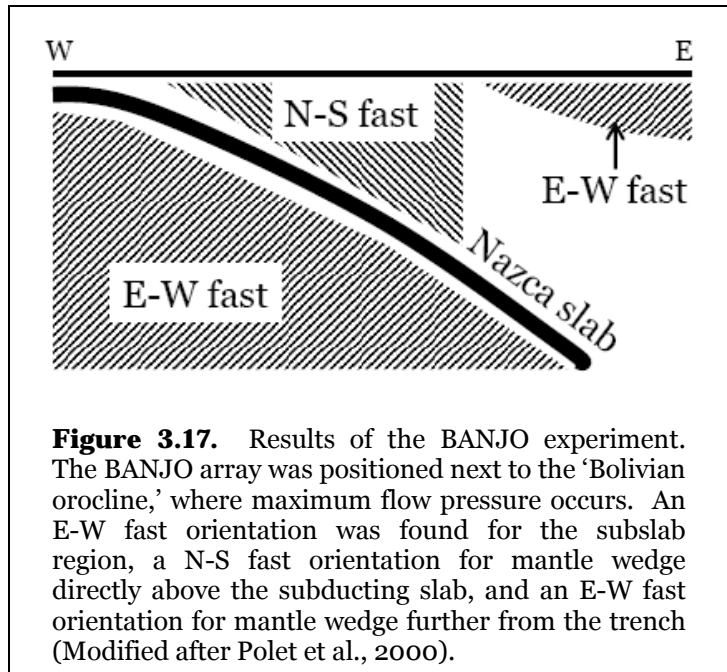
The southern Puna seismic gap has provoked arguments concerning the functionality of the transition. Febrer et al. (1982) first proposed the idea for the existence of a tear in the subducting slab as a consequence of stress from opposing subduction angles. A tear of this nature would allow asthenospheric flow through the break and therefore a temperature increase. However, more recent seismic studies of the southern transition zone imply that the subducting slab remains intact (Kay et al., 1994).

Results of Polet et al. (2000) showed that most shear-wave splitting fast directions were either at a trench-normal (E-W) or a trench-parallel direction in the central Andean plateau. They investigated three separate arrays: BANJO, SEDA, and PISCO. The BANJO array showed E-W fast directions in the subslab region, which occurs at the Bolivian orocline (Figure 3.17). This region displayed the simple two-dimensional model that appeared to transition to the north and

south. The SEDA and PISCO arrays to the north and south of BANJO showed trench-parallel fast directions construed to be subslab components.

Mantle wedge anisotropy was found to exist within these arrays as well. The overall fast direction of the above-slab component was oriented N-S, also not consistent with the

predicted simple corner flow model. Polet et al. (2000) described this N-S direction as caused by the E-W shortening of the South American plate and growth of the Andes Mountains. In this case, the strain within the South American Plate controls the N-S fast direction rather than RPM.



### South America and delamination

A study of crustal thickness using crustal topography, Moho depth, and gravity suggests that the Altiplano and Puna have a felsic crust to a depth of 50-55 kilometers. A mafic composition exists below this, suggesting that critical thickness has been achieved. Any further thickening leads to an increase in density causing delamination, or a gravity-driven detachment from the lower

crust. In addition to compression, a change in crustal density could be caused by the eclogitization of lower crustal material (Gilbert et al., 2006).

Yuan et al. (2002) imply the possibility that the Altiplano might have undergone a lithospheric detachment in the past. New lithosphere is thought to have accumulated from underthrusting of the Brazilian shield. Furthermore, material of the Puna is thought to be in the detachment stage as mafic material of the lower crust is mostly absent. Yuan et al. (2002) believe a piece of delaminated crust rests on the Nazca Plate near 23°S of the northern Puna at a depth of 100 kilometers. Kay and Kay (1993) and Kay et al. (1994) believe that lithospheric detachment has occurred at 26°S based on volcanic composition.

## **TECTONIC IMPLICATIONS**

The results of the southern Puna plateau imply a very complex pattern of mantle flow. General depth-constrained splitting results of the four Puna regions have been combined into one model shown in Figure 3.18. Fast polarization directions with orientations nearly N-S are attributed to trench-parallel asthenospheric flow. This type of behavior exists mostly in the subslab regions beneath for the Volcanic arc, Puna plateau, and Southern transition region. Splitting orientations that are nearly E-W are caused by trench-perpendicular asthenospheric flow. This splitting pattern is viewed both in the subslab and mantle wedge. Within the subslab, some stations of the Southern transition and

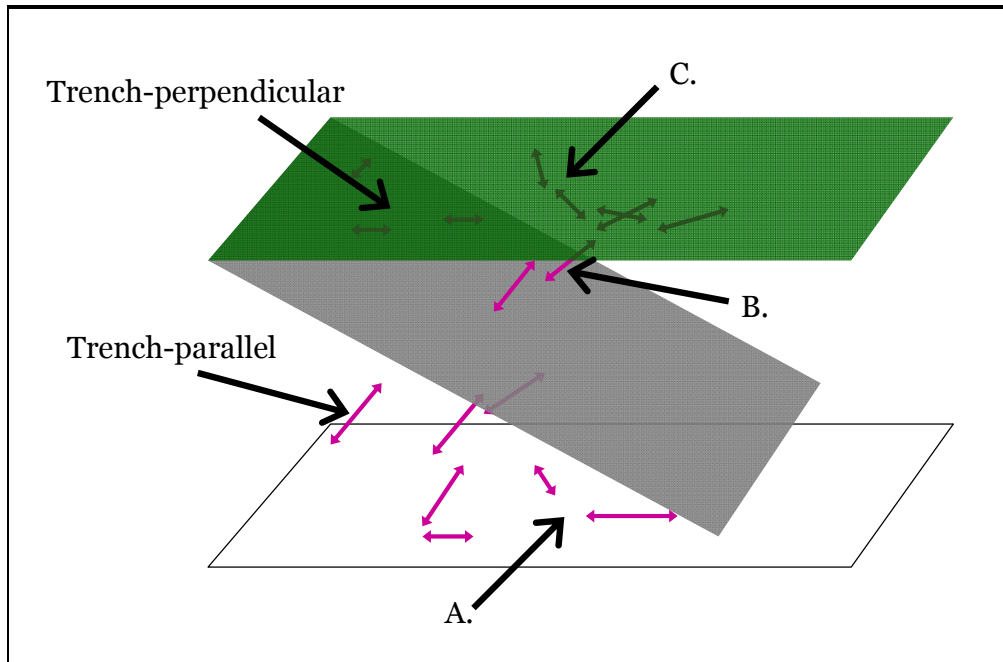


**Figure 3.18.** Model of general flow patterns. Regional splitting patterns from Figure 3.9 were combined to form a general model describing the splitting patterns of PUNA results. A trench-perpendicular mantle wedge pattern is expected, a trench-parallel subslab pattern is expected, but regions A, B, and C are unexpected.

Eastern regions display the E-W orientation. Stations within the Volcanic arc, Southern transition, and Eastern regions show trench-perpendicular flow in the mantle wedge. Finally, a complex mantle wedge flow is observed within the Puna plateau, Southern transition, and Eastern regions.

### **Trench-parallel motion**

Results show subslab asthenospheric flow parallel to the trench which matches shear-wave splitting results of similar studies along the Andean margin (Russo and Silver, 1994; Anderson et al., 2004). This flow pattern has been attributed to slab retrograde motion as the South American Plate moves westward over the Nazca Plate. Instead of flowing parallel to plate motion, the mantle moves laterally and independently of the lower slab to escape the barrier

the encroaching slab creates. Some unexpected trench-parallel flow is observed for the mantle wedge region. Baccheschi et al. (2007) note that shear deformation of the mantle from water released in subduction zones can rotate olivine crystals so that the fast axis aligns subparallel to flow direction (Zhang and Karato, 1995; Jung and Karato, 2001). However, these changes in fast direction can only be explained for high stress conditions and are likely limited in the mantle wedge to the top of the downgoing slab in front of the volcanic arc (Kneller et al., 2005).

### **Trench-perpendicular motion**

Results also show asthenospheric flow perpendicular to the trench where the mantle follows plate motion. This type of flow is expected for the above slab component. Allmendinger et al. (2007) plotted strain rates from GPS to illustrate horizontal surface deformation of South America. They found the general trend to parallel plate convergence direction, an E-W orientation. We have overlapped these strain patterns with our splitting results for comparison (Figure 3.19). The E-W oriented splitting results match strain patterns suggesting a source of APM and RPM. However, because the strain measurements of Allmendinger et al. (2007) have a GPS source, the resulting strain is considered instantaneous rather than finite, which does not truly describe plate motion over large periods of time.

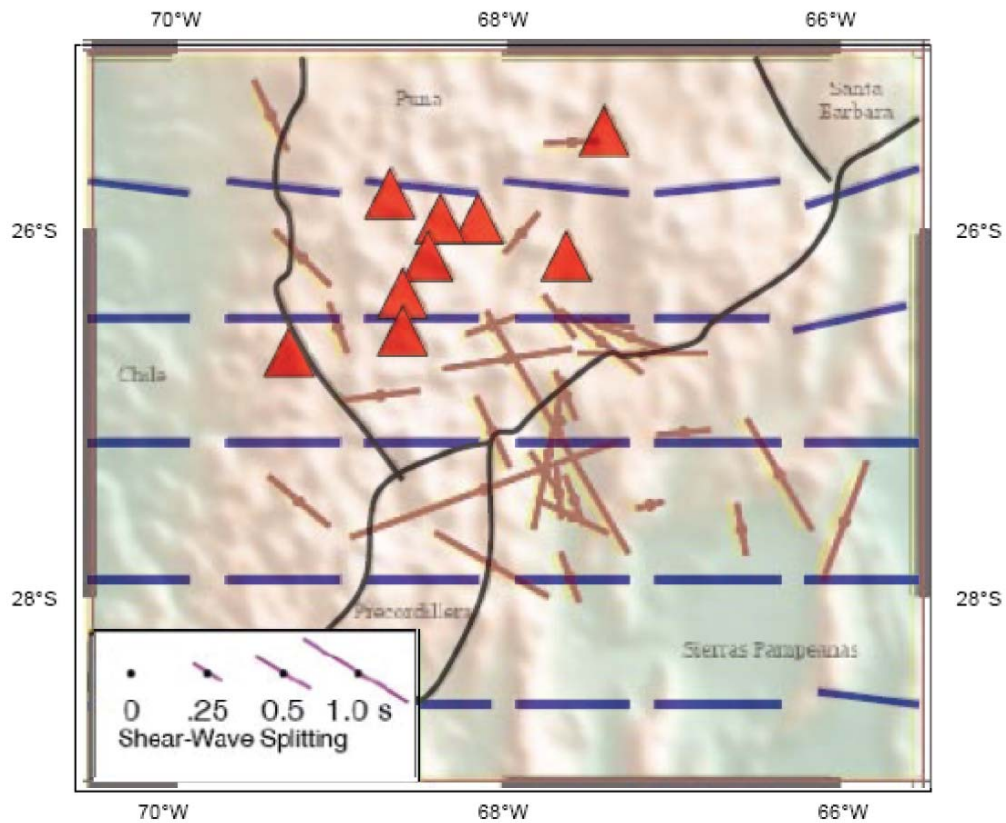


**Figure 3.19.** Comparison of stacked local shallow splitting to strain patterns. Stations of the Southern transition and Eastern regions display a pattern (red) parallel with strain (blue). These regions exhibit mantle flow behavior that is caused from APM or RPM. This comparison should be regarded with caution though as the strain patterns represent instantaneous strain rather than finite (Modified after Allmendinger et al., 2007).

### Complex flow patterns

While subslab trench-parallel and mantle wedge trench-perpendicular flow patterns have been identified, Figure 3.18 demonstrates three regions of unexpected flow patterns. Subslab trench-perpendicular behavior is unexpected along a trench of this nature since this part of the margin lacks high compression. However, the perpendicular behavior occurs where the subducting slab transitions from a steep to flat angle and could be caused by mantle escape. A

slab tear could exist and would allow mantle escape. This type of flow would show fast directions following mantle strain caused by the curve of the slab up to the slab tear (Peyton et al., 2001; Baccheschi et al., 2007). Cahill and Isacks (1992) state that slab tears along the South American subduction margin are not expected though as continuous slab flexure occurs with a changing dip.

In the instance of a slab tear, fast polarization orientations should closely parallel subducting slab depth contours until the tear where the orientation becomes perpendicular. Fast polarization orientations were plotted against depth contours for a comparison (Figure 3.20). We observe that the region in question shows splitting orientations that do not follow the contours. While this behavior might normally represent a slab tear, these splitting orientations are not abruptly perpendicular to contours either.

The changing orientations are likely attributed to a mantle escape caused by slab flattening (Figure 3.21). The transition in subduction angle likely causes a break in the slab boundary causing lateral flow along the rest of the margin. Anderson et al. (2004) found similar results on the southern portion of this central Chile flatslab. The mantle wedge splitting pattern in question of the Southern transition region is also likely attributed to this slab transition. While most of the flow pattern follows the E-W oriented APM guidelines, splitting of this area plots more SW-NE. Under slab flexure such as this, compensation will occur that causes sharp bends in the plate where mantle material can readily flow, or an inflow occurs from pressure differences.

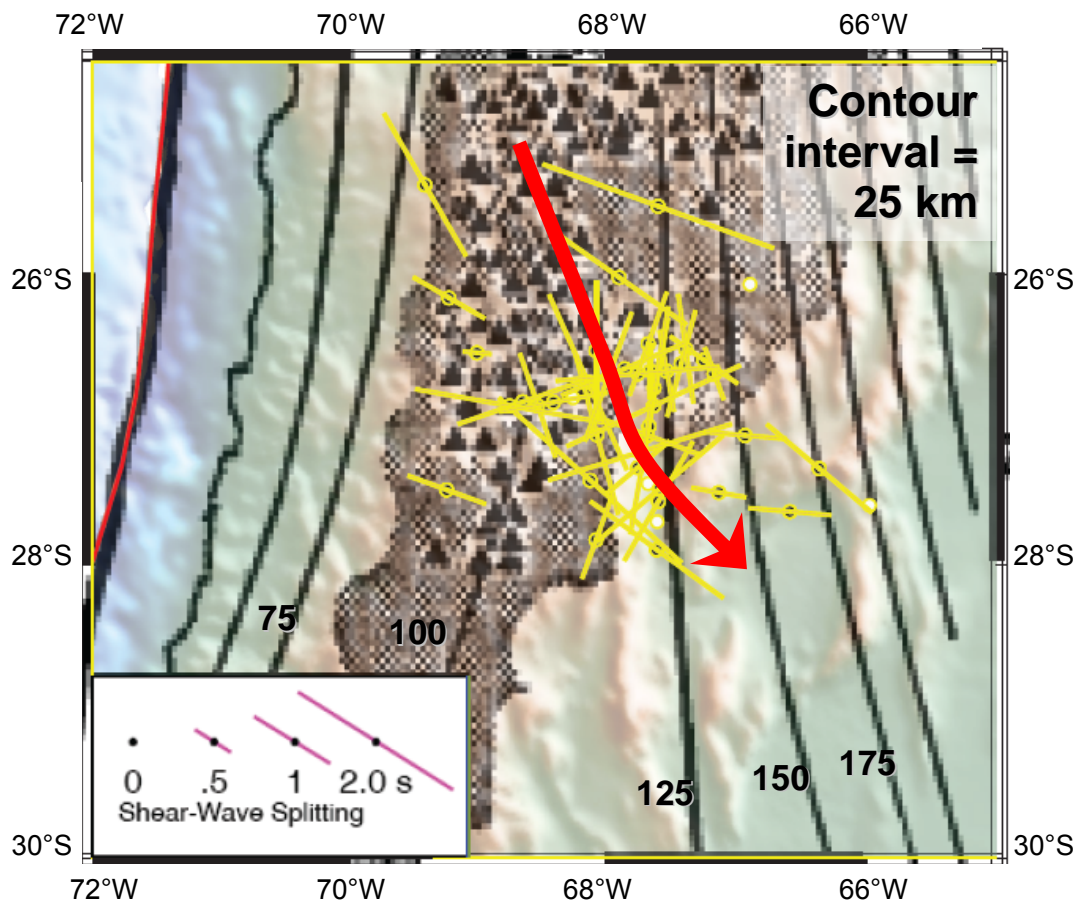


**Figure 3.20.** Comparison of stacked teleseismic splitting with slab contours. Stations of the Volcanic arc region and parts of the Southern transition region show fast directions parallel to subducting slab contours. The slab flattens where the contour lines spread apart, and mantle flow patterns are expected to mimic this behavior. A gradual perpendicular behavior of splitting results suggests a mantle escape underneath the flatslab, which is illustrated by the red arrow (Modified after Cahill and Isacks, 1992).

The final area in question lies in the mantle wedge of the Eastern region near Cerro Galan. A clear toroidal flow pattern is observed in the stacked shallow local events results. This region was suggested by Kay and Kay (1993) and Kay et al. (1994) to have undergone delamination.

Several shear-wave splitting studies have investigated the possibility of a delamination event. Buontempo et al. (2008) state that a delamination model would require an asthenospheric flow directed radially inwards from all directions to replace detached lithosphere. Their study of shear-wave splitting beneath southern Iberia did not show a radial pattern, but a rotation does exist. They explain this with a toroidal mantle flow pattern that shows slab rollback toward the west along slab curvature. Zhao and Zheng (2007) also predicted a mantle flow model for delamination where the asthenosphere replaces the

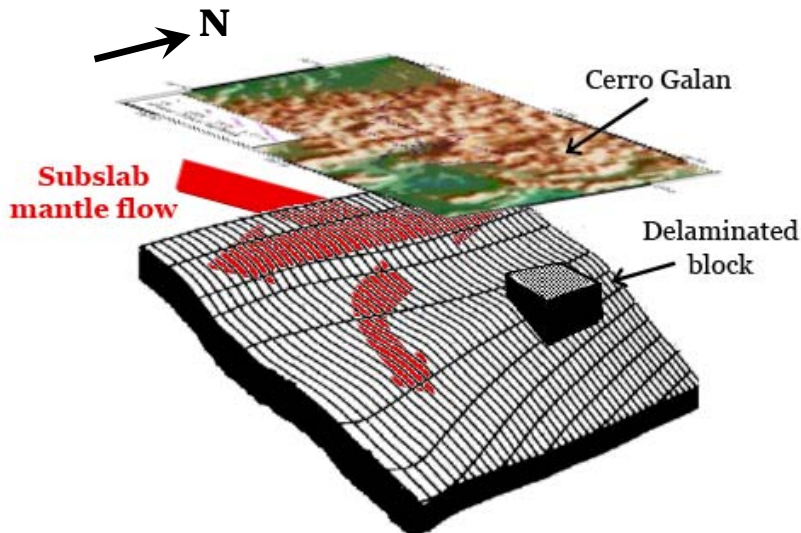


**Figure 3.21.** General tectonic model of subslab mantle flow. Asthenosphere flows trench-parallel beneath the subducting slab except where the slab shallows. This trench-perpendicular flow is likely due to mantle escape (After Cahill and Isacks, 1992).

delaminated portion. Fast directions would dominantly parallel the direction of mantle flow over the delaminated area, and ascending asthenosphere to

the outsides of this area would show no splitting from vertical fast directions. Also, a pressure gradient would force other asthenospheric material towards the detached area. West et al. (2009) also associated shear-wave splitting results beneath the Great Basin to delamination, or a 'lithospheric drip.' They believe

the toroidal flow pattern found beneath the region was produced from the retreating Juan de Fuca slab. Smaller splitting times of the region are caused by a localized shift to vertical flow above and around the delaminated portion, or the ‘drip.’

The toroidal pattern observed in the Eastern region most generally suggests circular flow movement. This type of pattern is likely to occur as flowing material avoids an obstacle (Figure 3.22). A radial pattern is thought to be attributed with a delamination event as material flows towards a common center. We do not observe this in our results, but our recording stations might not have been geographically positioned to detect this behavior. Furthermore, station BB19 was placed near the center of Cerro Galan and shows null results, or no splitting. As stated earlier, null results can imply an isotropic region or more importantly a region where the fast direction is vertically

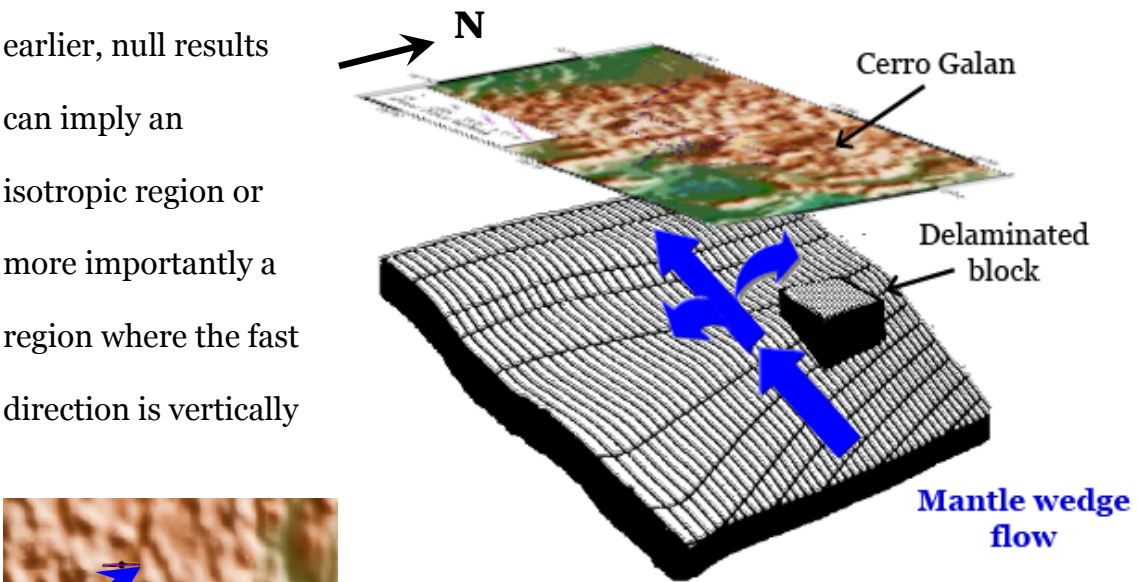


**Figure 3.22.** General tectonic model describing mantle wedge flow. Asthenosphere flows trench-perpendicular in the mantle wedge. Flow behavior opposite of this is attributed to slab flexure compensation and obstacle avoidance. A delaminated block is the obstacle in this case. Splitting patterns demonstrate toroidal behavior (From Cahill and Isacks, 1992).

oriented. Nevertheless, the toroidal flow pattern near Cerro Galan is more than likely tied to the ignimbrite. Ignimbrite flare-ups have been deemed a consequence of delamination as an increase in mantle input occurs, causing widespread crustal magmatism, and large volumes of magma ascend until eruption occurs from mechanical failure of the magma chamber roof (de Silva et al., 2006a). Because of the link between ignimbrites and delamination, it seems possible that a block of lithosphere in this region may be the obstruction. This block could therefore cause complex mantle flow around it. If a block of lithosphere is present, it is possible that delamination occurred.

## **CHAPTER 4: Summary and Conclusions**

This study was aimed at testing the hypothesis first proposed by Kay and Kay (1993) that uplift of the southern Puna plateau occurred as a consequence of the removal of underlying lithospheric crust and mantle through an episode of delamination. This goal was achieved by studying asthenospheric flow patterns beneath this region through shear-wave splitting measurements caused by anisotropic layers of the mantle that might be associated with anomalous features of the southern Puna plateau pointing to delamination.

To illustrate and confine the location and extent of seismic anisotropy within the mantle beneath the Puna, this study maintained three major objectives throughout the processing of shear-wave splitting measurements. These objectives included: 1) determining fast polarization directions and delay times of splitting events, 2) providing a vertical constraint on mantle anisotropy using both teleseismic and local events, and 3) finding any localized splitting dependencies.

Of the PUNA array, 43 stations have provided data from 30 teleseismic events and 88 local events which demonstrate shear-wave splitting. In completing the aforementioned objectives, results of the southern Puna plateau imply that complex flow behavior is involved with the subducting slab. Subslab splitting patterns show a trench-parallel behavior indicative of retrograde slab

motion. However, trench-perpendicular flow behavior exists in the steep-to-flat subduction transition zone which suggests a mantle escape underneath the flatslab. Flow patterns of the mantle wedge indicate motion related and coupled to plate motion with trench-perpendicular fast directions that rotate to trench-parallel as a result of slab flattening. Finally, the region near Cerro Galan shows a toroidal mantle wedge flow pattern surrounding the giant ignimbrite. Although delamination is not directly observed, the rotating mantle flow pattern indicates that an obstruction might exist in the Cerro Galan region forcing flow orientation to vary according to the location of the obstruction. Because ignimbrites are linked with delamination, a block of delaminated lithosphere is likely causing the flow obstruction. Under this assumption, we confirm the original hypothesis of Kay and Kay (1993).

The PUNA array is the first seismic study involving stations located in the southern Puna plateau. As a preliminary study of lithospheric structure for this region, the findings of this research should be further developed. This particular thesis work serves as preliminary results for the entire PUNA seismic array. As stated in Chapter 2, a set of German seismic stations completes the array. These stations extend northeast of the US stations and better cover the Cerro Galan region. With the addition of data from these stations, a better illustration of mantle flow patterns around Cerro Galan can aid in developing more conclusive interpretations. Investigation of this region is crucial in studying lithospheric delamination of the Puna plateau.

We used a number of shear-wave splitting methods for this study; however, other methods exist that could potentially advance data results. For instance, Šilený and Plomerová (1996) examine splitting for three components, or out-of-horizontal plane motion. This type of study is useful for nearly vertical incidence angles where the ray has earlier passed through anisotropic material at lower incidence angles. Methods such as this could reduce data errors. Other useful methods might include searching for splitting of teleseismic S-waves or modifying the stacking procedure used within this study.

Others have researched areas surrounding the southern Puna plateau using other seismic methods. For instance, Schurr et al. (2006) completed a study using tomographic inversion for the southern central Andes from 20°S-25°S. They generated tomographic models of P-wave velocity, P-wave attenuation, and  $v_p/v_s$  ratio. In doing so, they imaged a fast, high- $Q_p$  body near 23°S and interpreted it as detaching lithosphere dipping westward from the eastern Puna crust. Imaging farther south at 24°S illustrates slab thickening above the Benioff zone, suggesting a body resting atop the subducting Nazca plate. This region is also the location of the strato-volcano Cerro Tuzgle, which likely formed in response to lithospheric detachment directly below.

Future recommendations for this research include work on velocity and attenuation structure to further analyze interpretations of localized variations in shear-wave splitting patterns (slab tear, abrupt change in slab subduction angle, and delamination). Tomographic modeling will better visualize lithospheric structure beneath the southern Puna using velocity of phases such as Pn for

possible comparisons with Pn anisotropy models and attenuation studies using phases like Sn which is sensitive to mantle lid rheology. Further work includes determining crustal thickness beneath each station by using teleseismic receiver functions. Discovering regions of thinner crust will facilitate in determining regions of possible lithospheric delamination events.

The results of this particular preliminary research point to an episode of delamination within the southern Puna plateau. Although the original hypothesis cannot be proven, these results do not disprove it. Additional research using tomographic modeling will provide more conclusive results on lithospheric structure. If a delamination event is determined to have occurred within the Puna, implications can be made for lithospheric evolution of similar orogenic systems of the past, present, and future.

## Appendix A: Matlab stacking code

### Basic code for all for weighting factors:

```
clear;

files = dir('*.energy.sks');

% get data into matlab
for i=1:length(files)

    fid = fopen(files(i).name);
    infilename = textscan(fid,'%s');
    fclose(fid);
    infilename = infilename{:};
    sampling = strmatch('SAMPLING',infilename);
    first = sampling + 14;
    last = first + 10859;
    data = infilename(first:last);

% change cell array to number array
    S = char(data);
    energy = str2num(S);
    AllData(:,i)=energy;
end

% Insert code for specific weighting factor HERE

% assign one matrix as the weight
[Min,position] = min(all);
weight=AllData(:,position);

% Find weighted average vector
variance = AllData-repmat(weight,1,length(files));
Variance = variance.^2;
row_sum = sum(Variance)';
percentage = Variance./repmat(row_sum,1,length(files));
normalization = 1-percentage;
Weight = normalization.*AllData;
ROW_SUM = sum(Weight)';
Row_Sum = sum(normalization)';
WeightedAvg = ROW_SUM./Row_Sum;

% Plot weighted average matrix contours
transform = WeightedAvg';
matrix = reshape(transform,60,181);
Z=matrix.';
contour(Z)
set(gca,'YTick',0:20:180);
set(gca,'YTickLabel',[-90:20:90]);
set(gca,'XTick',0:12.5:60);
set(gca,'XTickLabel',[0:0.5:2+15/44]);
xlabel('Delta T (sec)');
```

```
YLabel('Phi (degrees)');  
hold on
```

```
[values columns] = (min(Z))  
[val column] = min(min(Z))  
row = columns(1,column)  
minval = Z(row,column)  
point = plot(column,row,'b*')  
set(point,'MarkerSize',12)
```

-----  
%% Codes for specific weighting factors:

```
% find the minimum delay time error  
for i=1:length(files)  
    fid = fopen(files(i).name);  
    out = textscan(fid,'%s');  
    fclose(fid);  
    out = out{:};  
    delay = strmatch('DELAY',out);  
    time = delay + 4;  
    which = out(time:time);  
    cell = char(which);  
    m = str2num(cell);  
    all(:,i)=m;  
end
```

```
% find the minimum fast direction error  
for i=1:length(files)  
    fid = fopen(files(i).name);  
    out = textscan(fid,'%s');  
    fclose(fid);  
    out = out{:};  
    angle = strmatch('ANGLE',out);  
    time = angle + 4;  
    which = out(time:time);  
    cell = char(which);  
    m = str2num(cell);  
    all(:,i)=m;  
end
```

```
% find average of minimum values  
[e f] = (min(AllData))  
AvgMin = mean(e);  
diff = (AvgMin - e).^2;  
[smallest,group] = min(diff);  
weight = AllData(:,group)
```

```
% find absolute minimum value  
[e f] = (min(AllData))  
[g h] = min(min(AllData))  
Row = f(1,h)  
weight = AllData(:,h);
```

## Appendix B: Splitting events

List of events showing teleseismic shear-wave splitting. Each event is classified by year, Julian day, and seconds into the day. Source depth, latitude, longitude, body wave magnitude,  $\Delta$  (distance), and BAZ (back azimuth) are also given.

Year	Day	Seconds	Depth (km)	Latitude (°)	Longitude (°)	mb	$\Delta$ (deg)	BAZ (deg)
2007	354	75515.8	20	-39.011	178.291	6.3	89.8	225.51
2008	6	51420.2	75	37.216	22.693	6.1	106.29	56.27
2008	15	175215.7	597	-21.984	-179.535	5.8	97.81	240.63
2008	32	121006.4	604	-21.495	-179.352	5.6	97.93	241.13
2008	45	100922.7	29	36.501	21.67	6.2	105.27	56.64
2008	45	120855.8	28	36.345	21.863	5.9	105.35	56.85
2008	55	144621.5	22	-2.405	99.931	6	148.53	156.41
2008	78	82247.1	25	-29.252	-177.44	5.8	92.29	235.56
2008	103	3012.6	16	-55.664	158.453	6.8	88.64	204.26
2008	109	203907.1	553	-17.342	-179.022	5.9	99.9	244.83
2008	187	21204.5	632	53.882	152.886	6.8	139.75	323.14
2008	273	151931.6	36	-29.756	-177.683	6.5	92.2	235.02
2008	344	62359.8	18	-31.232	-176.924	6.2	90.85	234.14
2009	15	174939.1	36	46.857	155.154	6.9	140.82	312.02
2009	18	141148.9	33	-30.199	-177.951	6	92.15	234.53
2009	22	134026	44	-5.912	148.511	5.6	131.85	232.61
2009	22	201634.6	146	-7.307	128.568	6.1	142.31	207.56

List of events showing local S-wave splitting. Each event is classified by year, Julian day, and seconds into the day. Source depth, latitude, longitude, and body wave magnitude are included.

Year	Day	Seconds	Depth (km)	Latitude (°)	Longitude (°)	mb
2008	2	121700.5	123	-28.22	-67.425	0
2008	14	60428	169	-27.01	-66.455	4.2
2008	18	213301.3	191	-23.613	-66.646	4.3
2008	28	115728.2	170	-24.087	-66.987	4.4
2008	37	95158.5	124	-28.349	-67.4	0
2008	39	155902.1	577	-27.555	-63.34	4.5
2008	46	211605.7	133	-28.784	-67.237	0
2008	74	65511.6	103	-28.497	-67.632	4.4
2008	78	4653.4	159	-24.256	-66.96	4.5
2008	80	12140.8	167	-24.183	-67.064	4.3

---

2008	90	70636	127	-26.108	-68.577	0
2008	97	13206.5	530	-22.141	-63.775	4.3
2008	110	175240.5	117	-28.746	-67.319	4.3
2008	111	53610.8	161	-24.197	-66.857	4.6
2008	114	175131.6	162	-27.923	-66.558	4.8
2008	119	72639.7	200	-24.085	-67.504	4.5
2008	121	111452.2	199	-23.57	-66.61	4.5
2008	128	53425.4	111	-29.088	-67.454	4.7
2008	144	204618.6	100	-22.59	-68.55	5
2008	147	202017.9	208	-22.79	-66.23	4.6
2008	152	233327.3	186	-23.9	-66.6	4.5
2008	163	203515.3	189	-25.434	-66.196	4.5
2008	173	40904.3	150	-24.299	-67.048	4.2
2008	174	121250.5	214	-23.798	-66.521	4.6
2008	177	2658.4	116	-29.068	-67.271	0
2008	196	184000.9	163	-27.932	-66.492	4.6
2008	198	132636.2	156	-27.86	-66.661	4.1
2008	218	233858.8	174	-23.257	-66.874	4.3
2008	220	74424.9	164	-24.019	-66.972	4.2
2008	220	235621.5	120	-24.924	-67.66	4.3
2008	234	93257.6	107	-25.254	-68.697	5.3
2008	246	172733.5	138	-28.038	-67.424	0
2008	247	112514.5	569	-26.736	-63.225	5.9
2008	249	205113.9	156	-24.22	-67.088	4.2
2008	250	175725.7	161	-24.176	-67.075	4.1
2008	257	164730.3	105	-27.883	-68.25	0
2008	259	233652.1	152	-24.166	-66.799	5.1
2008	265	173524.5	563	-26.583	-63.387	4.4
2008	269	175448.3	166	-24.284	-66.861	4.2
2008	315	105614.5	169	-24.207	-66.602	3.8
2008	326	131733.2	181	-24.127	-67.015	4.2
2008	338	23237.9	162	-23.943	-66.869	3.9
2008	345	55655.1	157	-24.29	-67.046	4.4
2008	348	3552.7	164	-27.82	-66.747	3.8
2008	354	15618.1	129	-28.341	-67.333	3.9
2008	354	152101.7	147	-27.97	-66.879	3.8
2008	361	31544.4	186	-24.03	-66.706	4.8
2008	365	45557.9	147	-24.045	-68.101	0
2009	3	211501.6	627	-28.54	-63.011	5.1
2009	15	213121.5	131	-26.568	-67.03	4.3
2009	19	233155.4	176	-24.217	-66.812	4.3

---

## Appendix C: Splitting results

Results of teleseismic shear-wave splitting. Each individual station result is shown by event year, Julian day, hour, and minute. Fast directions and lag times are both shown with error factors. Back azimuths and source distance from the stations are shown as well as the station name and S-phase recorded.

Year	Day	Time	Fast Direction (deg)	Lag Time (s)	BAZ (deg)	$\Delta$ (deg)	Station	Phase
2007	354	7 55	81.0+/- 17.0	1.1+/- 0.6	225.03	90.38	BB11	SKS
2008	6	5 14	-78.0+/- 32.0	0.7+/- 0.6	56.12	105.94	BB12	SKS
2008	15	17 52	3.0+/- 23.0	0.9+/- 0.5	240.44	98.32	NS07	SKS
2008	15	17 52	89.0+/- 6.0	0.8+/- 0.2	240.07	98.57	BB11	SKS
2008	15	17 52	-11.0+/- 14.0	0.9+/- 0.4	240.66	97.69	BB02	SKS
2008	15	17 52	-16.0+/- 14.0	0.8+/- 0.5	240.25	98.6	EW09	SKS
2008	32	12 10	20.0+/- 19.0	1.2+/- 0.6	241.04	98.43	BB10	SKS
2008	32	12 10	-83.0+/- 21.0	1.0+/- 0.5	240.57	98.7	BB11	SKS
2008	45	10 9	41.0+/- 23.0	0.7+/- 0.5	56.18	104.24	BB15	SKS
2008	45	10 9	-8.0+/- 24.0	0.8+/- 0.4	56.31	104.49	EW10	SKS
2008	45	10 9	80.0+/- 28.0	0.7+/- 0.5	56.86	105.79	EW20	SKS
2008	45	12 8	46.0+/- 8.0	1.0+/- 0.5	56.39	104.33	BB15	SKS
2008	55	14 46	30.0+/- 21.0	0.8+/- 0.4	157.97	150.53	BB23	SKKS
2008	78	8 22	-73.0+/- 24.0	0.8+/- 0.3	234.86	92.95	BB13	SKS
2008	103	0 30	40.0+/- 8.0	1.8+/- 0.6	203.8	88.92	BB11	SKS
2008	103	0 30	-30.0+/- 29.0	0.9+/- 0.6	204.31	87.85	BB24	SKS
2008	109	20 39	16.0+/- 21.0	1.0+/- 0.5	244.65	100.4	NS07	SKS
2008	109	20 39	29.0+/- 25.0	0.6+/- 0.3	244.51	100.67	EW10	SKS
2008	187	2 12	77.0+/- 12.0	1.4+/- 0.6	322.99	140.14	NS13	SKS
2008	273	15 19	74.0+/- 4.0	1.3+/- 0.2	234.33	92.85	BB13	SKS
2008	344	6 23	69.0+/- 14.0	0.9+/- 0.5	234.03	90.82	NS13	SKS
2008	344	6 23	76.0+/- 12.0	1.2+/- 0.5	233.47	91.48	BB13	SKS
2008	344	6 23	-77.0+/- 20.0	1.2+/- 0.4	234.33	90.61	EW17	SKS
2009	15	17 49	57.0+/- 6.0	1.6+/- 0.6	312.92	140.21	BB08	PKS
2009	18	14 11	73.0+/- 8.0	1.3+/- 0.4	233.83	92.79	BB13	SKS
2009	22	13 40	6.0+/- 23.0	0.8+/- 0.6	232.43	132.37	NS07	PKS
2009	22	13 40	75.0+/- 12.0	0.9+/- 0.4	231.53	132.52	BB11	PKS
2009	22	13 40	78.0+/- 13.0	0.9+/- 0.4	230.82	132.43	BB13	PKS
2009	22	13 40	82.0+/- 17.0	0.6+/- 0.4	231.44	132.14	BB12	PKS
2009	22	20 16	74.0+/- 23.0	0.7+/- 0.4	209.09	141.35	BB03	PKS

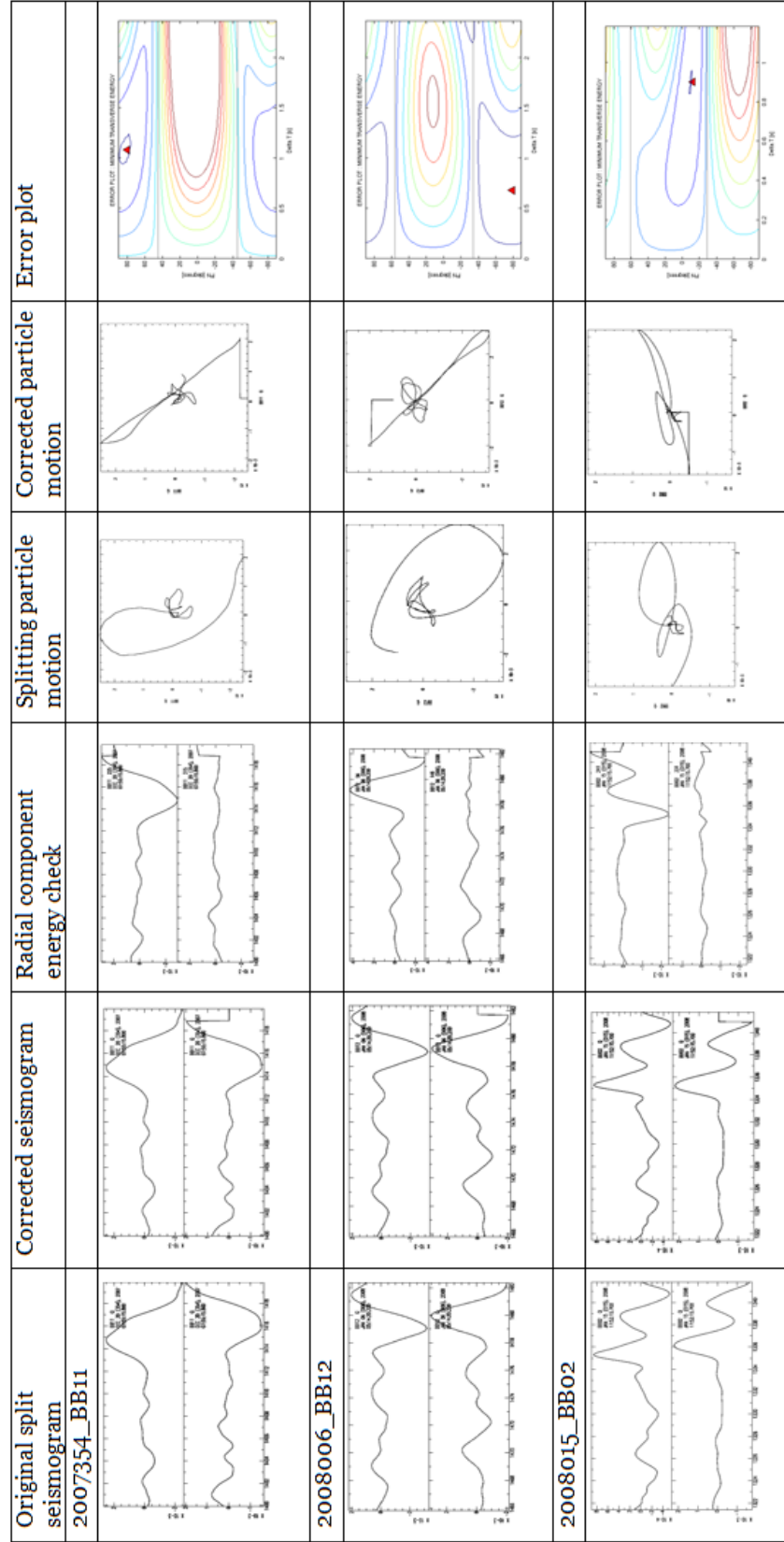
Results of local S-wave splitting. Each individual station result is shown by event year, Julian day, hour, and minute. Fast directions and lag times are both shown with error factors. Back azimuths and source distance from the stations are shown as well as the station name and source depth.

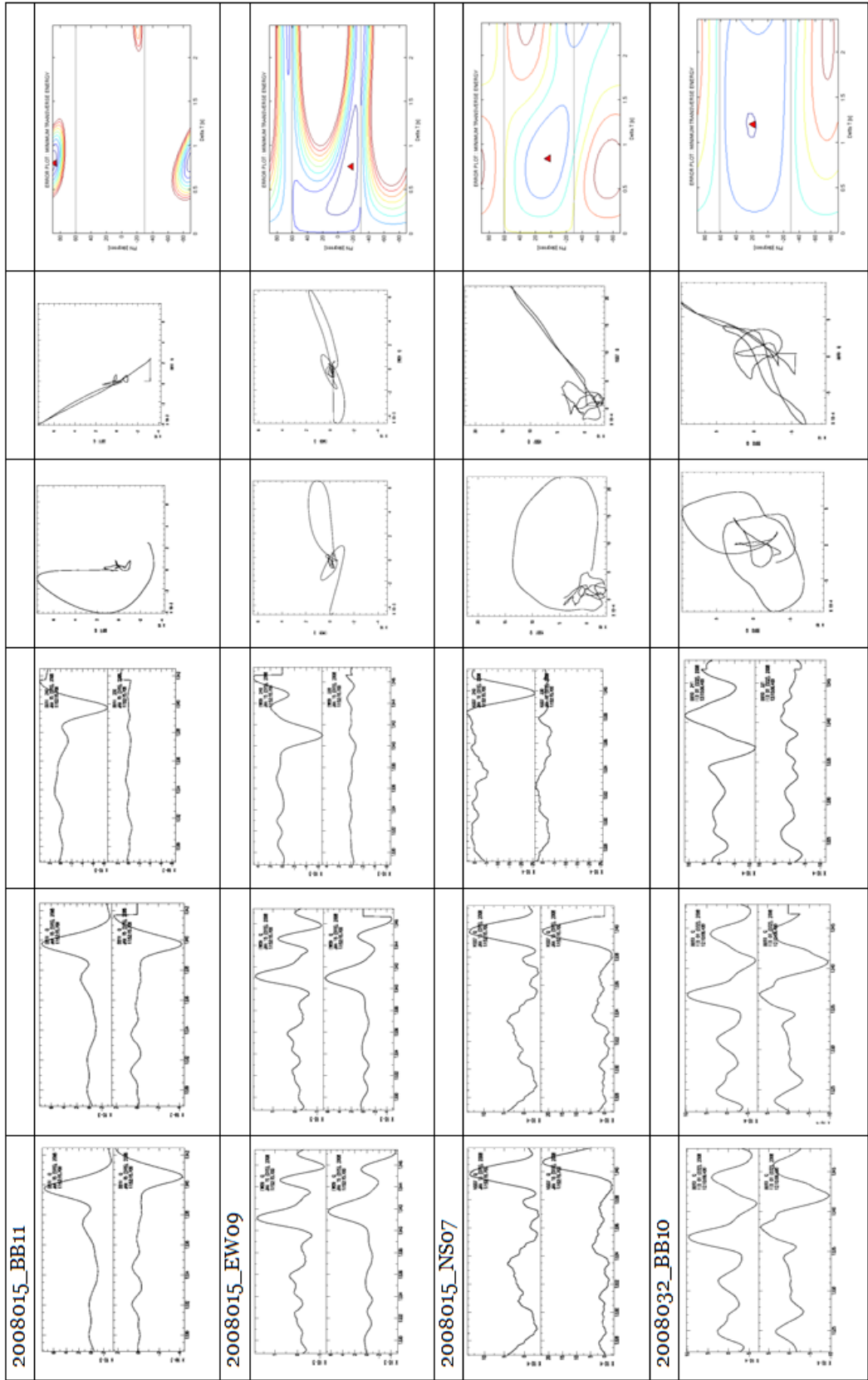
Year	Day	Time	Fast Direction (deg)	Lag Time (s)	BAZ (deg)	$\Delta$ (deg)	Station	Depth (km)
2008	2	12 17	-10.0+/- 18.0	0.3+/- 0.1	163.49	1.03	NS12	123
2008	14	6 4	10.0+/- 18.0	0.2+/- 0.0	79.7	1.18	NS12	169
2008	18	21 33	65.0+/- 17.0	1.0+/- 0.1	10.79	3.02	EW10	191
2008	28	11 57	70.0+/- 11.0	0.5+/- 0.1	5.76	2.51	EW10	170
2008	37	9 51	89.0+/- 11.0	0.1+/- 0.0	162.75	0.67	NS17	124
2008	39	15 59	-53.0+/- 20.0	0.9+/- 0.4	95.75	3.94	NS12	577
2008	46	21 16	-20.0+/- 15.0	0.2+/- 0.0	158.65	0.95	NS18	133
2008	74	6 55	6.0+/- 14.0	0.1+/- 0.1	182.24	1.82	NS07	103
2008	74	6 55	23.0+/- 20.0	0.3+/- 0.0	181.44	1.01	NS15	103
2008	74	6 55	-5.0+/- 20.0	0.3+/- 0.0	177.4	1.38	NS11	103
2008	78	0 46	22.0+/- 11.0	0.3+/- 0.1	19.98	3.02	BB02	159
2008	80	1 21	-36.0+/- 13.0	0.7+/- 0.1	23.17	1.98	BB08	167
2008	90	7 6	12.0+/- 13.0	0.2+/- 0.0	261.07	0.6	BB08	127
2008	97	1 32	4.0+/- 11.0	0.3+/- 0.1	30.42	6.15	BB12	526
2008	97	1 32	-64.0+/- 20.0	0.2+/- 0.1	37.51	5.56	NS06	526
2008	110	17 52	17.0+/- 16.0	0.2+/- 0.1	151.23	1.51	BB01	117
2008	110	17 52	20.0+/- 16.0	0.2+/- 0.0	170.89	1.85	NS09	117
2008	111	5 36	-63.0+/- 12.0	1.2+/- 0.1	20.13	3.42	BB01	161
2008	114	17 51	-8.0+/- 15.0	0.1+/- 0.0	91.57	0.95	NS18	162
2008	119	7 26	17.0+/- 16.0	0.4+/- 0.1	37.66	2.59	BB22	200
2008	121	11 14	88.0+/- 20.0	0.4+/- 0.1	25.56	2.14	BB07	199
2008	121	16 43	-79.0+/- 10.0	0.1+/- 0.1	133.55	1.02	NS11	150
2008	128	5 34	13.0+/- 19.0	0.2+/- 0.0	175.41	2.18	NS09	111
2008	128	5 34	15.0+/- 14.0	0.2+/- 0.1	135.49	2.25	BB03	111
2008	144	20 46	29.0+/- 13.0	1.5+/- 0.1	350.12	4.57	NS11	100
2008	147	20 20	-65.0+/- 18.0	0.3+/- 0.1	16.31	3.86	NS05	208
2008	152	23 33	19.0+/- 17.0	0.3+/- 0.1	40.67	3.42	BB04	188
2008	152	23 33	-79.0+/- 20.0	0.4+/- 0.1	28.1	2.94	BB09	188
2008	163	20 35	42.0+/- 14.0	0.5+/- 0.1	52.73	1.7	BB10	189
2008	163	20 35	-13.0+/- 11.0	1.0+/- 0.1	22.06	1.8	BB11	189
2008	173	4 9	11.0+/- 14.0	1.2+/- 0.1	12.52	2.99	NS12	150
2008	174	12 12	-34.0+/- 16.0	0.3+/- 0.1	6.7	3.32	BB11	214
2008	177	0 26	67.0+/- 10.0	0.2+/- 0.0	169.59	1.61	NS15	116
2008	196	18 40	44.0+/- 17.0	0.2+/- 0.1	92.02	1.01	NS18	163
2008	198	13 26	28.0+/- 19.0	0.4+/- 0.1	118.11	1.12	NS13	156
2008	198	13 26	29.0+/- 13.0	0.2+/- 0.1	87.5	0.86	NS18	156
2008	198	13 26	-4.0+/- 14.0	0.1+/- 0.0	114.59	0.92	NS15	156
2008	198	13 26	-67.0+/- 10.0	0.2+/- 0.0	129.03	1.19	NS11	156
2008	198	13 26	-73.0+/- 9.0	0.3+/- 0.2	123.15	1.16	NS12	156
2008	218	23 38	-52.0+/- 16.0	0.9+/- 0.6	8.85	3.38	NS06	174
2008	220	7 44	48.0+/- 16.0	1.2+/- 0.1	5.91	2.58	EW10	164
2008	220	23 56	14.0+/- 18.0	0.4+/- 0.2	74.97	1.66	BB23	120

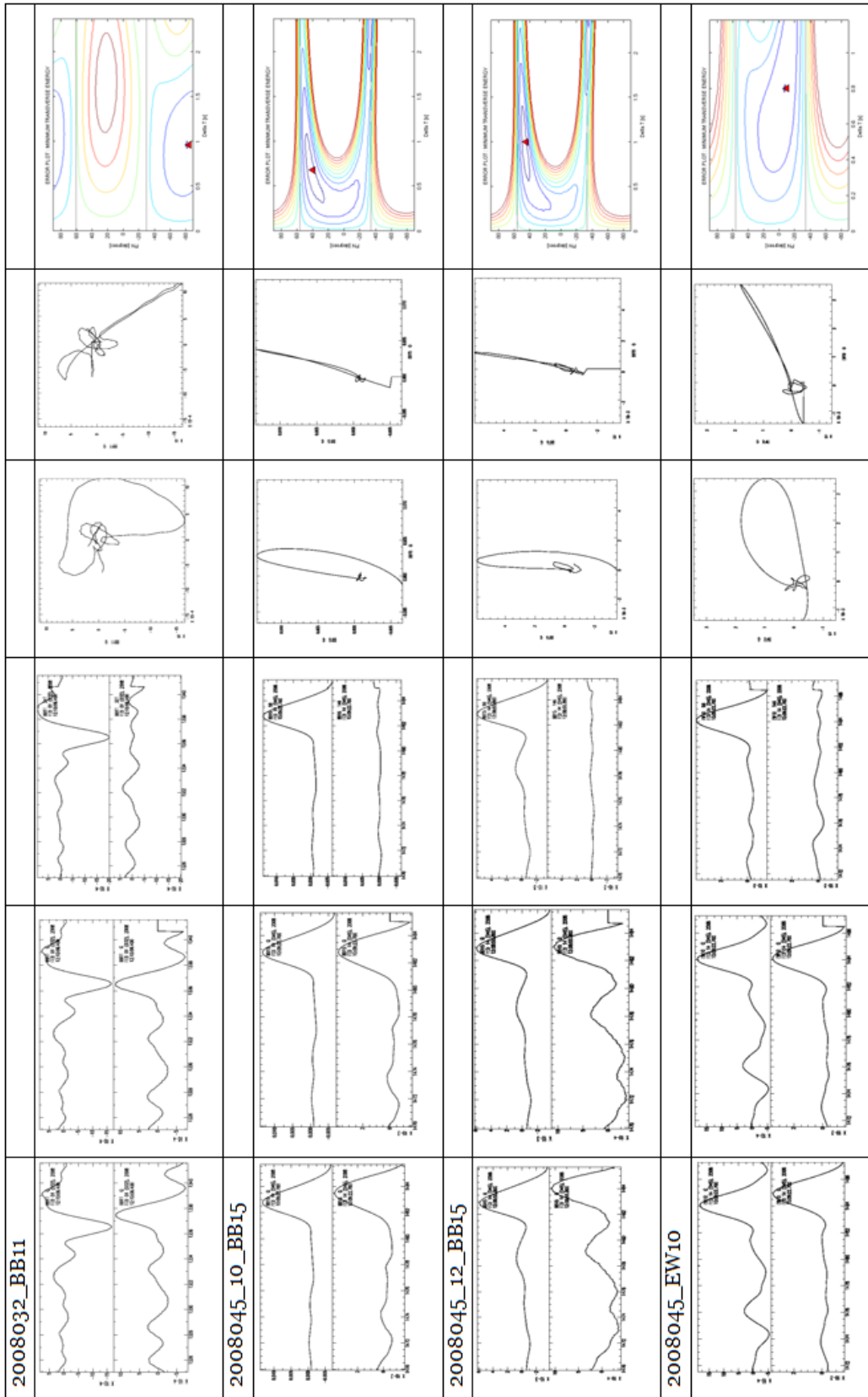
2008	234	9 32	-4.0+/- 14.0	0.2+/- 0.1	12.85	2.28	BB03	107
2008	246	17 27	4.0+/- 18.0	0.4+/- 0.1	158.04	0.64	NS14	138
2008	246	17 27	72.0+/- 14.0	0.2+/- 0.0	166.65	1.01	NS10	138
2008	246	17 27	-19.0+/- 14.0	0.2+/- 0.0	169.79	1.14	NS09	138
2008	247	11 25	8.0+/- 20.0	0.3+/- 0.1	84.12	4.07	NS12	569
2008	247	11 25	9.0+/- 15.0	0.3+/- 0.2	83.44	5.43	BB03	569
2008	247	11 25	-17.0+/- 9.0	1.2+/- 0.1	88.49	3.96	NS09	569
2008	249	20 51	-84.0+/- 15.0	1.0+/- 0.1	2.05	2.46	EW09	156
2008	250	17 57	86.0+/- 20.0	0.3+/- 0.1	2.28	2.5	EW09	161
2008	257	16 47	32.0+/- 17.0	0.4+/- 0.1	199.37	1.49	BB10	105
2008	257	16 47	33.0+/- 11.0	0.4+/- 0.0	114.01	0.98	BB03	105
2008	257	16 47	-23.0+/- 11.0	0.4+/- 0.1	208.57	1.11	NS09	105
2008	257	16 47	-41.0+/- 8.0	0.1+/- 0.0	260.27	1.48	BB13	105
2008	257	16 47	-74.0+/- 14.0	0.4+/- 0.0	248.84	1.05	BB12	105
2008	259	23 36	7.0+/- 19.0	0.4+/- 0.1	40.86	3.1	BB04	152
2008	259	23 36	85.0+/- 20.0	0.4+/- 0.1	26.87	2.63	BB09	152
2008	265	17 35	14.0+/- 15.0	0.6+/- 0.4	75.49	3.48	BB12	563
2008	265	17 35	84.0+/- 9.0	0.4+/- 0.1	89.15	3.4	EW09	563
2008	269	17 54	65.0+/- 18.0	0.4+/- 0.1	17.75	3.71	BB24	166
2008	315	10 56	15.0+/- 13.0	0.4+/- 0.0	43.81	3.19	BB04	169
2008	315	10 56	27.0+/- 14.0	0.6+/- 0.1	66.37	2.81	BB23	169
2008	315	10 56	42.0+/- 10.0	0.9+/- 0.2	20.77	3.85	BB24	169
2008	315	10 56	55.0+/- 19.0	0.6+/- 0.1	14.25	2.45	EW10	169
2008	315	10 56	-14.0+/- 13.0	0.6+/- 0.2	36.8	4.05	BB03	169
2008	315	10 56	-64.0+/- 13.0	0.4+/- 0.1	30.71	2.68	BB09	169
2008	326	13 17	84.0+/- 8.0	0.9+/- 0.1	3.47	2.55	EW09	181
2008	338	2 32	-87.0+/- 13.0	0.5+/- 0.1	7.77	2.66	EW10	162
2008	345	5 56	17.0+/- 16.0	0.4+/- 0.1	18.76	2.96	BB02	157
2008	348	0 35	28.0+/- 17.0	0.3+/- 0.0	89.69	1.2	BB24	164
2008	348	0 35	28.0+/- 18.0	0.4+/- 0.1	118.11	1.03	NS13	164
2008	348	0 35	-18.0+/- 16.0	0.2+/- 0.1	98.36	0.79	NS17	164
2008	348	0 35	-57.0+/- 13.0	0.2+/- 0.0	251.78	0.72	BB14	164
2008	354	1 56	-18.0+/- 14.0	0.2+/- 0.0	127	0.84	BB24	129
2008	354	15 21	41.0+/- 15.0	0.2+/- 0.0	96.09	0.67	NS18	147
2008	354	15 21	-72.0+/- 15.0	0.2+/- 0.0	217.15	0.41	BB13	147
2008	361	3 15	15.0+/- 11.0	0.3+/- 0.1	22.47	3.31	BB02	186
2008	361	3 15	52.0+/- 16.0	1.0+/- 0.2	18.62	3.99	BB24	186
2008	361	3 15	-75.0+/- 18.0	0.4+/- 0.1	14.47	2.55	NS05	186
2008	365	4 55	69.0+/- 17.0	0.6+/- 0.1	17.16	3.58	BB03	147
2009	3	21 15	16.0+/- 16.0	0.2+/- 0.1	106.62	3.29	BB13	627
2009	3	21 15	79.0+/- 16.0	0.9+/- 0.7	110.19	5.08	EW17	627
2009	3	21 15	-86.0+/- 12.0	1.4+/- 0.1	104.95	4.67	BB01	627
2009	15	21 31	33.0+/- 14.0	0.3+/- 0.2	48.08	0.81	NS11	131
2009	15	21 31	40.0+/- 17.0	0.2+/- 0.1	351.91	0.55	BB11	131
2009	19	23 31	-32.0+/- 20.0	0.5+/- 0.2	19.7	2.39	BB10	176
2009	64	6 4	-3.0+/- 24.0	0.4+/- 0.1	42.61	3.41	BB04	201

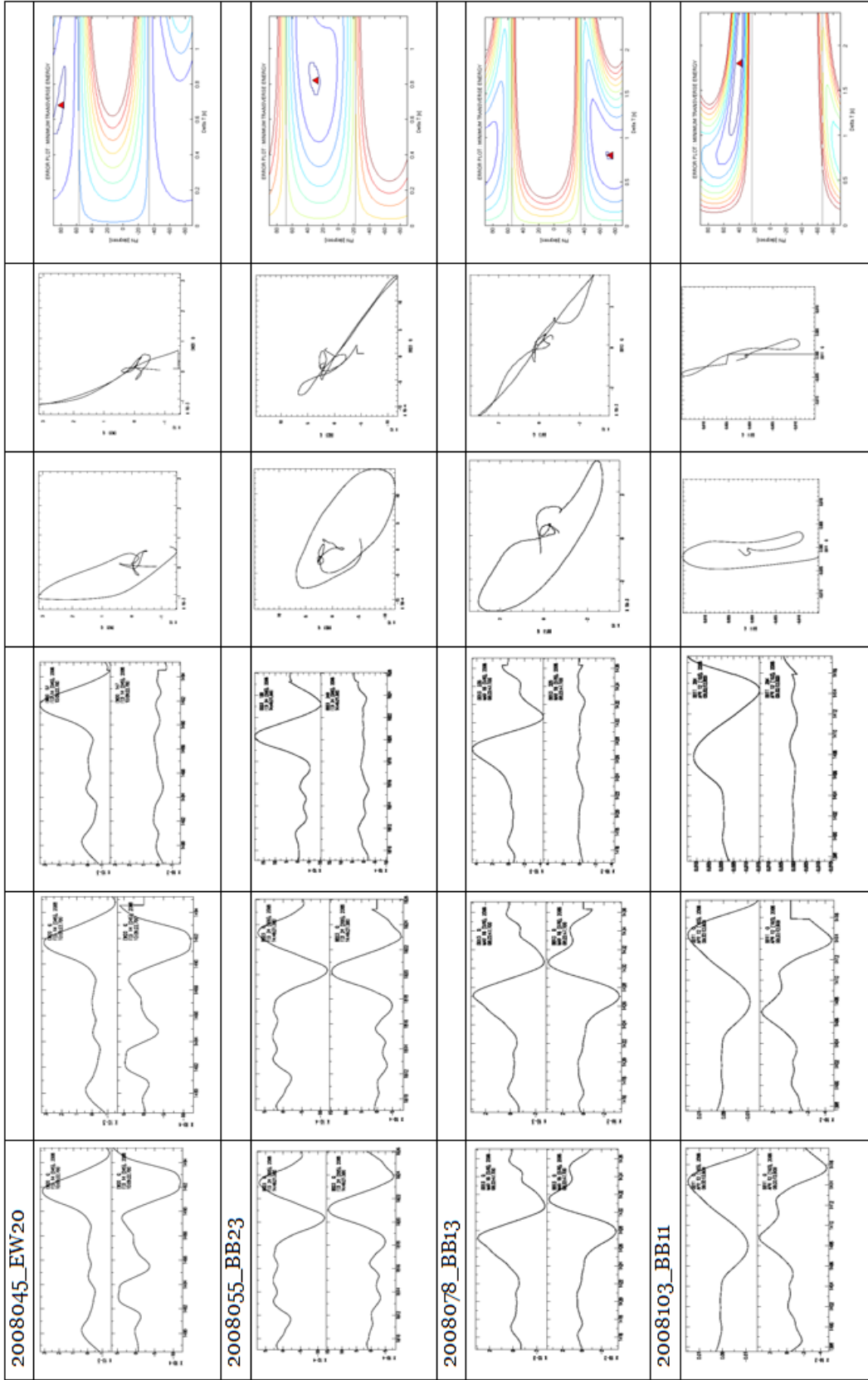
## Appendix D: Quality-control inspection of shear-wave splitting

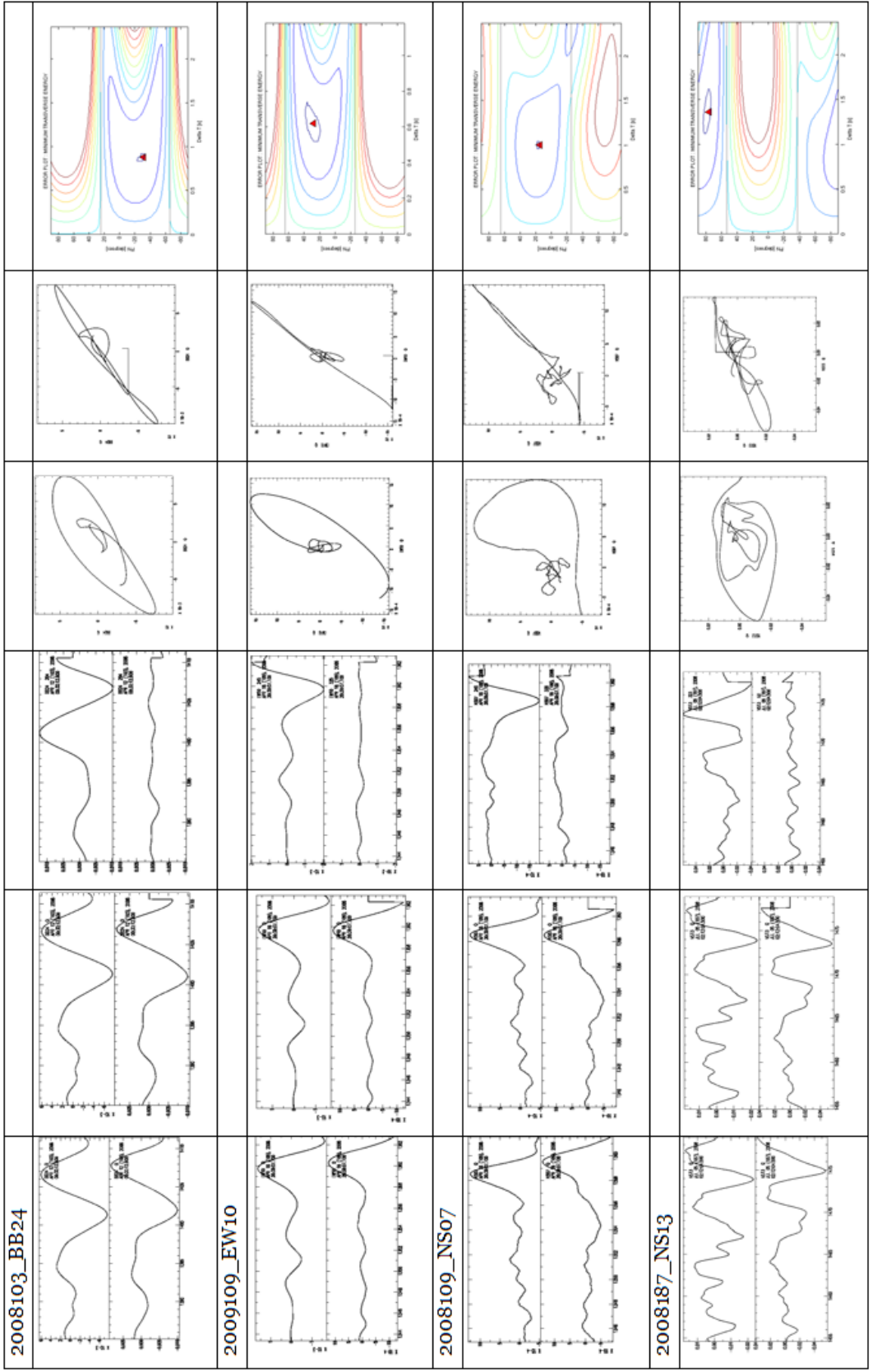
Quality-control check for teleseismic splitting events. All components of the quality-control check are shown. Only events considered to show true splitting behavior are shown. Events are identified by: year-julian day-station name.

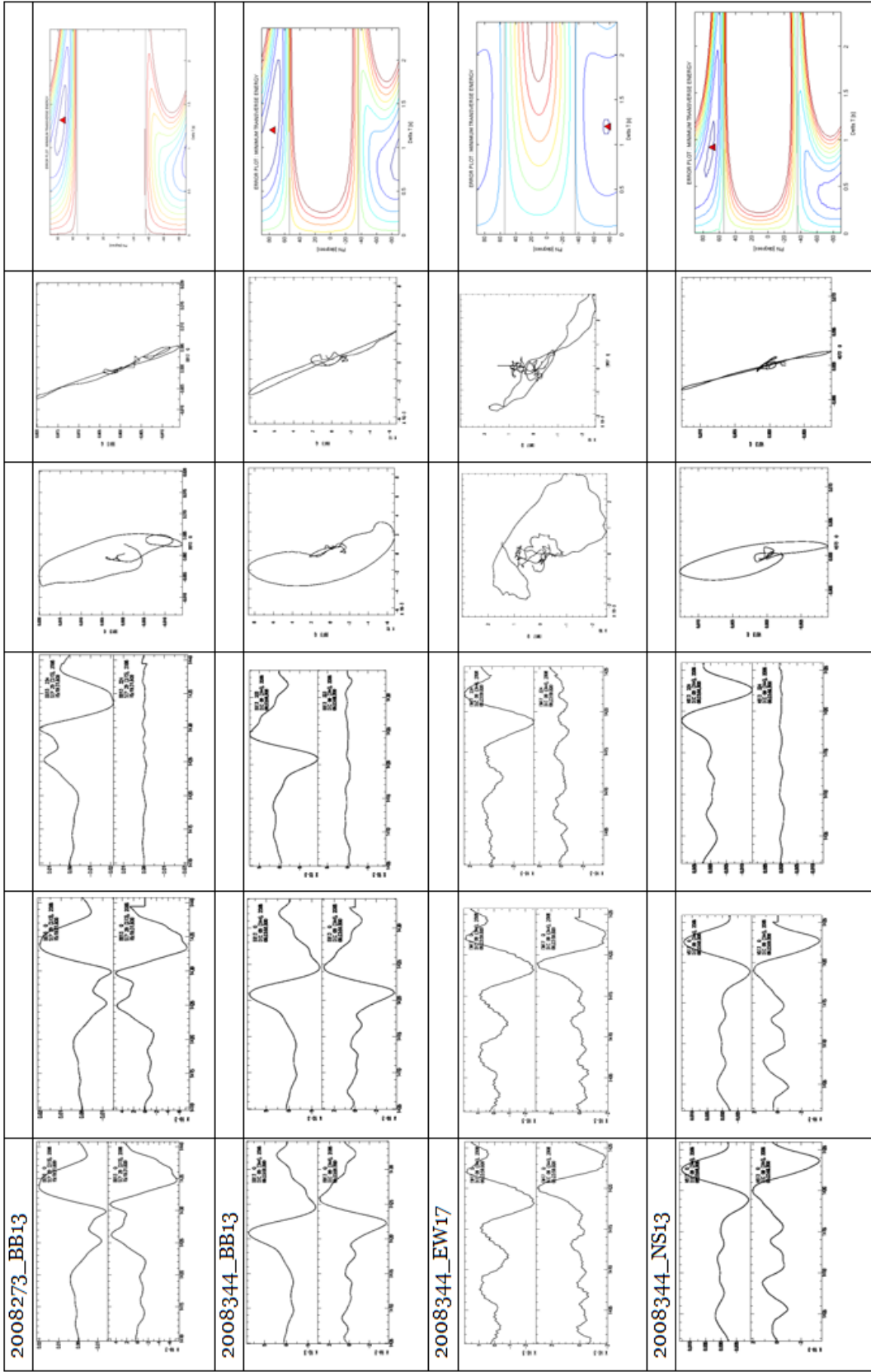


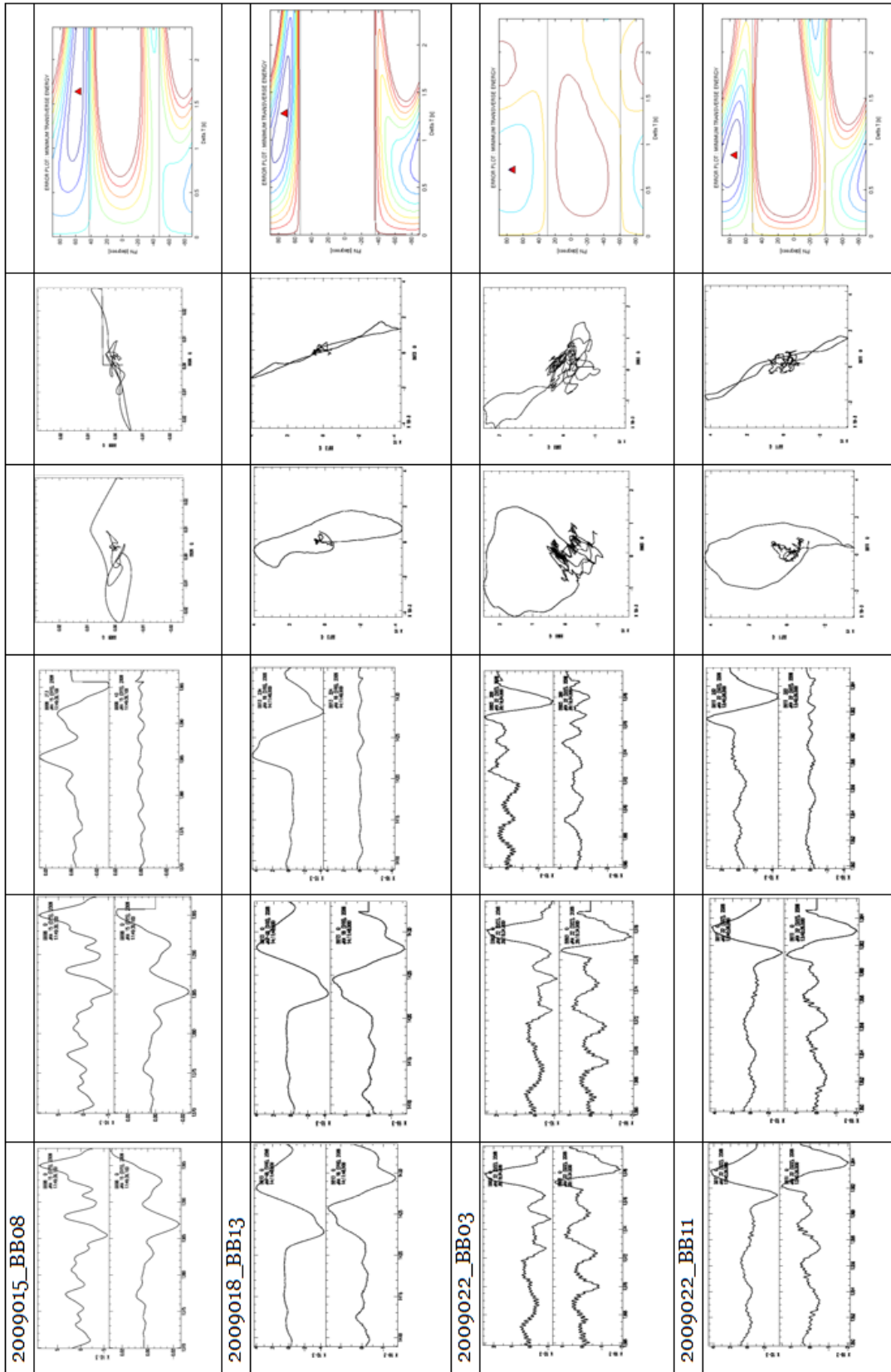


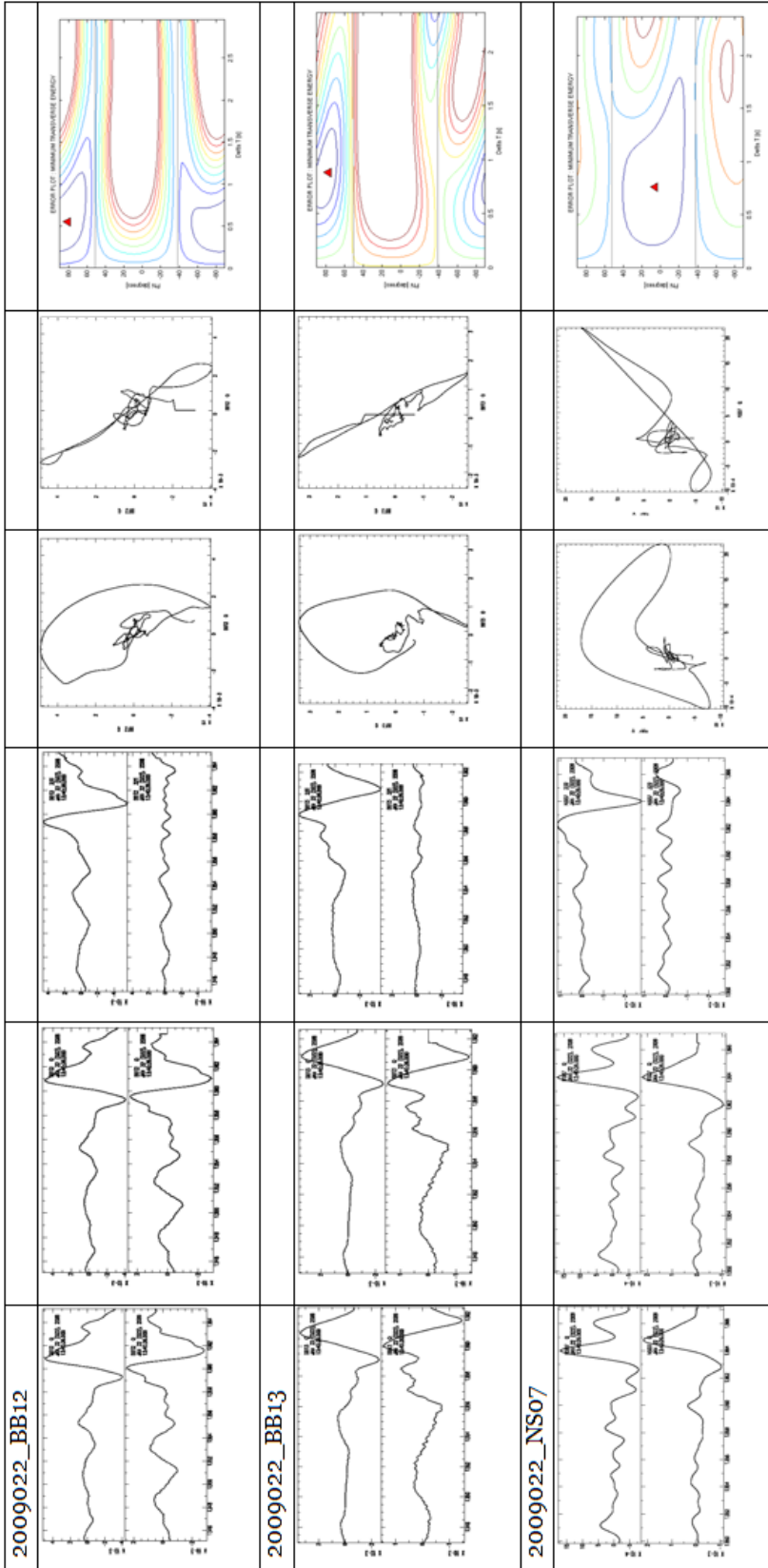




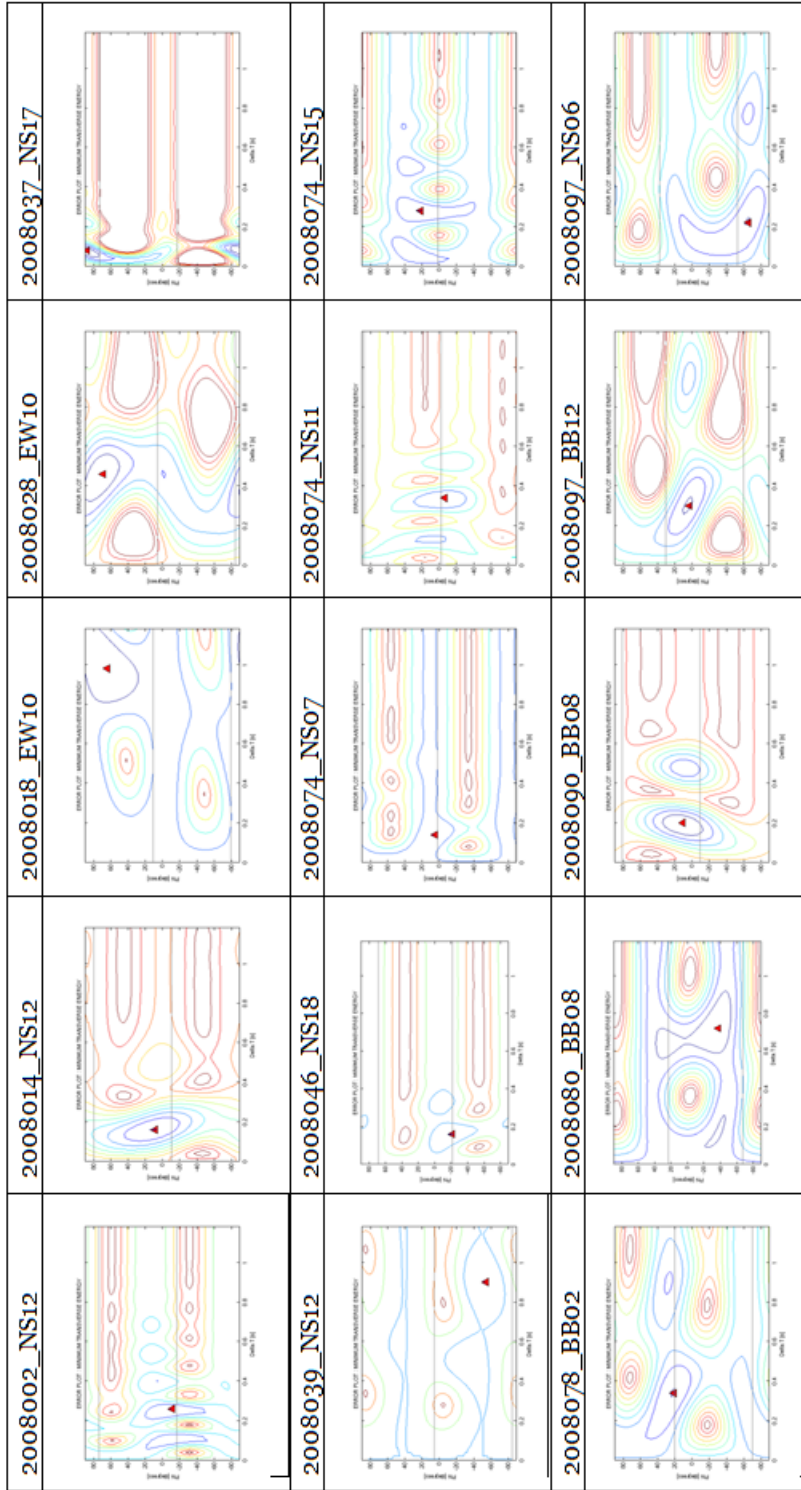


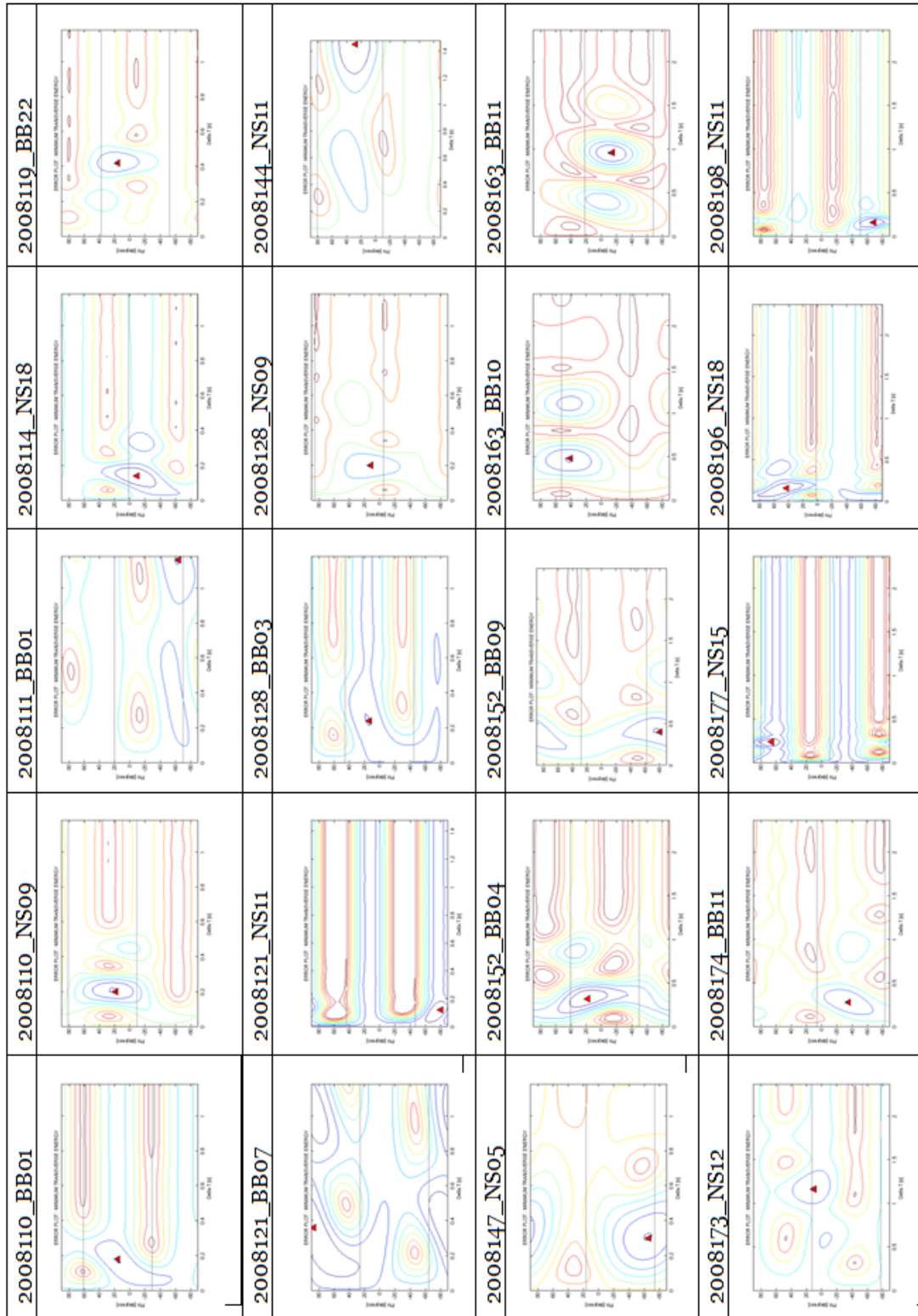


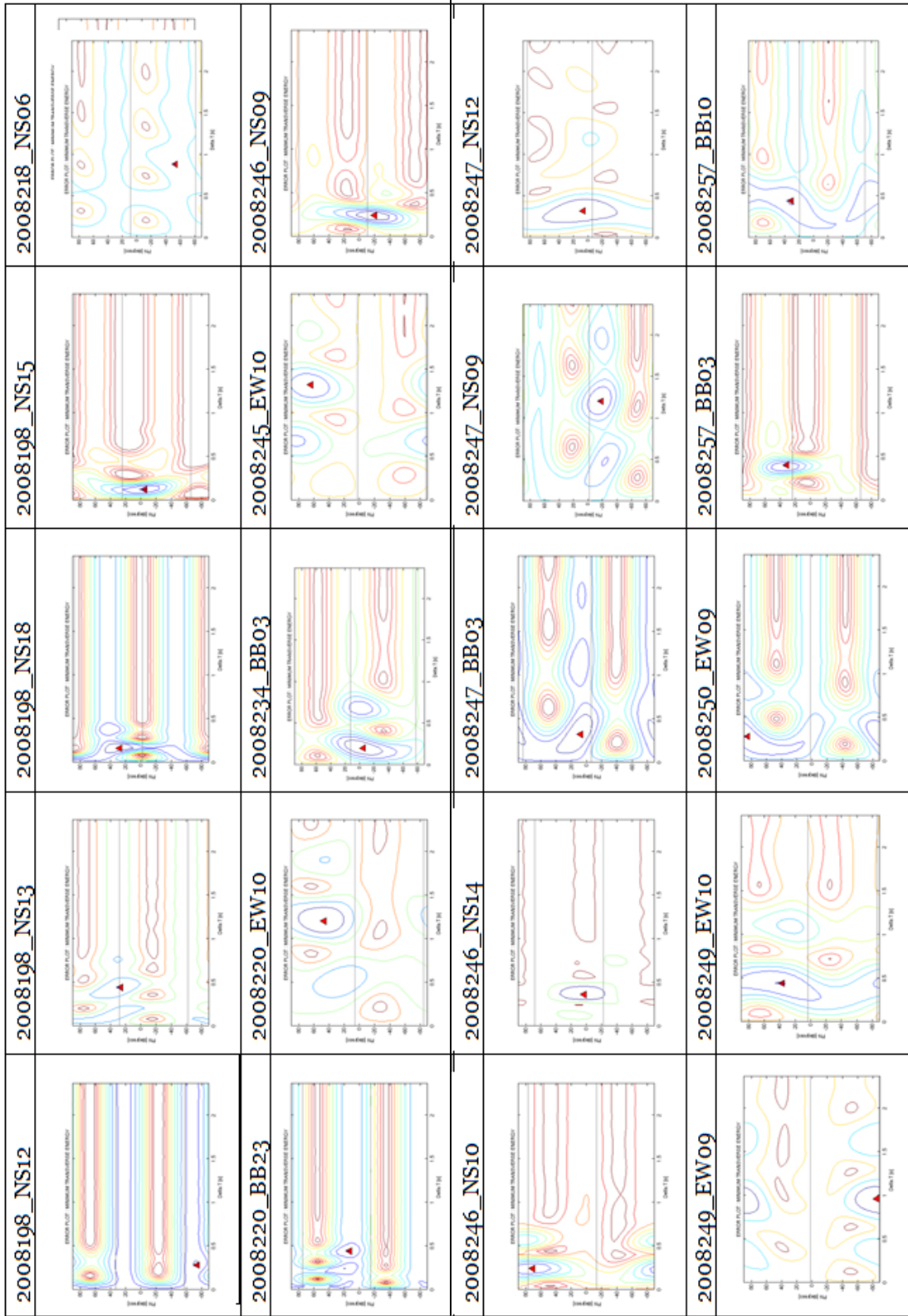


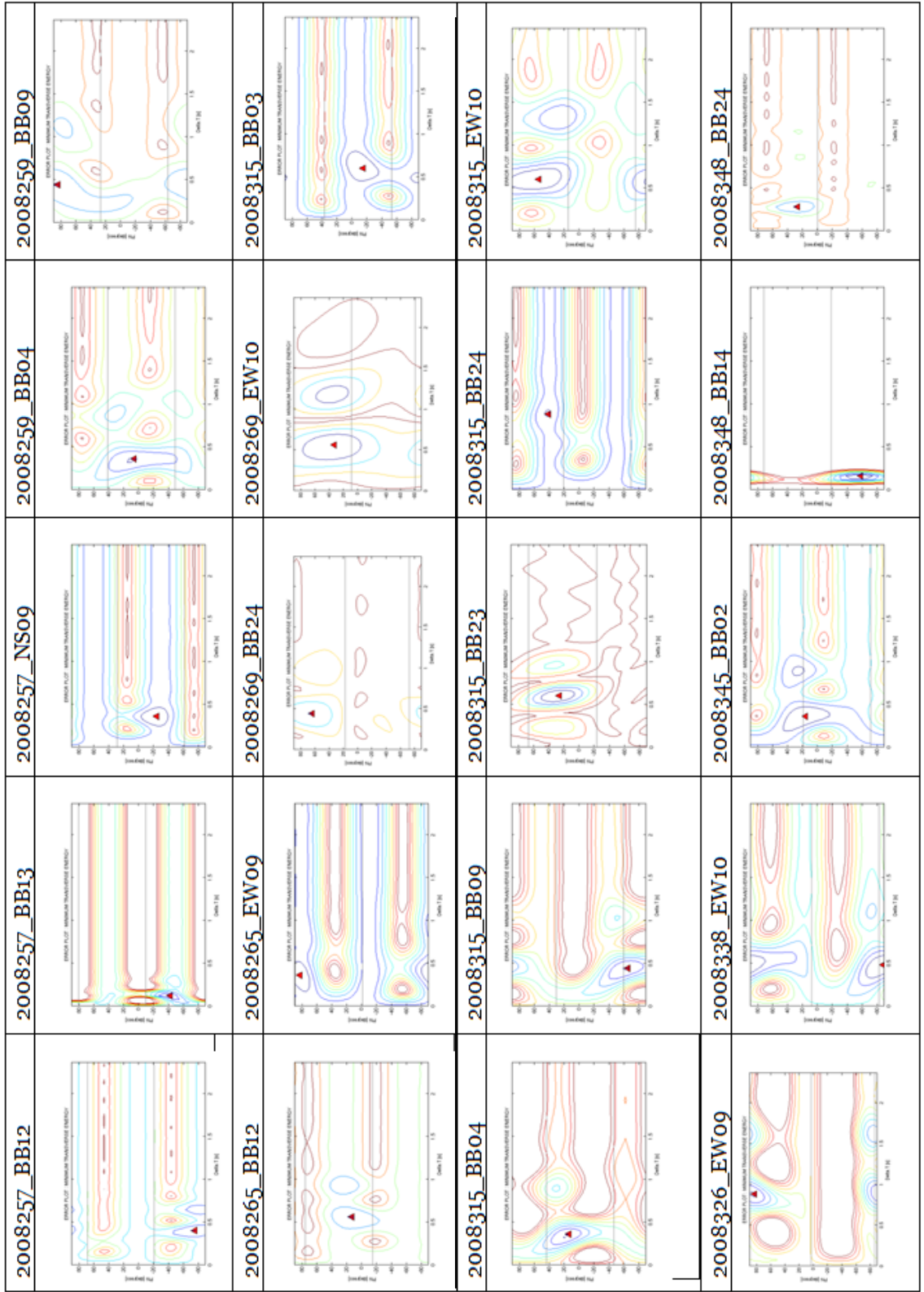


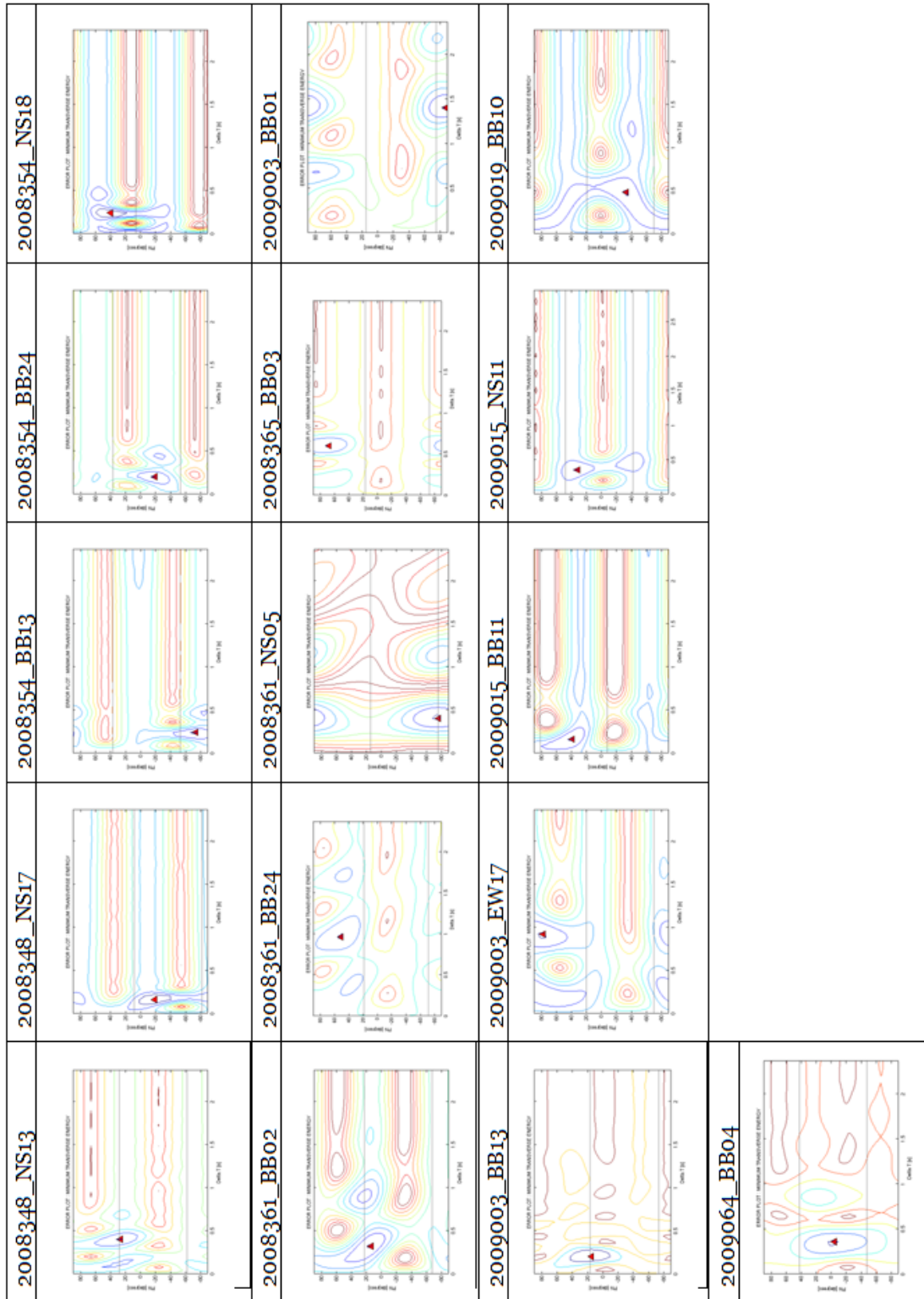
Error plots of local events used in this study. These events passed quality-control inspection to display shear-wave splitting behavior. Events are identified by: year-julian day-station name.





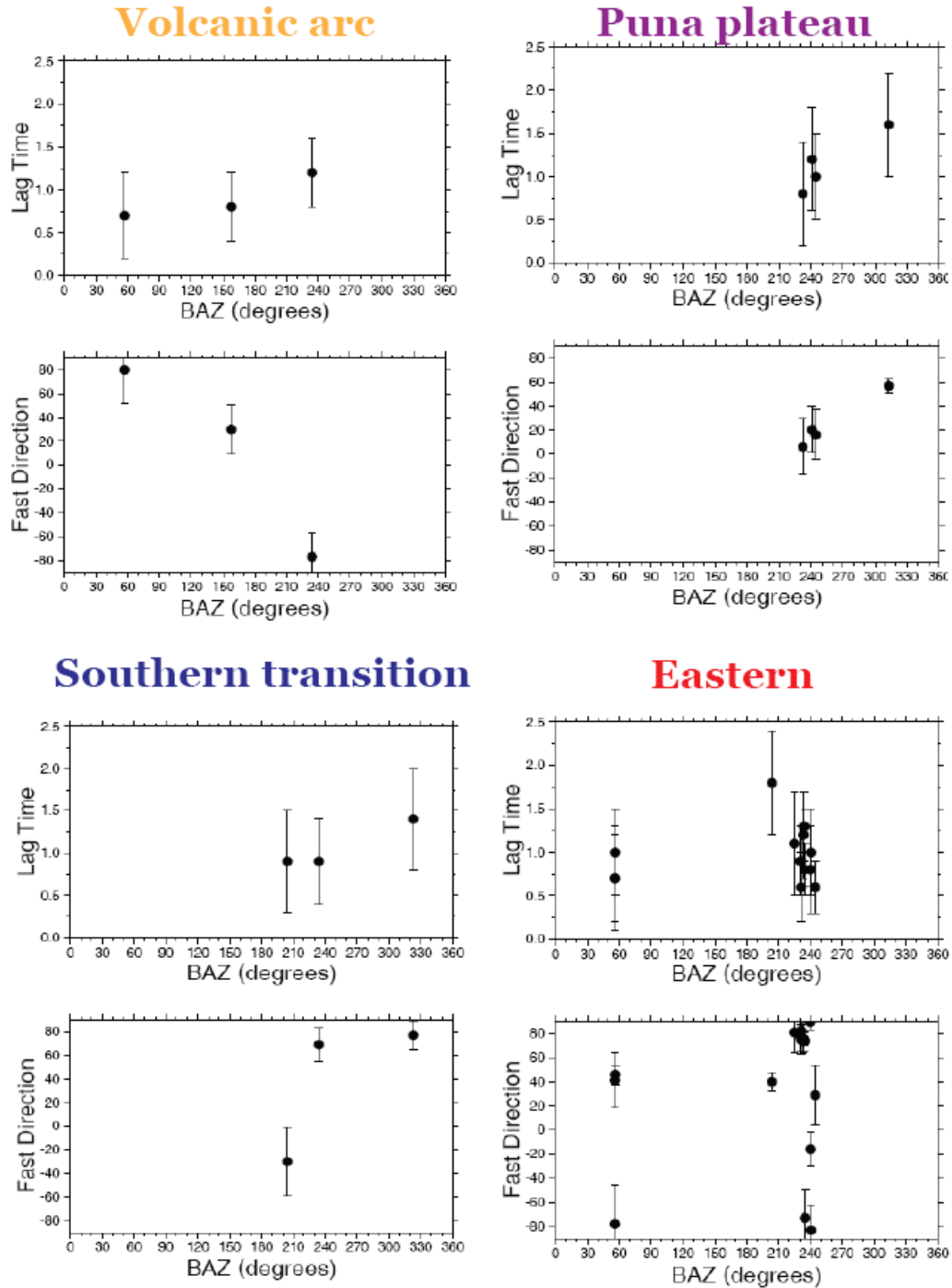






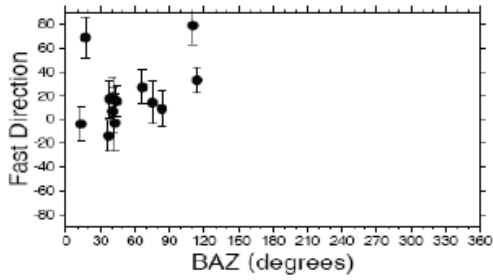
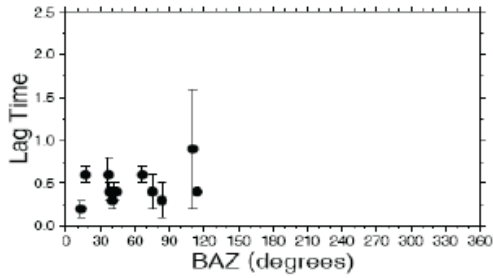
## Appendix E: Splitting versus BAZ.

Plots demonstrate teleseismic event back azimuths versus both the fast direction and the lag time of shear-wave splitting.

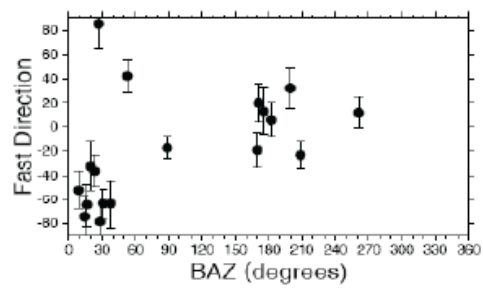
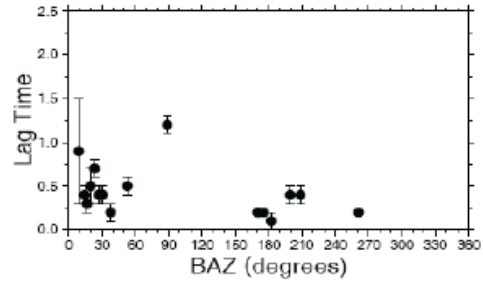


Plots demonstrate local event back azimuths versus both the fast direction and the lag time of shear-wave splitting.

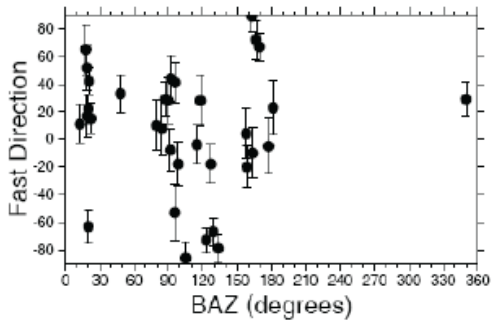
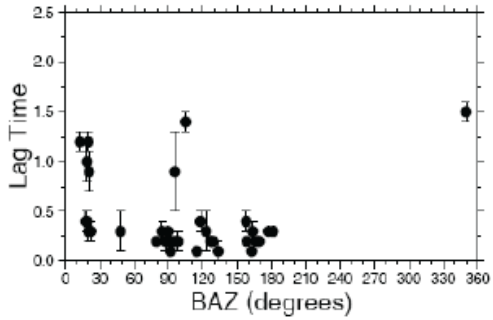
### Volcanic arc



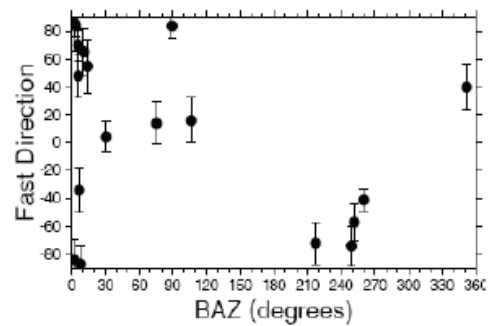
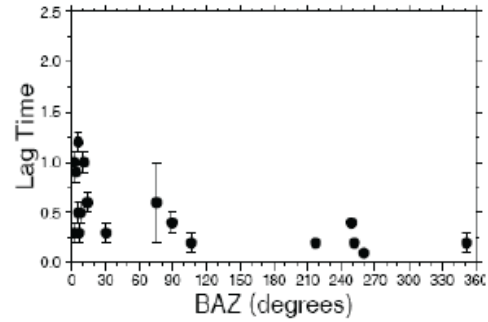
### Puna plateau



### Southern transition



### Eastern



## Appendix F: Stacking data

Teleseismic events used for the stacking procedure. Two sets of data are displayed in this table under the column labeled 'Quality.' 'Noisy' data was not used in the original splitting analysis. However, 'Good' data is considered to be high quality and was included in the analysis. The stacking procedure uses a weighted average method for both 'Noisy' and 'Good' data and also one for only 'Good' data.

Event Time	Fast Direction (°)	Lag Time (sec)	BAZ (°)	DELTA (°)	STA	QUALITY
7354 7 55	55.0+/- 36.0	1.5+/- 1.3	224.87	90.23	BB13	Noisy
<b>7354 7 55</b>	<b>81.0+/- 17.0</b>	<b>1.1+/- 0.6</b>	<b>225.03</b>	<b>90.38</b>	<b>BB11</b>	<b>Good</b>
8 1 18 54	-21.0+/- 15.0	1.6+/- 0.8	229.23	133.56	BB13	Noisy
<b>8 6 5 14</b>	<b>-78.0+/- 32.0</b>	<b>0.7+/- 0.6</b>	<b>56.12</b>	<b>105.94</b>	<b>BB12</b>	<b>Good</b>
<b>8 15 17 52</b>	<b>2.0+/- 27.0</b>	<b>0.8+/- 0.6</b>	<b>240.44</b>	<b>98.32</b>	<b>NS07</b>	<b>Good</b>
<b>8 15 17 52</b>	<b>89.0+/- 6.0</b>	<b>0.8+/- 0.2</b>	<b>240.07</b>	<b>98.57</b>	<b>BB11</b>	<b>Good</b>
<b>8 15 17 52</b>	<b>-11.0+/- 16.0</b>	<b>0.9+/- 0.4</b>	<b>240.66</b>	<b>97.69</b>	<b>BB02</b>	<b>Good</b>
8 15 17 52	-14.0+/- 33.0	0.6+/- 0.6	240.3	98.59	EW10	Noisy
<b>8 15 17 52</b>	<b>-16.0+/- 15.0</b>	<b>0.8+/- 0.5</b>	<b>240.25</b>	<b>98.6</b>	<b>EW09</b>	<b>Good</b>
8 15 17 52	-24.0+/- 4.0	1.2+/- 0.6	241.22	96.6	BB03	Noisy
8 30 7 32	-29.0+/- 18.0	1.3+/- 0.5	205.35	142.3	NS16	Noisy
8 32 12 10	1.0+/- 23.0	1.6+/- 0.9	240.95	98.45	NS07	Noisy
<b>8 32 12 10</b>	<b>20.0+/- 19.0</b>	<b>1.2+/- 0.6</b>	<b>241.04</b>	<b>98.43</b>	<b>BB10</b>	<b>Good</b>
<b>8 32 12 10</b>	<b>-83.0+/- 21.0</b>	<b>1.0+/- 0.5</b>	<b>240.57</b>	<b>98.7</b>	<b>BB11</b>	<b>Good</b>
<b>8 45 10 9</b>	<b>41.0+/- 23.0</b>	<b>0.7+/- 0.5</b>	<b>56.18</b>	<b>104.24</b>	<b>BB15</b>	<b>Good</b>
<b>8 45 10 9</b>	<b>-8.0+/- 24.0</b>	<b>0.8+/- 0.4</b>	<b>56.31</b>	<b>104.49</b>	<b>EW10</b>	<b>Good</b>
8 45 10 9	71.0+/- 42.0	1.9+/- 1.0	56.5	104.92	EW12	Noisy
<b>8 45 10 9</b>	<b>80.0+/- 28.0</b>	<b>0.7+/- 0.5</b>	<b>56.86</b>	<b>105.79</b>	<b>EW20</b>	<b>Good</b>
8 45 10 9	-18.0+/- 11.0	1.4+/- 0.6	56.57	105.11	EW14	Noisy
8 45 10 9	-23.0+/- 59.0	0.9+/- 0.8	56.69	105.39	BB02	Noisy
8 45 10 9	-27.0+/- 90.0	1.2+/- 0.7	57.15	106.47	BB03	Noisy
8 45 10 9	-28.0+/- 90.0	1.5+/- 1.1	56.42	104.75	NS07	Noisy
8 45 10 9	-8.0+/- 24.0	1.6+/- 0.8	56.5	104.89	NS08	Noisy
8 45 10 9	-45.0+/- 12.0	1.3+/- 0.9	56.6	105.28	NS13	Noisy
<b>8 45 12 8</b>	<b>46.0+/- 8.0</b>	<b>1.0+/- 0.5</b>	<b>56.39</b>	<b>104.33</b>	<b>BB15</b>	<b>Good</b>
8 45 12 8	79.0+/- 12.0	1.2+/- 0.4	56.4	104.25	BB07	Noisy
8 45 12 8	-10.0+/- 29.0	1.2+/- 1.0	56.9	105.54	BB23	Noisy
8 45 12 8	-19.0+/- 10.0	1.2+/- 0.6	57	105.71	EW18	Noisy
8 45 12 8	-19.0+/- 66.0	1.4+/- 1.2	56.8	105.19	NS11	Noisy
8 51 18 27	28.0+/- 27.0	1.6+/- 0.8	56.42	104.24	BB15	Noisy
<b>8 55 14 46</b>	<b>30.0+/- 21.0</b>	<b>0.8+/- 0.4</b>	<b>157.97</b>	<b>150.53</b>	<b>BB23</b>	<b>Good</b>
8 78 8 22	36.0+/- 35.0	0.7+/- 0.6	236.14	91.09	BB03	Noisy
8 78 8 22	62.0+/- 13.0	1.2+/- 0.9	235.44	93.41	BB07	Noisy

8 78 8 22	-30.0+/- 90.0	1.2+/- 0.6	235.23	93.06	EW10	Noisy
<b>8 78 8 22</b>	<b>-73.0+/- 24.0</b>	<b>0.8+/- 0.3</b>	<b>234.86</b>	<b>92.95</b>	<b>BB13</b>	<b>Good</b>
8 80 22 32	15.0+/- 27.0	1.1+/- 0.8	64.92	151.84	BB11	Noisy
8 82 21 24	74.0+/- 17.0	1.4+/- 1.0	316.3	123.64	NS11	Noisy
<b>8103 0 30</b>	<b>40.0+/- 8.0</b>	<b>1.8+/- 0.6</b>	<b>203.8</b>	<b>88.92</b>	<b>BB11</b>	<b>Good</b>
<b>8103 0 30</b>	<b>-30.0+/- 29.0</b>	<b>0.9+/- 0.6</b>	<b>204.31</b>	<b>87.85</b>	<b>BB24</b>	<b>Good</b>
8103 0 30	48.0+/- 16.0	1.4+/- 0.7	204.2	89.01	EW12	Noisy
8103 0 30	-43.0+/- 22.0	1.8+/- 0.8	204.25	88.9	EW14	Noisy
8103 0 30	-56.0+/- 82.0	1.2+/- 1.1	204.3	88.5	BB02	Noisy
8103 0 30	-62.0+/- 88.0	1.2+/- 0.8	203.93	89.28	EW10	Noisy
<b>8109 20 39</b>	<b>16.0+/- 21.0</b>	<b>1.0+/- 0.5</b>	<b>244.65</b>	<b>100.4</b>	<b>NS07</b>	<b>Good</b>
8109 20 39	-10.0+/- 15.0	1.5+/- 0.9	244.7	100.28	NS08	Noisy
<b>8109 20 39</b>	<b>29.0+/- 25.0</b>	<b>0.6+/- 0.3</b>	<b>244.51</b>	<b>100.67</b>	<b>EW10</b>	<b>Good</b>
8109 20 39	58.0+/- 11.0	1.5+/- 0.9	244.7	100.3	EW11	Noisy
8109 20 39	-19.0+/- 7.0	0.9+/- 0.5	245.4	98.68	BB03	Noisy
8109 20 39	-37.0+/- 90.0	1.9+/- 1.1	245.23	99.32	EW20	Noisy
8110 5 58	-85.0+/- 10.0	1.4+/- 0.4	235.17	108.42	EW10	Noisy
8123 1 33	65.0+/- 21.0	1.1+/- 0.7	316	122.89	NS11	Noisy
8146 8 21	-76.0+/- 20.0	1.6+/- 0.7	39.22	170.7	BB07	Noisy
8148 5 51	40.0+/- 30.0	1.3+/- 0.9	198.59	91.85	EW12	Noisy
8153 1 57	-19.0+/- 86.0	1.8+/- 1.5	238.38	168.52	BB04	Noisy
8185 3 2	-10.0+/- 17.0	1.4+/- 0.9	239.1	97.87	NS06	Noisy
8185 3 2	-18.0+/- 20.0	1.8+/- 1.2	239.19	97.31	NS12	Noisy
8185 3 2	-24.0+/- 90.0	1.9+/- 1.3	239.01	98.02	EW10	Noisy
<b>8187 2 12</b>	<b>77.0+/- 12.0</b>	<b>1.4+/- 0.6</b>	<b>322.99</b>	<b>140.14</b>	<b>NS13</b>	<b>Good</b>
8197 3 26	24.0+/- 23.0	1.2+/- 0.8	58.87	108.91	EW09	Noisy
8197 3 26	46.0+/- 24.0	1.4+/- 1.0	58.82	108.63	BB15	Noisy
8232 16 30	-6.0+/- 12.0	1.9+/- 1.0	249.4	96.87	NS08	Noisy
8232 16 30	78.0+/- 10.0	1.8+/- 1.0	248.78	97.44	BB13	Noisy
8243 6 54	-73.0+/- 31.0	1.0+/- 0.5	230.63	133.33	EW09	Noisy
8243 6 54	-83.0+/- 14.0	1.8+/- 0.6	231.21	132.92	EW12	Noisy
8273 15 19	49.0+/- 5.0	1.8+/- 1.1	234.82	92.15	NS16	Noisy
8273 15 19	71.0+/- 20.0	1.3+/- 1.1	235.62	91.76	BB22	Noisy
8273 15 19	71.0+/- 20.0	1.4+/- 1.0	235.34	91.78	EW19	Noisy
<b>8273 15 19</b>	<b>74.0+/- 4.0</b>	<b>1.3+/- 0.2</b>	<b>234.33</b>	<b>92.85</b>	<b>BB13</b>	<b>Good</b>
8273 15 19	-30.0+/- 10.0	1.4+/- 1.0	235.02	92.82	BB08	Noisy
8273 15 19	-30.0+/- 56.0	1.7+/- 1.6	235.06	92.07	BB02	Noisy
8279 9 12	63.0+/- 28.0	1.2+/- 1.2	234.54	92.36	EW10	Noisy
8279 9 12	-24.0+/- 14.0	1.8+/- 1.0	234.96	91.61	EW15	Noisy
8292 0 54	4.0+/- 22.0	0.9+/- 0.5	230.32	132.43	EW11	Noisy
8293 5 10	72.0+/- 15.0	1.8+/- 1.2	244.05	92.75	BB04	Noisy
8293 5 10	-17.0+/- 14.0	1.6+/- 0.9	243.31	93.98	NS06	Noisy
8296 12 55	2.0+/- 19.0	1.7+/- 0.8	245.6	96.74	NS08	Noisy
8296 12 55	-18.0+/- 88.0	1.5+/- 1.2	245.72	95.95	BB24	Noisy
8296 12 55	-34.0+/- 75.0	1.4+/- 1.3	246.29	95.72	BB04	Noisy
8297 10 4	2.0+/- 8.0	1.7+/- 0.4	231.79	136.91	BB11	Noisy
8341 10 55	73.0+/- 34.0	0.8+/- 0.6	204.04	143.99	BB22	Noisy
8344 6 23	63.0+/- 8.0	1.8+/- 0.9	234	91	NS11	Noisy
<b>8344 6 23</b>	<b>69.0+/- 14.0</b>	<b>0.9+/- 0.5</b>	<b>234.03</b>	<b>90.82</b>	<b>NS13</b>	<b>Good</b>

---

8344 6 23	69.0+/- 22.0	1.0+/- 0.9	233.73	91.17	BB12	Noisy
<b>8344 6 23</b>	<b>76.0+/- 12.0</b>	<b>1.2+/- 0.5</b>	<b>233.47</b>	<b>91.48</b>	<b>BB13</b>	<b>Good</b>
8344 6 23	-44.0+/- 50.0	1.8+/- 1.5	233.99	91.28	EW11	Noisy
8344 6 23	-45.0+/- 23.0	1.0+/- 0.8	233.95	90.8	NS16	Noisy
<b>8344 6 23</b>	<b>-81.0+/- 23.0</b>	<b>1.2+/- 0.6</b>	<b>234.33</b>	<b>90.61</b>	<b>EW17</b>	<b>Good</b>
8346 21 40	43.0+/- 48.0	1.3+/- 1.1	206.46	151.07	BB04	Noisy
8348 8 45	15.0+/- 66.0	1.8+/- 1.6	186.75	103.2	BB13	Noisy
<b>9 15 17 49</b>	<b>57.0+/- 6.0</b>	<b>1.6+/- 0.6</b>	<b>312.92</b>	<b>140.21</b>	<b>BB08</b>	<b>Good</b>
9 15 17 49	74.0+/- 17.0	1.2+/- 0.8	312	141.09	NS11	Noisy
9 18 14 11	66.0+/- 25.0	1.3+/- 1.0	233.73	93.13	BB15	Noisy
9 18 14 11	67.0+/- 24.0	1.7+/- 1.3	234.38	92.3	NS11	Noisy
<b>9 18 14 11</b>	<b>73.0+/- 8.0</b>	<b>1.3+/- 0.4</b>	<b>233.83</b>	<b>92.79</b>	<b>BB13</b>	<b>Good</b>
9 18 14 11	-20.0+/- 33.0	1.4+/- 1.0	234.37	92.53	NS08	Noisy
9 18 14 11	-56.0+/- 28.0	1.0+/- 0.8	234.02	92.85	BB11	Noisy
<b>9 22 13 40</b>	<b>7.0+/- 24.0</b>	<b>0.8+/- 0.6</b>	<b>232.43</b>	<b>132.37</b>	<b>NS07</b>	<b>Good</b>
9 22 13 40	67.0+/- 47.0	1.4+/- 1.0	232.74	132.15	EW13	Noisy
9 22 13 40	70.0+/- 35.0	1.1+/- 1.0	231.84	131.77	NS16	Noisy
<b>9 22 13 40</b>	<b>75.0+/- 12.0</b>	<b>0.9+/- 0.4</b>	<b>231.53</b>	<b>132.52</b>	<b>BB11</b>	<b>Good</b>
<b>9 22 13 40</b>	<b>78.0+/- 13.0</b>	<b>0.9+/- 0.4</b>	<b>230.82</b>	<b>132.43</b>	<b>BB13</b>	<b>Good</b>
9 22 13 40	-8.0+/- 18.0	1.0+/- 0.7	232.4	132.57	NS05	Noisy
<b>9 22 13 40</b>	<b>82.0+/- 17.0</b>	<b>0.6+/- 0.4</b>	<b>231.44</b>	<b>132.14</b>	<b>BB12</b>	<b>Good</b>
9 22 13 40	-32.0+/- 88.0	1.3+/- 1.1	232.45	131.49	BB01	Noisy
<b>9 22 20 16</b>	<b>74.0+/- 23.0</b>	<b>0.7+/- 0.4</b>	<b>209.09</b>	<b>141.35</b>	<b>BB03</b>	<b>Good</b>
9 42 17 34	-67.0+/- 81.0	1.4+/- 1.3	212.13	153.87	EW09	Noisy
9 49 21 53	50.0+/- 9.0	1.9+/- 1.1	237.62	93.02	BB08	Noisy
9 49 21 53	65.0+/- 8.0	1.9+/- 1.1	237.46	92.75	NS09	Noisy
9 49 21 53	-20.0+/- 67.0	1.4+/- 1.1	237.53	92.78	EW12	Noisy
9 49 21 53	-28.0+/- 89.0	1.8+/- 1.1	237.29	93.21	EW10	Noisy
9 52 0 12	-49.0+/- 16.0	1.4+/- 0.7	281.51	163.49	NS08	Noisy

---

Local events used for the stacking procedure. Two sets of data are displayed in this table under the column labeled 'Quality.' 'Noisy' data was not used in the original splitting analysis. However, 'Good' data is considered to be high quality and was included in the analysis. The stacking procedure uses an weighted average method for both 'Noisy' and 'Good' data and also one for only 'Good' data. All stacking data was distributed into one of three depth categories. A shallow category was assigned for earthquakes occurring at a depth of 0 to 200 km, an intermediate for 200 to 300 km depth, and deep for an origin of greater than 300 km depth.

Event Time	Fast Direction (°)	Lag Time (sec)	BAZ (°)	Delta (km)	STA	Depth (km)	Quality
<b>Shallow (0-200 km)</b>							
<b>8 2 12 17</b>	<b>-10.0+/- 18.0</b>	<b>0.3+/- 0.1</b>	<b>163.49</b>	<b>1.03</b>	<b>NS12</b>	<b>123</b>	<b>Good</b>
8 2 12 17	-16.0+/- 17.0	0.5+/- 0.1	123.1	0.71	BB24	123	Noisy
8 9 0 51	18.0+/- 12.0	0.5+/- 0.4	34.81	3.01	BB04	163	Noisy
8 14 6 4	5.0+/- 29.0	0.3+/- 0.2	56.52	1.25	NS17	169	Noisy
8 14 6 4	42.0+/- 23.0	0.4+/- 0.1	347.05	0.34	BB15	169	Noisy
8 14 6 4	-27.0+/- 23.0	0.6+/- 0.1	116.66	0.73	EW09	169	Noisy
8 14 6 4	-70.0+/- 19.0	0.5+/- 0.4	61.07	1.67	BB24	169	Noisy
<b>8 18 21 33</b>	<b>65.0+/- 17.0</b>	<b>1.0+/- 0.1</b>	<b>10.79</b>	<b>3.02</b>	<b>EW10</b>	<b>191</b>	<b>Good</b>
8 22 15 50	71.0+/- 24.0	1.2+/- 0.1	8.66	2.51	EW10	184	Noisy
8 22 15 50	-44.0+/- 37.0	0.3+/- 0.1	1.67	3	BB11	184	Noisy
8 28 11 57	37.0+/- 17.0	1.2+/- 0.6	12.55	3.31	NS13	170	Noisy
<b>8 28 11 57</b>	<b>70.0+/- 11.0</b>	<b>0.5+/- 0.1</b>	<b>5.76</b>	<b>2.51</b>	<b>EW10</b>	<b>170</b>	<b>Good</b>
8 28 11 57	-36.0+/- 90.0	0.3+/- 0.2	8.79	3.84	NS18	170	Noisy
8 28 11 57	-64.0+/- 21.0	0.7+/- 0.1	9.38	3.51	NS16	170	Noisy
8 37 9 51	14.0+/- 19.0	0.3+/- 0.1	153.78	1.38	BB02	124	Noisy
8 37 9 51	77.0+/- 67.0	0.3+/- 0.2	129.98	0.8	BB24	124	Noisy
8 37 9 51	90.0+/- 13.0	0.3+/- 0.1	164.27	1.16	NS12	124	Noisy
8 37 9 51	-64.0+/- 11.0	0.3+/- 0.0	144.62	1.13	BB01	124	Noisy
8 46 21 16	-88.0+/- 30.0	0.4+/- 0.1	188.78	1.69	BB11	133	Noisy
<b>8 74 6 55</b>	<b>23.0+/- 20.0</b>	<b>0.3+/- 0.0</b>	<b>181.44</b>	<b>1.01</b>	<b>NS15</b>	<b>103</b>	<b>Good</b>
<b>8 74 6 55</b>	<b>-5.0+/- 20.0</b>	<b>0.3+/- 0.0</b>	<b>177.4</b>	<b>1.38</b>	<b>NS11</b>	<b>103</b>	<b>Good</b>
8 74 6 55	-20.0+/- 24.0	0.4+/- 0.0	180.26	0.59	NS18	103	Noisy
<b>8 78 0 46</b>	<b>22.0+/- 11.0</b>	<b>0.3+/- 0.1</b>	<b>19.98</b>	<b>3.02</b>	<b>BB02</b>	<b>159</b>	<b>Good</b>
<b>8 80 1 21</b>	<b>-36.0+/- 13.0</b>	<b>0.7+/- 0.1</b>	<b>23.17</b>	<b>1.98</b>	<b>BB08</b>	<b>167</b>	<b>Good</b>
8111 5 36	-40.0+/- 13.0	0.3+/- 0.2	8.82	2.41	EW10	161	Noisy
<b>8111 5 36</b>	<b>-63.0+/- 12.0</b>	<b>1.2+/- 0.1</b>	<b>20.13</b>	<b>3.42</b>	<b>BB01</b>	<b>161</b>	<b>Good</b>
<b>8121 11 14</b>	<b>88.0+/- 20.0</b>	<b>0.4+/- 0.1</b>	<b>25.56</b>	<b>2.14</b>	<b>BB07</b>	<b>199</b>	<b>Good</b>
8121 16 43	5.0+/- 17.0	0.3+/- 0.1	159.91	1.39	NS05	150	Noisy
8132 2 24	59.0+/- 29.0	0.5+/- 0.1	18.03	3.94	BB24	192	Noisy
8139 10 59	9.0+/- 75.0	0.4+/- 0.1	358.06	3.56	BB13	179	Noisy
8139 10 59	36.0+/- 30.0	0.3+/- 0.2	10.97	2.56	EW10	179	Noisy
<b>8144 20 46</b>	<b>29.0+/- 13.0</b>	<b>1.5+/- 0.1</b>	<b>350.12</b>	<b>4.57</b>	<b>NS11</b>	<b>100</b>	<b>Good</b>
8152 23 33	11.0+/- 31.0	0.3+/- 0.2	16.12	2.69	NS05	188	Noisy
<b>8152 23 33</b>	<b>19.0+/- 17.0</b>	<b>0.3+/- 0.1</b>	<b>40.67</b>	<b>3.42</b>	<b>BB04</b>	<b>188</b>	<b>Good</b>
<b>8152 23 33</b>	<b>-79.0+/- 20.0</b>	<b>0.4+/- 0.1</b>	<b>28.1</b>	<b>2.94</b>	<b>BB09</b>	<b>188</b>	<b>Good</b>
<b>8163 20 35</b>	<b>42.0+/- 14.0</b>	<b>0.5+/- 0.1</b>	<b>52.73</b>	<b>1.7</b>	<b>BB10</b>	<b>189</b>	<b>Good</b>

<b>8163 20 35</b>	<b>-13.0+/- 11.0</b>	<b>1.0+/- 0.1</b>	<b>22.06</b>	<b>1.8</b>	<b>BB11</b>	<b>189</b>	<b>Good</b>
<b>8173 4 9</b>	<b>11.0+/- 14.0</b>	<b>1.2+/- 0.1</b>	<b>12.52</b>	<b>2.99</b>	<b>NS12</b>	<b>150</b>	<b>Good</b>
8198 13 26	1.0+/- 21.0	0.3+/- 0.1	122.56	2.48	BB04	156	Noisy
<b>8198 13 26</b>	<b>28.0+/- 19.0</b>	<b>0.4+/- 0.1</b>	<b>118.11</b>	<b>1.12</b>	<b>NS13</b>	<b>156</b>	<b>Good</b>
<b>8198 13 26</b>	<b>-73.0+/- 9.0</b>	<b>0.3+/- 0.2</b>	<b>123.15</b>	<b>1.16</b>	<b>NS12</b>	<b>156</b>	<b>Good</b>
8216 15 44	57.0+/- 16.0	1.3+/- 0.1	5.36	2.35	EW10	166	Noisy
<b>8218 23 38</b>	<b>-52.0+/- 16.0</b>	<b>0.9+/- 0.6</b>	<b>8.85</b>	<b>3.38</b>	<b>NS06</b>	<b>174</b>	<b>Good</b>
<b>8220 7 44</b>	<b>48.0+/- 16.0</b>	<b>1.2+/- 0.1</b>	<b>5.91</b>	<b>2.58</b>	<b>EW10</b>	<b>164</b>	<b>Good</b>
<b>8220 23 56</b>	<b>14.0+/- 18.0</b>	<b>0.4+/- 0.2</b>	<b>74.97</b>	<b>1.66</b>	<b>BB23</b>	<b>120</b>	<b>Good</b>
8245 13 38	65.0+/- 15.0	1.3+/- 0.1	2.53	2.48	EW10	165	Noisy
<b>8246 17 27</b>	<b>4.0+/- 18.0</b>	<b>0.4+/- 0.1</b>	<b>158.04</b>	<b>0.64</b>	<b>NS14</b>	<b>138</b>	<b>Good</b>
8249 20 51	38.0+/- 27.0	0.4+/- 0.1	3.85	2.37	EW10	156	Noisy
<b>8249 20 51</b>	<b>-84.0+/- 15.0</b>	<b>1.0+/- 0.1</b>	<b>2.05</b>	<b>2.46</b>	<b>EW09</b>	<b>156</b>	<b>Good</b>
8250 14 15	33.0+/- 15.0	0.3+/- 0.2	78.4	0.72	NS18	154	Noisy
<b>8250 17 57</b>	<b>86.0+/- 20.0</b>	<b>0.3+/- 0.1</b>	<b>2.28</b>	<b>2.5</b>	<b>EW09</b>	<b>161</b>	<b>Good</b>
<b>8257 16 47</b>	<b>32.0+/- 17.0</b>	<b>0.4+/- 0.1</b>	<b>199.37</b>	<b>1.49</b>	<b>BB10</b>	<b>105</b>	<b>Good</b>
<b>8257 16 47</b>	<b>33.0+/- 11.0</b>	<b>0.4+/- 0.0</b>	<b>114.01</b>	<b>0.98</b>	<b>BB03</b>	<b>105</b>	<b>Good</b>
<b>8257 16 47</b>	<b>-23.0+/- 11.0</b>	<b>0.4+/- 0.1</b>	<b>208.57</b>	<b>1.11</b>	<b>NS09</b>	<b>105</b>	<b>Good</b>
<b>8257 16 47</b>	<b>-74.0+/- 14.0</b>	<b>0.4+/- 0.0</b>	<b>248.84</b>	<b>1.05</b>	<b>BB12</b>	<b>105</b>	<b>Good</b>
<b>8259 23 36</b>	<b>7.0+/- 19.0</b>	<b>0.4+/- 0.1</b>	<b>40.86</b>	<b>3.1</b>	<b>BB04</b>	<b>152</b>	<b>Good</b>
8259 23 36	32.0+/- 17.0	0.3+/- 0.1	48.62	2.97	BB22	152	Noisy
<b>8259 23 36</b>	<b>85.0+/- 20.0</b>	<b>0.4+/- 0.1</b>	<b>26.87</b>	<b>2.63</b>	<b>BB09</b>	<b>152</b>	<b>Good</b>
8269 17 54	34.0+/- 22.0	0.6+/- 0.1	9.05	2.33	EW10	166	Noisy
<b>8269 17 54</b>	<b>65.0+/- 18.0</b>	<b>0.4+/- 0.1</b>	<b>17.75</b>	<b>3.71</b>	<b>BB24</b>	<b>166</b>	<b>Good</b>
8270 2 21	-15.0+/- 36.0	0.4+/- 0.2	169.34	1.5	NS10	128	Noisy
8277 16 2	-48.0+/- 17.0	0.3+/- 0.2	25.49	2.92	BB08	174	Noisy
8301 19 8	-25.0+/- 24.0	0.6+/- 0.1	263.03	1.1	BB02	113	Noisy
8315 10 56	3.0+/- 30.0	0.4+/- 0.1	23.84	2.47	BB10	169	Noisy
<b>8315 10 56</b>	<b>15.0+/- 13.0</b>	<b>0.4+/- 0.0</b>	<b>43.81</b>	<b>3.19</b>	<b>BB04</b>	<b>169</b>	<b>Good</b>
<b>8315 10 56</b>	<b>27.0+/- 14.0</b>	<b>0.6+/- 0.1</b>	<b>66.37</b>	<b>2.81</b>	<b>BB23</b>	<b>169</b>	<b>Good</b>
<b>8315 10 56</b>	<b>42.0+/- 10.0</b>	<b>0.9+/- 0.2</b>	<b>20.77</b>	<b>3.85</b>	<b>BB24</b>	<b>169</b>	<b>Good</b>
<b>8315 10 56</b>	<b>55.0+/- 19.0</b>	<b>0.6+/- 0.1</b>	<b>14.25</b>	<b>2.45</b>	<b>EW10</b>	<b>169</b>	<b>Good</b>
8315 10 56	83.0+/- 20.0	0.6+/- 0.1	36.47	3.33	EW20	169	Noisy
<b>8315 10 56</b>	<b>-14.0+/- 13.0</b>	<b>0.6+/- 0.2</b>	<b>36.8</b>	<b>4.05</b>	<b>BB03</b>	<b>169</b>	<b>Good</b>
8315 10 56	-37.0+/- 12.0	1.0+/- 0.2	18.99	3.29	NS13	169	Noisy
<b>8315 10 56</b>	<b>-64.0+/- 13.0</b>	<b>0.4+/- 0.1</b>	<b>30.71</b>	<b>2.68</b>	<b>BB09</b>	<b>169</b>	<b>Good</b>
8319 16 38	21.0+/- 12.0	0.5+/- 0.2	219.43	2.68	NS15	126	Noisy
8319 16 38	50.0+/- 37.0	0.7+/- 0.4	187.31	2.07	BB03	126	Noisy
8319 16 38	-23.0+/- 73.0	1.0+/- 0.8	237.49	3.7	BB14	126	Noisy
8319 16 38	-57.0+/- 26.0	0.3+/- 0.2	231.2	3.57	BB15	126	Noisy
8323 11 33	27.0+/- 64.0	1.0+/- 0.9	38.37	3.02	BB04	165	Noisy
8325 0 5	-8.0+/- 90.0	0.3+/- 0.2	347.99	3.64	BB14	193	Noisy
8326 13 17	52.0+/- 47.0	0.5+/- 0.4	45.37	2.85	BB22	181	Noisy
8326 13 17	56.0+/- 27.0	0.4+/- 0.2	37.5	3.01	BB04	181	Noisy
8326 13 17	78.0+/- 23.0	0.3+/- 0.1	8.49	2.4	NS05	181	Noisy
<b>8326 13 17</b>	<b>84.0+/- 8.0</b>	<b>0.9+/- 0.1</b>	<b>3.47</b>	<b>2.55</b>	<b>EW09</b>	<b>181</b>	<b>Good</b>
8326 13 17	-26.0+/- 28.0	0.3+/- 0.1	22.56	2.58	BB09	181	Noisy
8326 13 17	-36.0+/- 21.0	0.3+/- 0.1	23.72	2.05	BB08	181	Noisy
8326 13 17	-82.0+/- 14.0	0.5+/- 0.1	5.26	2.46	EW10	181	Noisy

8335	13	55	-14.0+/- 37.0	0.3+/- 0.2	347.97	3.57	BB14	180	Noisy	
8335	13	55	-29.0+/- 27.0	0.6+/- 0.1	28.3	2.17	BB08	180	Noisy	
8335	13	55	-60.0+/- 79.0	0.3+/- 0.2	2.66	3.01	BB11	180	Noisy	
8338	2	32	16.0+/- 27.0	0.4+/- 0.1	13.63	3.18	NS10	162	Noisy	
8338	2	32	38.0+/- 16.0	0.7+/- 0.2	19.54	3.34	BB02	162	Noisy	
<b>8338</b>	<b>2</b>	<b>32</b>	<b>-87.0+/- 13.0</b>	<b>0.5+/- 0.1</b>	<b>7.77</b>	<b>2.66</b>	<b>EW10</b>	<b>162</b>	<b>Good</b>	
8340	22	23	48.0+/- 31.0	0.6+/- 0.4	146.12	3.59	NS14	186	Noisy	
8340	22	23	50.0+/- 31.0	1.0+/- 0.4	146.84	3.52	NS15	186	Noisy	
<b>8345</b>	<b>5</b>	<b>56</b>	<b>17.0+/- 16.0</b>	<b>0.4+/- 0.1</b>	<b>18.76</b>	<b>2.96</b>	<b>BB02</b>	<b>157</b>	<b>Good</b>	
8345	5	56	-19.0+/- 58.0	0.8+/- 0.4	38.99	2.87	BB04	157	Noisy	
8345	5	56	-67.0+/- 28.0	0.3+/- 0.1	24.88	1.89	BB08	157	Noisy	
8348	0	35	16.0+/- 75.0	0.3+/- 0.2	114.25	0.92	NS14	164	Noisy	
<b>8348</b>	<b>0</b>	<b>35</b>	<b>28.0+/- 17.0</b>	<b>0.3+/- 0.0</b>	<b>89.69</b>	<b>1.2</b>	<b>BB24</b>	<b>164</b>	<b>Good</b>	
<b>8348</b>	<b>0</b>	<b>35</b>	<b>28.0+/- 18.0</b>	<b>0.4+/- 0.1</b>	<b>118.11</b>	<b>1.03</b>	<b>NS13</b>	<b>164</b>	<b>Good</b>	
8348	0	35	-26.0+/- 18.0	0.3+/- 0.1	132.7	1.13	NS10	164	Noisy	
8348	0	35	-89.0+/- 90.0	0.4+/- 0.2	107.97	1.3	BB01	164	Noisy	
8354	1	56	53.0+/- 23.0	0.3+/- 0.1	157.81	0.68	NS17	129	Noisy	
8354	1	56	-15.0+/- 62.0	0.8+/- 0.2	191.17	0.85	BB12	129	Noisy	
8354	15	21	29.0+/- 14.0	0.9+/- 0.4	128.71	1.01	NS13	147	Noisy	
8354	15	21	81.0+/- 22.0	0.4+/- 0.1	176.15	0.86	BB11	147	Noisy	
8354	15	21	-22.0+/- 23.0	0.5+/- 0.4	142.06	1.16	NS10	147	Noisy	
8354	18	2	-31.0+/- 35.0	0.4+/- 0.3	60.22	2.5	BB23	168	Noisy	
8354	18	2	-48.0+/- 33.0	1.8+/- 0.9	11.2	3.06	NS11	168	Noisy	
8355	7	12	-9.0+/- 24.0	0.4+/- 0.1	21.3	2.65	BB10	182	Noisy	
8355	7	12	-33.0+/- 30.0	0.3+/- 0.1	40.89	3.32	BB04	182	Noisy	
8359	0	28	-59.0+/- 78.0	0.3+/- 0.1	38.12	2.88	BB04	176	Noisy	
<b>8361</b>	<b>3</b>	<b>15</b>	<b>15.0+/- 11.0</b>	<b>0.3+/- 0.1</b>	<b>22.47</b>	<b>3.31</b>	<b>BB02</b>	<b>186</b>	<b>Good</b>	
8361	3	15	-3.0+/- 27.0	0.4+/- 0.2	358.43	3.6	BB13	186	Noisy	
8361	3	15	45.0+/- 46.0	0.3+/- 0.2	20.36	2.59	BB10	186	Noisy	
<b>8361</b>	<b>3</b>	<b>15</b>	<b>52.0+/- 16.0</b>	<b>1.0+/- 0.2</b>	<b>18.62</b>	<b>3.99</b>	<b>BB24</b>	<b>186</b>	<b>Good</b>	
8361	3	15	-15.0+/- 35.0	0.4+/- 0.1	349.37	3.61	BB14	186	Noisy	
8361	3	15	-32.0+/- 21.0	0.3+/- 0.1	40.48	3.26	BB04	186	Noisy	
<b>8361</b>	<b>3</b>	<b>15</b>	<b>-75.0+/- 18.0</b>	<b>0.4+/- 0.1</b>	<b>14.47</b>	<b>2.55</b>	<b>NS05</b>	<b>186</b>	<b>Good</b>	
9	64	6	4	38.0+/- 39.0	0.3+/- 0.1	49.71	3.28	BB22	201	Noisy
<b>9</b>	<b>19</b>	<b>23</b>	<b>31</b>	<b>-32.0+/- 20.0</b>	<b>0.5+/- 0.2</b>	<b>19.7</b>	<b>2.39</b>	<b>BB10</b>	<b>176</b>	<b>Good</b>
9	19	23	31	-35.0+/- 80.0	0.3+/- 0.1	41.3	3.06	BB04	176	Noisy
9	19	23	31	-74.0+/- 30.0	0.4+/- 0.1	27.13	2.58	BB09	176	Noisy
9	33	19	45	-81.0+/- 38.0	0.5+/- 0.1	16.95	3.52	BB03	143	Noisy
9	41	5	15	86.0+/- 33.0	1.3+/- 0.8	10.59	2.38	EW10	183	Noisy
8365	4	55	2.0+/- 30.0	1.0+/- 0.6	355.13	1.97	BB08	147	Noisy	
8365	4	55	5.0+/- 86.0	0.4+/- 0.2	354.78	3.29	NS13	147	Noisy	
8365	4	55	46.0+/- 36.0	0.5+/- 0.2	42.75	1.78	BB23	147	Noisy	
<b>8365</b>	<b>4</b>	<b>55</b>	<b>69.0+/- 17.0</b>	<b>0.6+/- 0.1</b>	<b>17.16</b>	<b>3.58</b>	<b>BB03</b>	<b>147</b>	<b>Good</b>	
9	1	23	9	49.0+/- 47.0	0.4+/- 0.2	21.52	2.59	BB10	195	Noisy
9	1	23	9	-11.0+/- 15.0	0.5+/- 0.1	17.59	3.12	NS10	195	Noisy
9	13	21	32	45.0+/- 46.0	0.9+/- 0.8	16.34	3.8	BB24	181	Noisy
9	13	21	32	51.0+/- 40.0	0.4+/- 0.2	39.12	3.03	BB04	181	Noisy
9	15	21	31	25.0+/- 34.0	0.5+/- 0.1	98.92	0.6	BB10	131	Noisy
9	15	21	31	30.0+/- 11.0	0.5+/- 0.3	322.43	0.97	BB15	131	Noisy

<b>9 15 21 31</b>	<b>33.0+/- 14.0</b>	<b>0.3+/- 0.2</b>	<b>48.08</b>	<b>0.81</b>	<b>NS11</b>	<b>131</b>	<b>Good</b>
9 15 21 31	-5.0+/- 29.0	0.4+/- 0.1	83.49	0.21	EW10	131	Noisy
9 15 21 31	54.0+/- 53.0	1.0+/- 0.8	317.3	1.39	BB14	131	Noisy
9 15 21 31	69.0+/- 19.0	0.6+/- 0.1	99.39	0.34	NS05	131	Noisy
9 19 23 31	48.0+/- 36.0	0.5+/- 0.4	49.2	2.93	BB22	176	Noisy
9 19 23 31	49.0+/- 43.0	0.3+/- 0.2	13.29	2.35	NS05	176	Noisy
9 19 23 31	73.0+/- 16.0	1.1+/- 0.2	9.86	2.4	EW10	176	Noisy
9 19 23 31	81.0+/- 22.0	1.1+/- 0.1	23.71	2.7	EW14	176	Noisy
9 67 5 18	5.0+/- 36.0	0.5+/- 0.1	137.48	1.26	BB24	140	Noisy
9 67 5 18	81.0+/- 11.0	0.4+/- 0.2	143.25	2.78	BB04	140	Noisy
9 67 5 18	-9.0+/- 19.0	0.7+/- 0.1	173.89	2.25	NS05	140	Noisy
9 67 5 18	-24.0+/- 30.0	0.3+/- 0.1	169.94	2.12	NS07	140	Noisy
9 75 1 56	-8.0+/- 90.0	1.5+/- 1.4	152.01	1.59	NS05	147	Noisy
9 75 1 56	86.0+/- 46.0	0.4+/- 0.1	196.25	0.6	BB15	147	Noisy
9 75 1 56	-42.0+/- 35.0	0.3+/- 0.2	154.87	1.46	EW10	147	Noisy
9 75 1 56	-81.0+/- 14.0	0.4+/- 0.0	157.12	0.87	BB11	147	Noisy

#### Intermediate (200-300 km)

8 34 20 27	18.0+/- 28.0	0.3+/- 0.2	176.02	1.73	NS12	204	Noisy
8 34 20 27	-81.0+/- 26.0	0.5+/- 0.3	195.97	1.51	BB12	204	Noisy
8 49 2 2	44.0+/- 11.0	0.5+/- 0.1	19.89	5.37	BB24	241	Noisy
<b>8119 7 26</b>	<b>17.0+/- 16.0</b>	<b>0.4+/- 0.1</b>	<b>37.66</b>	<b>2.59</b>	<b>BB22</b>	<b>200</b>	<b>Good</b>
8119 7 26	17.0+/- 20.0	0.3+/- 0.1	10.09	3.06	BB02	200	Noisy
8119 7 26	-58.0+/- 21.0	0.3+/- 0.1	350.36	3.06	BB11	200	Noisy
8147 20 20	22.0+/- 22.0	0.4+/- 0.1	20.25	3.9	BB10	208	Noisy
<b>8147 20 20</b>	<b>-65.0+/- 18.0</b>	<b>0.3+/- 0.1</b>	<b>16.31</b>	<b>3.86</b>	<b>NS05</b>	<b>208</b>	<b>Good</b>
<b>8174 12 12</b>	<b>-34.0+/- 16.0</b>	<b>0.3+/- 0.1</b>	<b>6.7</b>	<b>3.32</b>	<b>BB11</b>	<b>214</b>	<b>Good</b>
8320 15 16	5.0+/- 29.0	0.4+/- 0.2	54.16	3.29	BB23	211	Noisy
8320 15 16	-24.0+/- 25.0	0.3+/- 0.1	5.99	3.71	BB11	211	Noisy
8320 15 16	-36.0+/- 10.0	1.2+/- 0.7	16.39	3.84	NS11	211	Noisy
8320 15 16	-41.0+/- 70.0	1.4+/- 0.9	14.66	3.2	NS05	211	Noisy
8326 21 58	-26.0+/- 80.0	0.3+/- 0.2	357.5	2.26	NS05	214	Noisy
8326 21 58	-76.0+/- 25.0	0.8+/- 0.6	349.72	2.9	BB11	214	Noisy
8363 9 58	7.0+/- 21.0	1.9+/- 1.6	21.63	3.28	NS10	201	Noisy
8363 9 58	11.0+/- 24.0	0.4+/- 0.1	26.1	2.76	BB10	201	Noisy
8363 9 58	21.0+/- 70.0	0.4+/- 0.1	43.89	3.5	BB04	201	Noisy
8363 9 58	26.0+/- 19.0	0.4+/- 0.2	64.25	3.11	BB23	201	Noisy
8363 9 58	55.0+/- 24.0	0.5+/- 0.2	50.83	3.39	BB22	201	Noisy
9 64 6 4	-3.0+/- 24.0	0.4+/- 0.1	42.61	3.41	BB04	201	Noisy

#### Deep (300+ km)

8 27 13 9	-27.0+/- 90.0	1.1+/- 1.0	36	6.07	NS18	535	Noisy
8 27 13 9	-50.0+/- 53.0	0.5+/- 0.3	38.26	5.73	NS15	535	Noisy
8 39 15 59	13.0+/- 41.0	0.4+/- 0.1	98.8	4.87	EW20	577	Noisy
8 39 15 59	15.0+/- 18.0	0.3+/- 0.1	97.06	4.25	BB02	577	Noisy
8 39 15 59	21.0+/- 27.0	0.7+/- 0.1	106.12	5.45	BB22	577	Noisy
8 39 15 59	76.0+/- 75.0	0.6+/- 0.3	97.47	3.91	NS11	577	Noisy
<b>8 39 15 59</b>	<b>-53.0+/- 20.0</b>	<b>0.9+/- 0.4</b>	<b>95.75</b>	<b>3.94</b>	<b>NS12</b>	<b>577</b>	<b>Good</b>
<b>8 97 1 32</b>	<b>4.0+/- 11.0</b>	<b>0.3+/- 0.1</b>	<b>30.42</b>	<b>6.15</b>	<b>BB12</b>	<b>526</b>	<b>Good</b>
8 97 1 32	5.0+/- 45.0	0.6+/- 0.1	40.53	5.83	EW13	526	Noisy

---

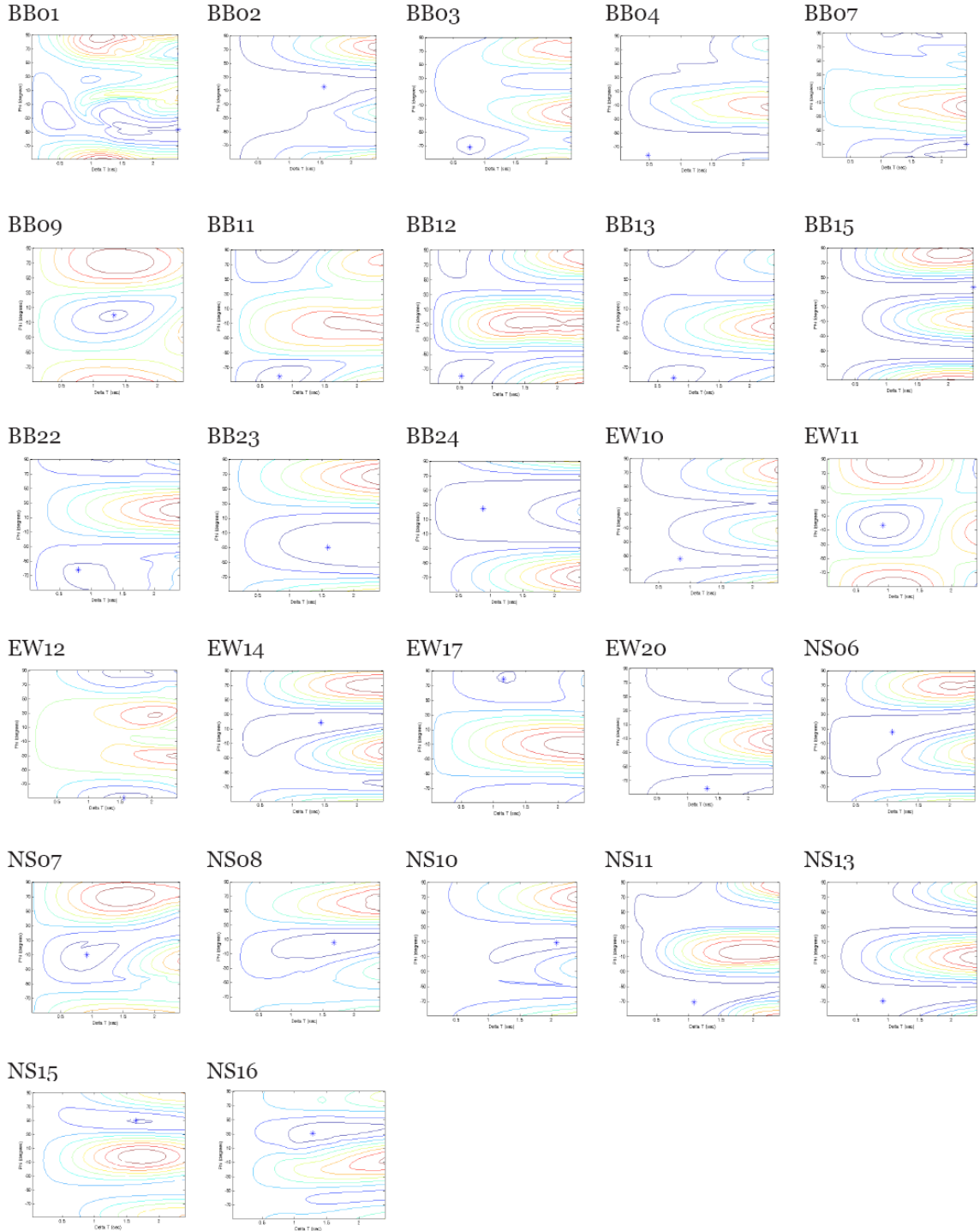
8 97 1 32	-17.0+/- 25.0	0.5+/- 0.1	30.76	5.72	BB11	526	Noisy
8 97 1 32	-56.0+/- 29.0	0.3+/- 0.1	45.21	5.39	BB08	526	Noisy
<b>8247 11 25</b>	<b>8.0+/- 20.0</b>	<b>0.3+/- 0.1</b>	<b>84.12</b>	<b>4.07</b>	<b>NS12</b>	<b>569</b>	<b>Good</b>
<b>8247 11 25</b>	<b>9.0+/- 15.0</b>	<b>0.3+/- 0.2</b>	<b>83.44</b>	<b>5.43</b>	<b>BB03</b>	<b>569</b>	<b>Good</b>
8247 11 25	-7.0+/- 27.0	0.4+/- 0.1	86.18	4.36	BB02	569	Noisy
<b>8247 11 25</b>	<b>-17.0+/- 9.0</b>	<b>1.2+/- 0.1</b>	<b>88.49</b>	<b>3.96</b>	<b>NS09</b>	<b>569</b>	<b>Good</b>
8247 11 25	-73.0+/- 20.0	0.4+/- 0.2	93.45	5.19	BB04	569	Noisy
<b>8265 17 35</b>	<b>14.0+/- 15.0</b>	<b>0.6+/- 0.4</b>	<b>75.49</b>	<b>3.48</b>	<b>BB12</b>	<b>563</b>	<b>Good</b>
<b>8265 17 35</b>	<b>84.0+/- 9.0</b>	<b>0.4+/- 0.1</b>	<b>89.15</b>	<b>3.4</b>	<b>EW09</b>	<b>563</b>	<b>Good</b>
8358 16 48	12.0+/- 15.0	0.3+/- 0.2	100.93	5.27	BB22	570	Noisy
8358 16 48	61.0+/- 33.0	0.3+/- 0.1	99.4	3.85	BB10	570	Noisy
9 3 21 15	2.0+/- 24.0	0.4+/- 0.1	104.45	4.18	NS16	627	Noisy
9 3 21 15	24.0+/- 30.0	1.4+/- 0.2	113.12	3.76	BB11	627	Noisy
9 3 21 15	40.0+/- 37.0	0.6+/- 0.4	106.99	4.38	NS13	627	Noisy
9 3 21 15	73.0+/- 21.0	1.1+/- 0.1	108.73	4.72	BB02	627	Noisy
<b>9 3 21 15</b>	<b>79.0+/- 16.0</b>	<b>0.9+/- 0.7</b>	<b>110.19</b>	<b>5.08</b>	<b>EW17</b>	<b>627</b>	<b>Good</b>
9 3 21 15	-22.0+/- 16.0	0.9+/- 0.1	111.84	5.7	BB04	627	Noisy
9 3 21 15	-34.0+/- 24.0	0.3+/- 0.2	112.67	3.2	BB15	627	Noisy
9 3 21 15	-56.0+/- 22.0	1.5+/- 0.8	108.97	5.35	EW20	627	Noisy
<b>9 3 21 15</b>	<b>-86.0+/- 12.0</b>	<b>1.4+/- 0.1</b>	<b>104.95</b>	<b>4.67</b>	<b>BB01</b>	<b>627</b>	<b>Good</b>
9 3 21 15	-87.0+/- 86.0	1.0+/- 0.8	114.6	6.02	BB22	627	Noisy

---

## Appendix G: Stacking results

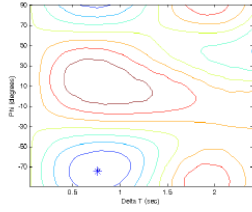
Stacked energy plots for all possible stations with teleseismic events using a weight factor of the lag time with least associated error.

**Data set includes both 'Noisy' and 'Good' quality splitting events.**

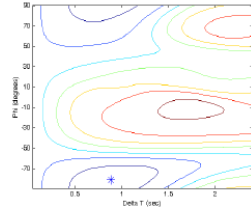


**Data set includes only 'Good' quality splitting teleseismic events.**

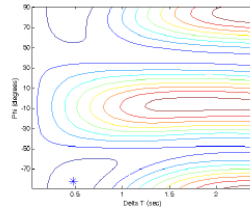
BB03



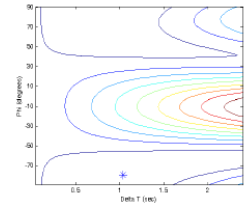
BB11



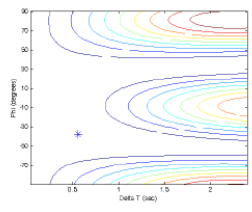
BB12



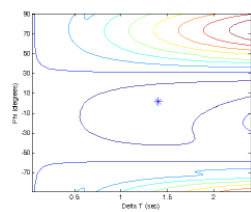
BB13



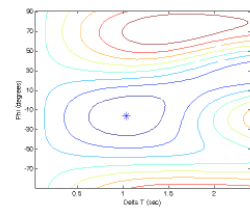
BB15



EW10



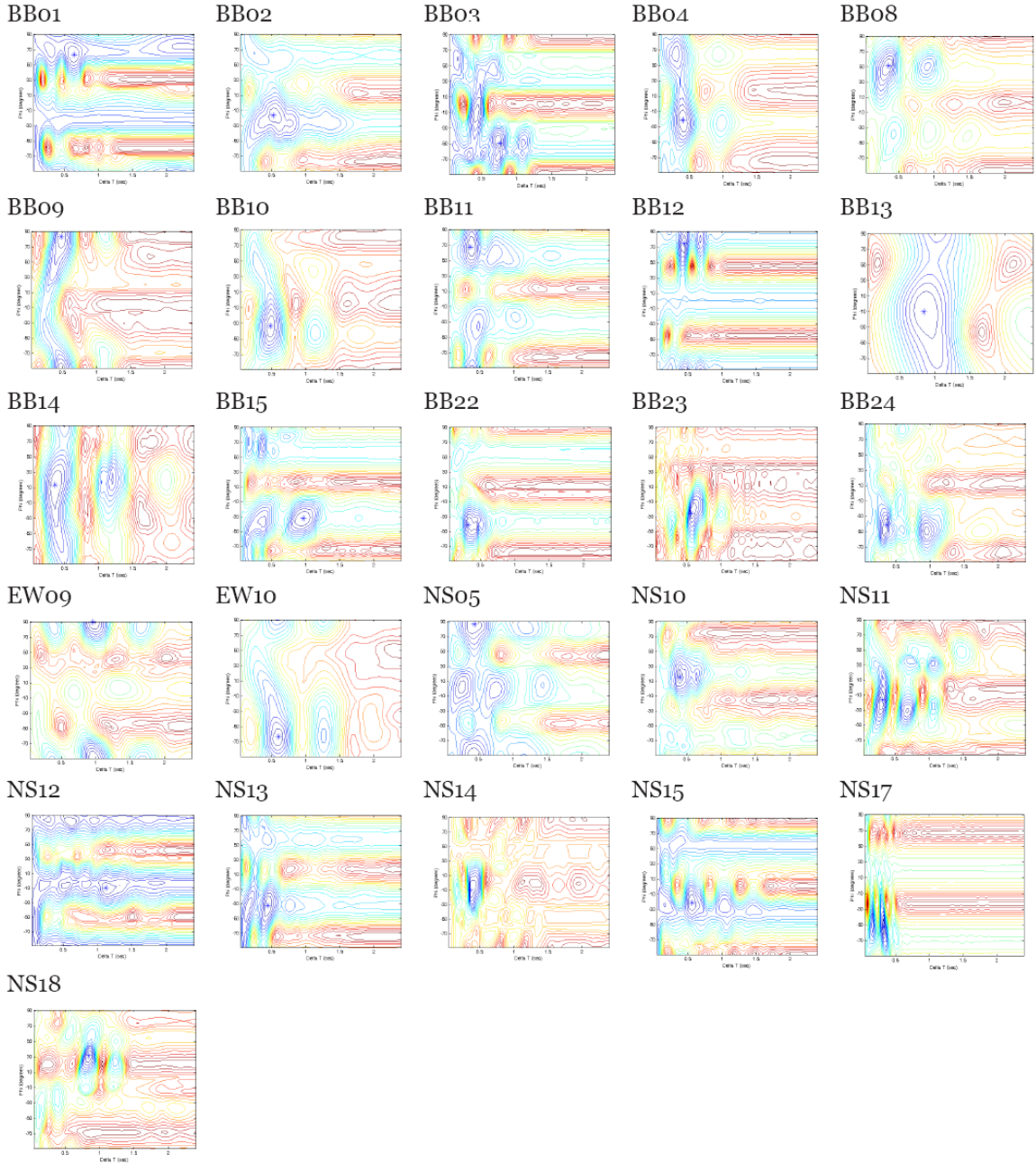
NS07



Stacked energy plots for all possible stations with local events using a weight factor of the lag time with least associated error.

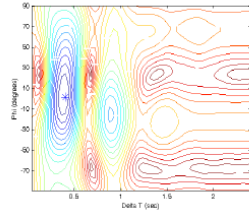
**Data set includes both 'Noisy' and 'Good' quality splitting events**

**Shallow events (0-200 km depth):**

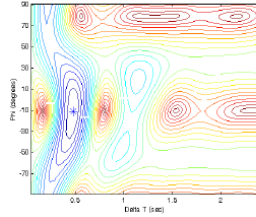


**Intermediate events (200-300 km depth):**

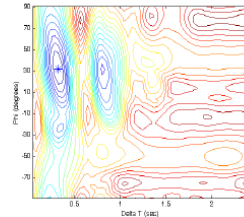
BB04



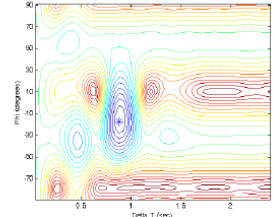
BB10



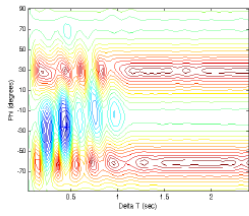
BB11



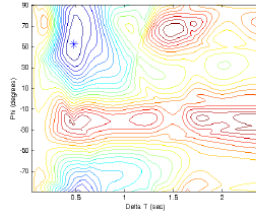
BB22



BB23

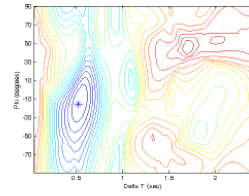


NS05

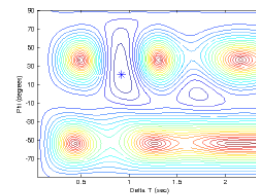


**Deep events (300+ km depth):**

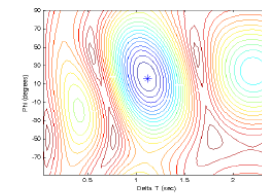
BB02



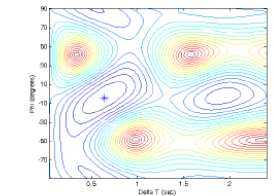
BB04



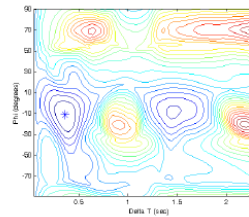
BB11



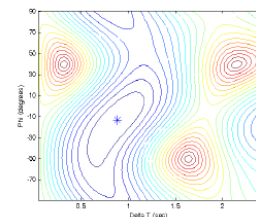
BB12



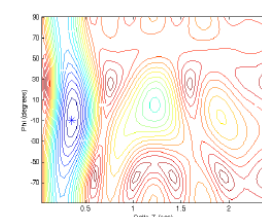
BB22



EW20



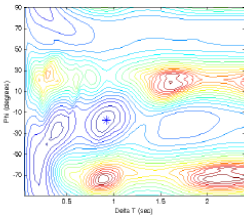
NS12



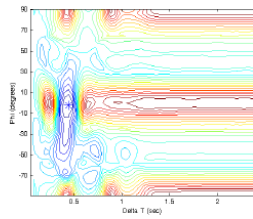
**Data set includes only 'Good' quality splitting teleseismic events.**

**Shallow events (0-200 km depth):**

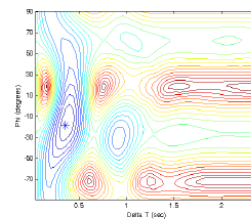
BB02



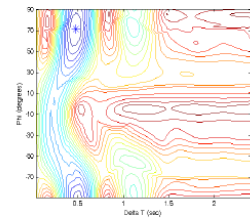
BB03



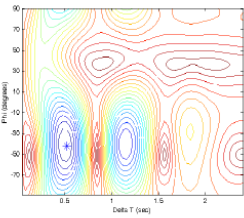
BB04



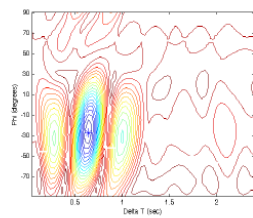
BB09



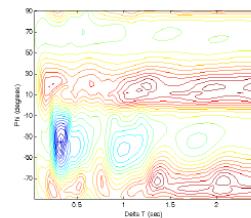
BB10



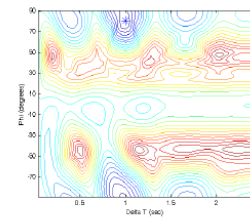
BB23



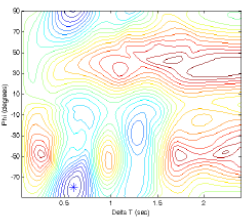
BB24



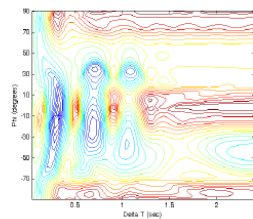
EW09



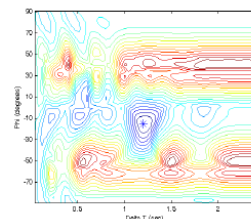
EW10



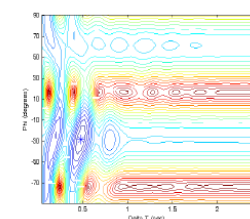
NS11



NS12

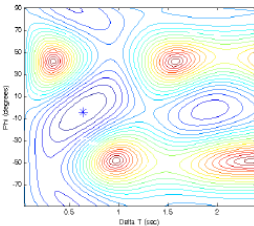


NS13

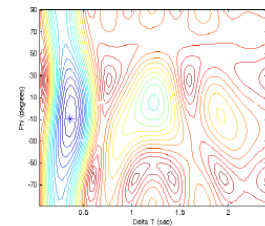


**Deep events (300+ km depth):**

BB12



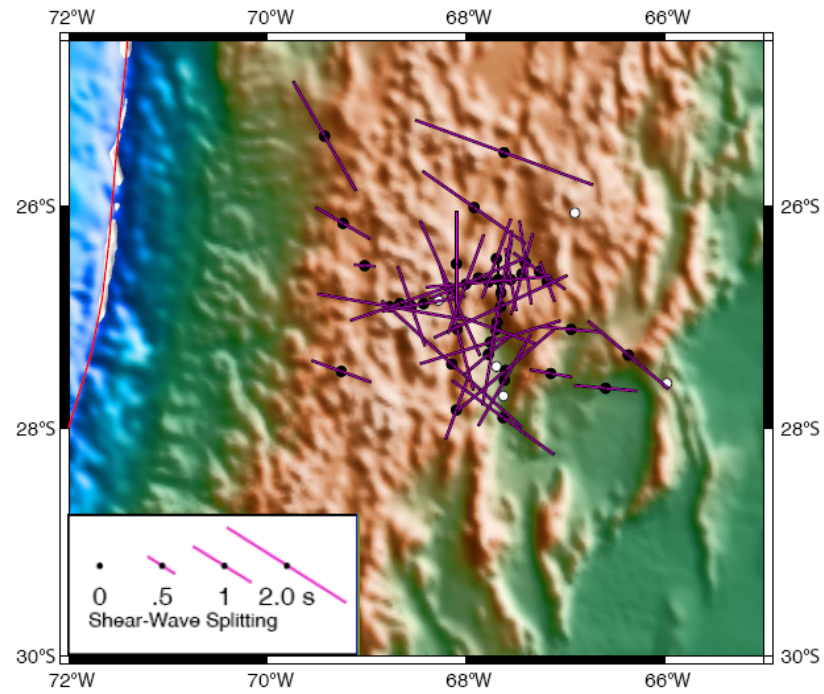
NS12



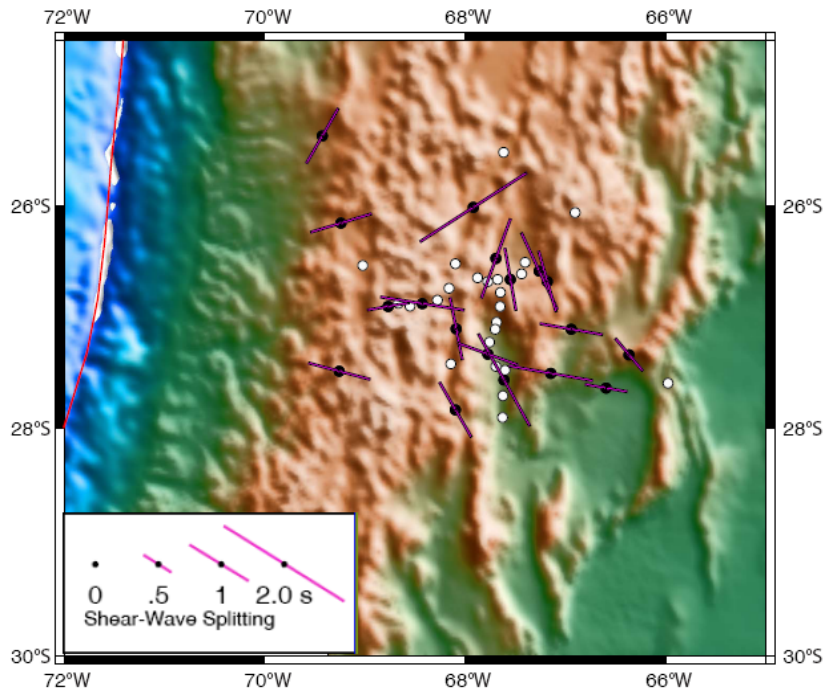
## Appendix H: Topographic plots of stacking results

Stacking results for teleseismic events using least lag time error weight

### All ('Good' and 'Noisy') data

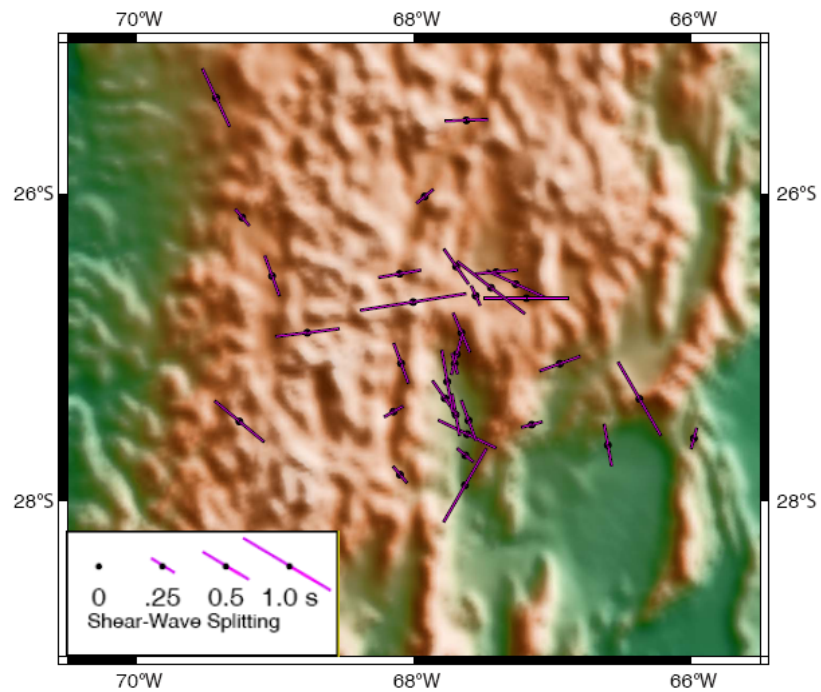


### Only 'Good' data

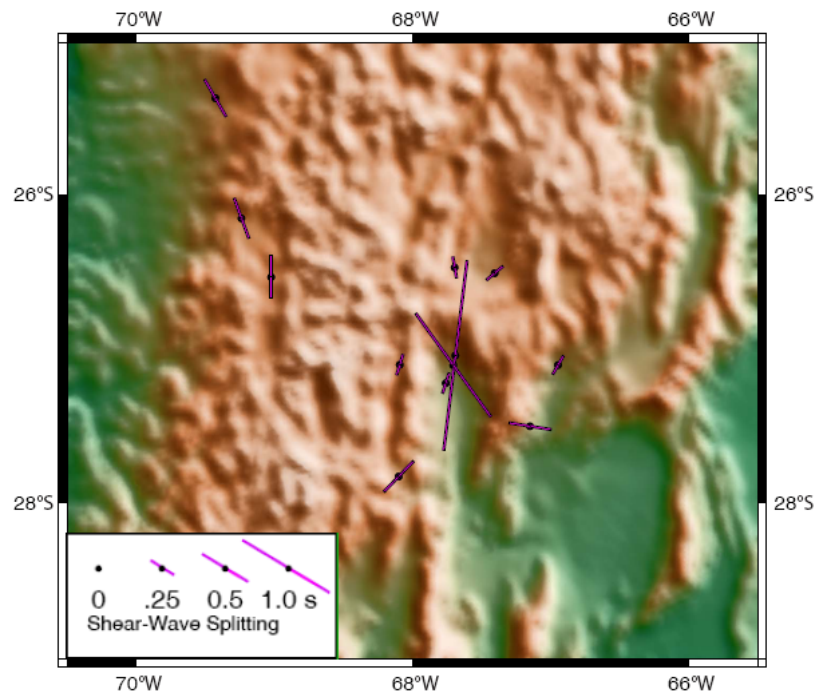


Stacking results for local events having at least 0.3 seconds lag time and using least lag time error weight.

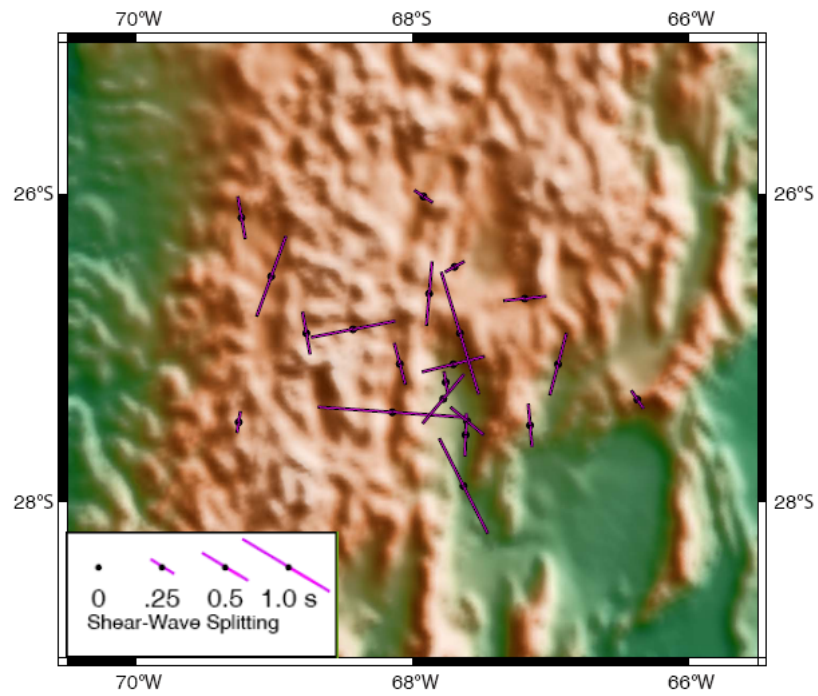
**All ('Good' and 'Noisy') data - shallow depth**



**All ('Good' and 'Noisy') data - intermediate depth**

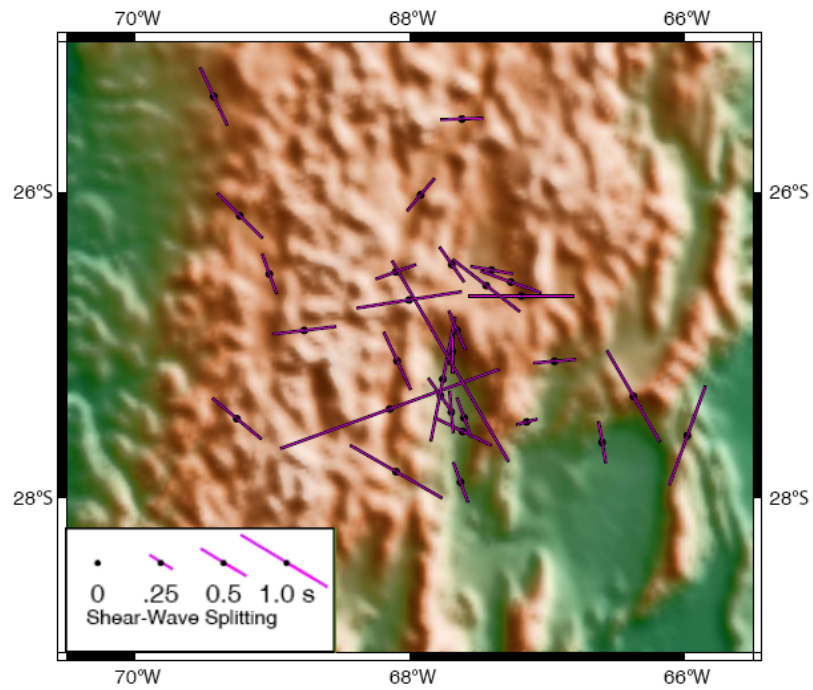


**All ('Good' and 'Noisy') data - deep depth**

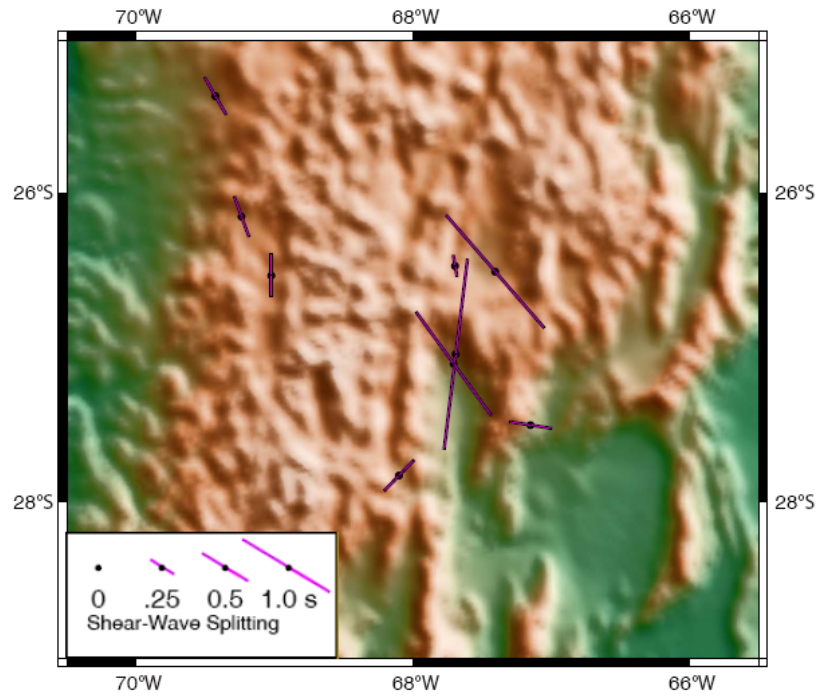


Stacking results for local events having at least 0.4 seconds lag time and using least lag time error weight.

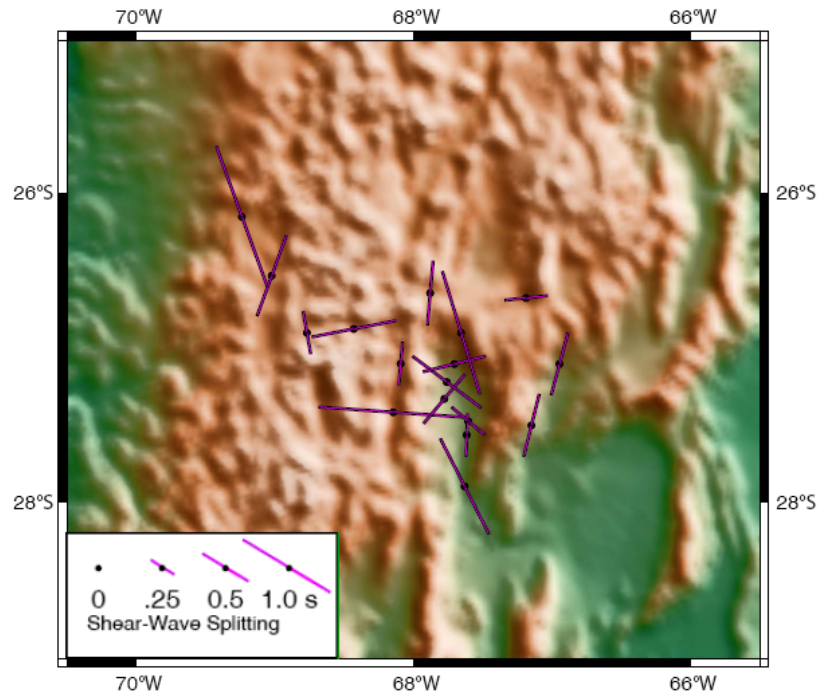
**All ('Good' and 'Noisy') data - shallow depth**



**All ('Good' and 'Noisy') data - intermediate depth**



**All ('Good' and 'Noisy') data - deep depth**



## REFERENCES

- Allmendinger, R.W., Jordan, T.E., Kay, S.M., and Isacks, B.L., 1997, The evolution of the Altiplano-Puna plateau of the Central Andes: *Annual Review of Earth and Planetary Sciences*, v. 25, p. 139-174.
- Allmendinger, R.W., Reilinger, R., and Loveless, J., 2007, Strain and rotation rate from GPS in Tibet, Anatolia, and the Altiplano: *Tectonics*, v. 26, p. 1-18.
- Anderson, M.L., Zandt, G., Triep, E., Fouch, M., and Beck, S., 2004, Anisotropy and mantle flow in the Chile-Argentina subduction zone from shear wave splitting analysis: *Geophysical Research Letters*, v. 31, p. 1-4.
- Babeyko, A., and Sobolev, S., 2005, Quantifying different modes of the late Cenozoic shortening in the central Andes: *Geology*, v. 33, p. 621-624.
- Babuska, V., and Cara, M., 1991, *Seismic Anisotropy in the Earth*: Kluwer Academic Publishers, 217 p.
- Baccheschi, P., Margheriti, L., and Steckler, M., 2007, Seismic anisotropy reveals focused mantle flow around the Calabrian slab (southern Italy): *Geophysical Research Letters*, v. 34, p. 1-6.
- Beck, S., and Zandt, G., 2002, The nature of orogenic crust in the central Andes: *Journal of Geophysical Research*, v. 107, p. 2230-2245.
- Bird, P., 1979, Continental delamination and the Colorado Plateau: *Journal of Geophysical Research*, v. 84, p. 7561-7571.
- Bjarnason, I.T., Silver, P.G., Rumpker, G., and Solomon, S.C., 2002, Shear wave splitting across the Iceland hot spot: Results from the ICEMELT experiment: *Journal of Geophysical Research*, v. 107, 2382-2393.
- Bowman, J.R., and Ando, M., 1987, Shear-wave splitting in the upper-mantle wedge above the Tonga subduction zone: *Geophysical Journal of the Royal Astronomical Society*, v. 88, p. 25-41.
- Buontempo, L., Bokelmann, G.H.R., Barruol, G., and Morales, J., 2008, Seismic anisotropy beneath southern Iberia from SKS splitting: *Earth and Planetary Science Letters*, v. 273, p. 237-250.
- Cahill, T., and Isacks, B.L., 1992, Seismicity and shape of the subducted Nazca Plate: *Journal of Geophysical Research*, v. 97, p. 17,503-17,529.

- de Silva, S.L., Zandt, G., Trumbull, R., Viramonte, J., 2006a, Large scale silicic volcanism – the result of thermal maturation of the crust: *Advances in Geosciences, Proceedings Volume of the Asia-Oceania Geosciences*, p. 215-230.
- England, P., and Houseman, G., 1989, Extension during continental convergence, with application to the Tibetan plateau: *Journal of Geophysical Research*, v. 94, p. 17561-17579.
- Espurt, N., Baby, P., Brusset, S., Roddaz, M., Hermoza, W., Regard, V., et al., 2007, How does the Nazca Ridge subduction influence the modern Amazonian foreland basin?: *Geology*, v. 35, p. 515-518.
- Espurt, N., Funicello, F., Martinod, J., Guillaume, B., Regard, V., Faccenna, C., and Brusset, S., 2008, Flat subduction dynamics and deformation of the South American Plate: insights from analog modeling: *Tectonics*, v. 27, p. 1-19.
- Febrer, J.M., Baldis, B., Gasco, J.C., Mamani, M., and Pomposiolo, C., 1982, La anomalia geotermica calchaqui en el Noroeste Argentino; Un nuevo proceso geodinamico asociado a la subduccion de la placa de Nazca. The Calchaqui geothermal anomaly in northwestern Argentina; a new geodynamic process associated with subduction of the Nazca Plate: *Quinto congreso latinoamericano de geologia*, v. 3, p. 691-703.
- Fielding, E.J., 1989, Neotectonics of the central Andean cordillera from satellite imagery, Ph.D., thesis, 213 p.
- Gilbert, H., Beck, S., and Zandt, G., 2006, Lithospheric and upper mantle structure of central Chile and Argentina: *Geophysical Journal International*, v. 165, p. 383-398.
- Hindle, D., Kley, J., Oncken, O., and Sobolev, S., 2005, Crustal balance and crustal flux from shortening estimates in the Central Andes: *Earth and Planetary Science Letters*, v. 230, p. 113-124.
- Isacks, B.L., 1988, Uplift of the Central Andean plateau and bending of the Bolivian orocline, *Journal of Geophysical Research*, v. 93, p. 3211-3231.
- Jung, H., and Karato, S.-i., 2001, Water-induced fabric transitions in olivine: *Science*, v. 293, p. 1460-1462.
- Kay, S.M., Coira, B., and Viramone, J., 1994, Young mafic back arc volcanic rocks as indicators of continental lithospheric delamination beneath the Argentine Puna plateau, central Andes: *Journal of Geophysical Research*, v. 99, p. 24,323-24,339.

- Kay, R.W., and Kay, S.M., 1993, Delamination and delamination magmatism: *Tectonophysics*, v. 219, p. 177-189.
- Kay, S.M., 1999, The role of magmas in plateau formation: Abstracts with Programs – Geological Society of America, v. 31, 66 p.
- Kneller, E., van Keken, P., Karato, S., and Park, J., 2005, B-type olivine fabric in the mantle wedge: insights from high-resolution non-Newtonian subduction zone models: *Earth and Planetary Science Letters*, v. 237, p. 781-797.
- Lamb, S., and Hoke, L., 1997, Origin of the high plateau in the Central Andes, Bolivia, South America: *Tectonics*, v. 16, p. 623-649.
- Long, M.D., and van der Hilst, R.D., 2006, Shear wave splitting from local events beneath the Ryuku Arc; trench-parallel anisotropy in the mantle wedge: *Physics of the Earth and Planetary Interiors*, v. 155, p. 300-312.
- McNamara, D.E., Owens, T.J., Silver, P.G., and Wu, F.T., 1994, Shear wave anisotropy beneath the Tibetan Plateau: *Journal of Geophysical Research*, v. 99, p. 13655-13665.
- Peyton, V., Levin, V., Park, J., Brandon, M., Lees, J., Gordeev, E., et al., 2001, Mantle flow at a slab edge; seismic anisotropy in the Kamchatka region: *Geophysical Research Letters*, v. 28, p. 379-382.
- Polet, J., Silver, P.G., Beck, S., Wallace, T., Zandt, G., Ruppert, S., Kind, R., and Rudloff, A., 2000, Shear wave anisotropy beneath the Andes from the BANJO, SEDA, and PISCO experiments: *Journal of Geophysical Research*, v. 105, p. 6287-6304.
- Restivo, A., and Helffrich, G., 1999, Teleseismic shear wave splitting measurements in noisy environments: *Geophysical Journal International*, v. 137, p. 821-830.
- Ribe, N.M., 1989, Seismic anisotropy and mantle flow: *Journal of Geophysical Research*, v. 94, p. 4213-4223.
- Riller, U., Petrinovic, I., Ramelow, J., Strecker, M., and Oncken, O., 2001, Late Cenozoic tectonism, collapse caldera and plateau formation in the central Andes: *Earth and Planetary Science Letters*, v. 188, p. 299-311.
- Russo, R.M., and Silver, P.G., 1994, Trench-parallel flow beneath the Nazca Plate from seismic anisotropy: *Science*, v. 263, p. 1105-1111.

- Russo, R.M., and Silver, P.G., 1996, Cordillera formation, mantle dynamics, and the Wilson cycle: *Geology*, v. 24, p. 511-514.
- Sandvol, E. and Ni, J., 1997, Deep azimuthal seismic anisotropy in the southern Kurile and Japan subduction zones: *Journal of Geophysical Research*, v. 102, p. 9911-9922.
- Sandvol, E., Ni, J.F., Hearn, T.M., and Roecker, S., 1994, Seismic azimuthal anisotropy beneath the Pakistan Himalayas: *Geophysical Research Letters*, v. 21, p. 1635-1638.
- Sandvol, E., Ni, J., Kind, R., and Zhao, W., 1997, Seismic anisotropy beneath the southern Himalayas – Tibet collision zone: *Journal of Geophysical Research*, v. 102, p. 17,813-17,823.
- Savage, M.K., 1999, Seismic anisotropy and mantle deformation: What have we learned from shear wave splitting?: *Reviews of Geophysics*, v. 37, p. 65-106.
- Schurr, B., Rietbrock, A., Asch, G., Kind, R., and Oncken, O., 2006, Evidence for lithospheric detachment in the central Andes from local earthquake tomography: *Tectonophysics*, v. 415, p. 203-223.
- Silver, P.G., and Chan, W.W., 1988, Implications for continental structure and evolution from seismic anisotropy, *Nature*, v. 335, p. 34-39.
- Silver, P.G., and Chan, W.W., 1991, Shear wave splitting and subcontinental mantle deformation: *Journal of Geophysical Research*, v. 96, p. 16,429-16,454.
- Silver, P.G., and Savage, M.K., 1994, The interpretation of shear-wave splitting parameters in the presence of two anisotropic layers: *Geophysical Journal International*, v. 119, p. 949-963.
- Smith, G.P., Wiens, D.A., Fischer, K.M., Dorman, L.M., Webb, S.C., and Hildebrand, J.A., 2001, A complex pattern of mantle flow in the Lau backarc: *Science*, v. 292, p. 713-716.
- Sobolev, S.V., and Babeyko, A.Y., 2005, What drives orogeny in the Andes?: *Geology*, v. 33, p. 617-620.
- Teanby, N.A., Kendall, J.-M., and van der Baan, M., 2004, Automation of shear-wave splitting measurements using cluster analysis: *Bulletin of the Seismological Society of America*, v. 94, p. 453-463.

- Vinnik, L.P., Farra, V., and Romanowicz, B., 1989, Azimuthal anisotropy in the Earth from observations of SKS at GEOSCOPE and NARS broadband stations: *Bulletin of Seismological Society of America*, v. 79, p. 1542-1558.
- Vinnik, L.P., Makeyeva, L.I., Milev, A., and Usenko, A.Y., 1992, Global patterns of azimuthal anisotropy and deformations in the continental mantle: *Geophysical Journal International*, v. 111, p. 433-447.
- West, J.D., Fouch, M.J., Roth, J.B., and Elkins-Tanton, L.T., 2009, Vertical mantle flow associated with a lithospheric drip beneath the Great Basin: *Nature Geoscience*, v. 2, p. 439-444.
- Whitman, D., Isacks, B.L., Chatelain, J.-L., Chiu, J.-M., and Perez, A., 1992, Attenuation of high-frequency seismic waves beneath the Central Andean plateau: *Journal of Geophysical Research*, v. 97, p. 19,929-19,947.
- Whitman, D., Isacks, B.L., and Kay, S.M., 1996, Lithospheric structure and along-strike segmentation of the Central Andean Plateau: seismic Q, magmatism, flexure, topography and tectonics: *Tectonophysics*, v. 259, p. 29-40.
- Wolfe, C.J., and Silver, P.G., 1998, Seismic anisotropy of oceanic upper mantle: Shear wave splitting methodologies and observations: *Journal of Geophysical Research*, v. 103, p. 749-771.
- Wolfe, C.J., and Vernon III, F.L., 1998, Shear-wave splitting at central Tien shan: Evidence for rapid variation of anisotropic patterns: *Geophysical Research Letters*, v. 25, p. 1217-1220.
- Wolfe, C.J., Vernon III, F.L., and Al-Amri, A., 1999, Shear-wave splitting across western Saudi Arabia: The pattern of upper mantle anisotropy at a Proterozoic shield: *Geophysical Research Letters*, v. 26, p. 779-782.
- Wüstefeld, A., and Bokelmann, G., 2007, Null detection in shear-wave splitting measurements: *Bulletin of the Seismological Society of America*, v. 97, p. 1204-1211.
- Yuan, X., Sobolev, S.V., and Kind, R., 2002, Moho topography in the central Andes and its geodynamic implications: *Earth and Planetary Science Letters*, v. 199, p. 389-402.
- Zhao, L., and Zheng, T., 2007, Complex upper-mantle deformation beneath the North China Craton: implications for lithospheric thinning: *Geophysical Journal International*, v. 170, p. 1095-1099.